N72-30903

NASA TECHNICAL NOTE

NASA TN D-6934

NASA TN D-6934

CASE FILE COPY

FLIGHT-DETERMINED DERIVATIVES AND DYNAMIC CHARACTERISTICS FOR THE HL-10 LIFTING BODY VEHICLE AT SUBSONIC AND TRANSONIC MACH NUMBERS

by Larry W. Strutz

Flight Research Center

Edwards, Calif. 93523

NATIONAL AERONAUTICS AND SPACE ADMINISTRATION • WASHINGTON, D. C. • SEPTEMBER 1972

1. Report No. NASA TN D-6934	2. Government Accession No.	3. Recipient's Catalog No.

4. Title and Subtitle FLIGHT-DETERMINED DERIVATIVES AND DYNAMIC CHARACTERISTICS FOR THE HL-10 LIFTING BODY VEHICLE AT SUBSONIC AND TRANSONIC MACH NUMBERS	5. Report Date September 1972 6. Performing Organization Code
7. Author(s) Larry W. Strutz	8. Performing Organization Report No. H-708
9. Performing Organization Name and Address NASA Flight Research Center P.O. Box 273 Edwards, California 93523	10. Work Unit No. 136-62-02-00-24 11. Contract or Grant No.
12. Sponsoring Agency Name and Address National Aeronautics and Space Administration Washington, D. C. 20546	13. Type of Report and Period Covered Technical Note 14. Sponsoring Agency Code

15. Supplementary Notes

16. Abstract

HL-10 lifting body stability and control derivatives were determined by using an analog-matching technique and compared with derivatives obtained from wind-tunnel results. The flight derivatives were determined as a function of angle of attack for a subsonic configuration at Mach 0.7 and for a transonic configuration at Mach 0.7, 0.9, and 1.2. At an angle of attack of 14°, data were obtained for a Mach number range from 0.6 to 1.4.

The flight and wind-tunnel derivatives were in general agreement, with the possible exception of the longitudinal and lateral damping derivatives. Some differences were noted between the vehicle dynamic response characteristics calculated from flight-determined derivatives and those predicted by the wind-tunnel results. However, the only difference the pilots noted between the response of the vehicle in flight and the response of a simulator programed with wind-tunnel-predicted data was that the damping generally was higher in the flight vehicle.

17. Key Words (Suggested by Author(s)) Lifting bodies Stability and control derivatives	18. Distribution Statement Unclassified - Unlimited

19. Security Classif. (of this report) Unclassified	20. Security Classif. (of this page) Unclassified	21. No. of Pages 77	22. Price* $3.00

*For sale by the National Technical Information Service, Springfield, Virginia 22151

FLIGHT-DETERMINED DERIVATIVES AND DYNAMIC CHARACTERISTICS FOR THE HL-10 LIFTING BODY VEHICLE AT SUBSONIC AND TRANSONIC MACH NUMBERS

Larry W. Strutz
Flight Research Center

INTRODUCTION

The design of the HL-10 lifting body vehicle is based on a NASA Langley Research Center concept for a vehicle capable of reentering the earth's atmosphere and landing horizontally. The HL-10 configuration is one of several proposed configurations. Three of these configurations are being flight tested at Mach numbers less than 2 (ref. 1) at the NASA Flight Research Center in a joint program with the U.S. Air Force.

During the expansion of the HL-10 flight envelope, stability and control maneuvers were performed to assess the vehicle's handling and stability and control characteristics. These evaluations were used to update the fixed-base HL-10 simulation, which had been programed with wind-tunnel predictions, in order to obtain improved predictions of vehicle behavior during the flight envelope expansion. The flight maneuvers were analyzed for aerodynamic stability and control derivatives and trim. This report presents the results of these analyses and compares them with predictions from wind-tunnel tests (refs. 2 to 8). Aerodynamic derivatives are presented as a function of angle of attack for Mach numbers of 0.7, 0.9, and 1.2 and for a range of Mach numbers from 0.6 to 1.4 at an angle of attack of about 14°. The significance of the differences between the flight-measured and predicted characteristics is discussed.

SYMBOLS

Data are presented in the form of standard NASA coefficients of forces and moments, which are referenced to the body axes passing through the center of gravity. The positive directions are: X, forward; Y, to the right; Z, down. Positive directions of the forces, moments, and angular displacements and velocities are in accord with the right-hand rule.

Physical quantities in this report are given in the International System of Units (SI) and parenthetically in U.S. Customary Units. Measurements were taken in Customary Units. Factors relating the two systems are given in reference 9.

a_n	normal acceleration, g units
a_t	transverse acceleration, g units
a_x	longitudinal acceleration, g units

b	wingspan, meters (feet)
C	dimensional chord-force coefficient, $\frac{\text{Chord force}}{mV}$, per second
C_c	nondimensional chord-force coefficient, $\frac{\text{Chord force}}{\bar{q}S}$
$C_{c_q} = \frac{\partial C_c}{\partial \frac{q\bar{c}}{2V}}$, per radian	
$C_{c_\alpha} = \frac{\partial C_c}{\partial \alpha}$, per degree	
$C_{c_{\delta_e}} = \frac{\partial C_c}{\partial \delta_e}$, per degree	
C_l	nondimensional rolling-moment coefficient, $\frac{\text{Rolling moment}}{\bar{q}Sb}$
C_{l_p}	nondimensional damping-in-roll derivative, $\frac{\partial C_l}{\partial \frac{pb}{2V}}$, per radian
$C_{l_r} = \frac{\partial C_l}{\partial \frac{rb}{2V}}$, per radian	
C_{l_β}	nondimensional effective dihedral derivative, $\frac{\partial C_l}{\partial \beta}$, per degree
$C_{l_{\dot{\beta}}} = \frac{\partial C_l}{\partial \frac{\dot{\beta} b}{2V}}$, per radian	
$C_{l_{\delta_a}}$	nondimensional rolling moment due to aileron derivative, $\frac{\partial C_l}{\partial \delta_a}$, per degree
$C_{l_{\delta_r}}$	nondimensional rolling moment due to rudder derivative, $\frac{\partial C_l}{\partial \delta_r}$, per degree
C_m	nondimensional pitching-moment coefficient, $\frac{\text{Pitching moment}}{\bar{q}S\bar{c}}$
C_{m_q}	nondimensional damping-in-pitch derivative, $\frac{\partial C_m}{\partial \frac{q\bar{c}}{2V}}$, per radian
C_{m_α}	nondimensional static pitch-stability derivative, $\frac{\partial C_m}{\partial \alpha}$, per degree

$C_{m_{\dot{\alpha}}} = \frac{\partial C_m}{\partial \frac{\dot{\alpha}\bar{c}}{2V}}$, per radian	
$C_{m_{\delta_e}}$	nondimensional elevator-effectiveness derivative, $\frac{\partial C_m}{\partial \delta_e}$, per degree
C_N	nondimensional normal-force coefficient, $\frac{\text{Normal force}}{\bar{q}S}$
$C_{N_q} = \frac{\partial C_N}{\partial \frac{q\bar{c}}{2V}}$	
C_{N_α}	nondimensional normal-force-due-to-angle-of-attack derivative, $\frac{\partial C_N}{\partial \alpha}$, per degree
$C_{N_{\delta_e}}$	nondimensional normal-force-due-to-elevator-derivative, $\frac{\partial C_N}{\partial \delta_e}$, per degree
C_n	nondimensional yawing-moment coefficient, $\frac{\text{Yawing moment}}{\bar{q}Sb}$
$C_{n_p} = \frac{\partial C_n}{\partial \frac{pb}{2V}}$, per radian	
C_{n_r}	nondimensional damping-in-yaw derivative, $\frac{\partial C_n}{\partial \frac{rb}{2V}}$, per radian
C_{n_β}	nondimensional static-directional-stability derivative, $\frac{\partial C_n}{\partial \beta}$, per degree
$C_{n_{\dot{\beta}}} = \frac{\partial C_n}{\partial \frac{\dot{\beta}b}{2V}}$, per radian	
$C_{n_{\delta_a}}$	nondimensional yawing-moment-due-to-aileron derivative, $\frac{\partial C_n}{\partial \delta_a}$, per degree
$C_{n_{\delta_r}}$	nondimensional yawing-moment-due-to-rudder derivative, $\frac{\partial C_n}{\partial \delta_r}$, per degree
$C_q = \frac{\partial C}{\partial q}$, per radian	

C_Y	nondimensional side-force coefficient, $\frac{\text{Side force}}{\bar{q}S}$
C_{Y_β}	nondimensional side-force-due-to-sideslip derivative, $\frac{\partial C_Y}{\partial \beta}$, per degree
$C_{Y_{\delta_a}}$	nondimensional side-force-due-to-aileron derivative, $\frac{\partial C_Y}{\partial \delta_a}$, per degree
$C_{Y_{\delta_r}}$	nondimensional side-force-due-to-rudder derivative, $\frac{\partial C_Y}{\partial \delta_r}$, per degree

$C_\alpha = \frac{\partial C}{\partial \alpha}$, per radian-second

$C_{\delta_e} = \frac{\partial C}{\partial \delta_e}$, per radian-second

$\bar{c}$	mean aerodynamic chord, meters (feet)
g	acceleration due to gravity, 9.807 meters per second^2 (32.174 feet per second^2)
I_X, I_Y, I_Z	moment of inertia about body X-, Y-, and Z-axis, respectively, kilogram-meter^2 (slug-foot^2)
I_{XZ}	product of inertia referred to body X and Z axes, kilogram-meter^2 (slug-foot^2)
L	dimensional rolling-moment coefficient, $\frac{\text{Rolling moment}}{I_X}$, per second^2

$L' = \dfrac{L + \dfrac{I_{XZ}}{I_X} N}{1 - \dfrac{I_{XZ}^2}{I_X I_Z}}$, per second^2

$L'_p = \frac{\partial L'}{\partial p}$, per second-radian

$L'_r = \frac{\partial L'}{\partial r}$, per second-radian

$L'_\beta = \frac{\partial L'}{\partial \beta}$, per second^2-radian

$L'_{\dot{\beta}} = \frac{\partial L'}{\partial \dot{\beta}}$, per second-radian

$L'_{\delta_a} = \frac{\partial L'}{\partial \delta_a}$, per second^2-radian

$L'_{\delta_r} = \frac{\partial L'}{\partial \delta_r}$, per second^2-radian

M Mach number or dimensional pitching-moment coefficient, $\frac{\text{Pitching moment}}{I_Y}$, per second^2

$M_q = \frac{\partial M}{\partial q}$, per second-radian

$M_\alpha = \frac{\partial M}{\partial \alpha}$, per second^2-radian

$M_{\dot{\alpha}} = \frac{\partial M}{\partial \dot{\alpha}}$, per second-radian

$M_{\delta_e} = \frac{\partial M}{\partial \delta_e}$, per second^2-radian

m mass, kilograms (slugs)

$\bar{N}$ dimensional normal-force coefficient, $\frac{\text{Normal force}}{mV}$, per second

N dimensional yawing-moment coefficient, $\frac{\text{Yawing moment}}{I_Z}$, per second^2

$$N' = \frac{N + \frac{I_{XZ}}{I_Z} L}{1 - \frac{I_{XZ}^2}{I_X I_Z}}, \text{ per second}^2$$

$N'_p = \frac{\partial N'}{\partial p}$, per second-radian

$\bar{N}_q = \frac{\partial \bar{N}}{\partial q}$, per radian

$N'_r = \frac{\partial N'}{\partial r}$, per second-radian

$\bar{N}_\alpha = \frac{\partial \bar{N}}{\partial \alpha}$, per second-radian

$\bar{N}_{\dot{\alpha}} = \frac{\partial \bar{N}}{\partial \dot{\alpha}}$, per radian

$N'_{\beta} = \frac{\partial N'}{\partial \beta}$, per second^2-radian

$N'_{\dot{\beta}} = \frac{\partial N'}{\partial \dot{\beta}}$, per second-radian

$N'_{\delta_a} = \frac{\partial N'}{\partial \delta_a}$, per second^2-radian

$\bar{N}_{\delta_e} = \frac{\partial \bar{N}}{\partial \delta_e}$, per second-radian

$N'_{\delta_r} = \frac{\partial N'}{\partial \delta_r}$, per second^2-radian

P	period of damped natural frequency of the airplane, seconds
p, q, r	time rate of change of roll, pitch, and yaw about body X-, Y-, and Z-axis, respectively, radians/second (unless noted otherwise)
$\bar{q}$	dynamic pressure, $\frac{1}{2}\rho V^2$, newtons/meters^2 (pounds/foot^2)
S	wing area, meters^2 (feet^2)
$T_{\frac{1}{2}}$	time required for absolute value of a transient oscillation to damp to one-half amplitude, seconds
$T_{\frac{1}{2}sp_1}$, $T_{\frac{1}{2}sp_2}$	time for aperiodic longitudinal short-period modes to damp to one-half amplitude, seconds
t	time, seconds
V	airspeed, meters/second (feet/second)
Y	dimensional side-force coefficient, $\frac{\text{Side force}}{mV}$, per second

$Y_{\beta} = \frac{\partial Y}{\partial \beta}$, per second-radian

$Y_{\delta_a} = \frac{\partial Y}{\partial \delta_a}$, per second-radian

$Y_{\delta_r} = \frac{\partial Y}{\partial \delta_r}$, per second-radian

α, β	angles of attack and sideslip, respectively, degrees or radians
Δ	change in value of any parameter from start time to current time
$\delta_e, \delta_a, \delta_r, \delta_{sb}$	average elevon, aileron, rudder, and speed brake deflections, respectively (trailing edge of elevator down, positive; total aileron deflection that produces right roll, positive; trailing edge of rudder to left, positive; brake open, positive), degrees or radians
ζ	ratio of actual damping to critical damping
Θ, φ	Euler angle of pitch and roll, respectively, degrees
ρ	mass density of air, kilograms/meter^3 (slugs/foot^3)
τ_r	roll mode time constant, seconds
τ_s	spiral mode time constant, seconds
$\angle\varphi/\beta$	phase angle between angle of roll and angle of sideslip, degrees
$\lvert\varphi\rvert/\lvert\beta\rvert$	magnitude of angle of roll to angle of sideslip

Subscripts:

$(\dot{\ })$	time derivative of quantity in brackets
$(\ )_o$	starting value of quantity in brackets
$(\ )_{av}$	average value over time being analyzed

VEHICLE DESCRIPTION

The HL-10 lifting body vehicle is a rocket-powered wingless configuration with a delta planform and negative camber. The vehicle's semimonocoque structure is constructed primarily of aluminum. Pertinent physical characteristics of the vehicle are presented in table 1. Figures 1(a) and 1(b) are photographs of the vehicle with the landing gear stowed and extended, respectively. Once the landing gear is extended, it cannot be retracted in flight.

The wing loading of the HL-10 vehicle was approximately 182.7 kilograms/meter^2 (37.5 pounds/foot^2) based on the reference planform area of 14.9 meters^2 (160 feet^2). The center of gravity after burnout was at approximately 53 percent of the body length.

Figure 2 is a three-view drawing of the vehicle showing body dimensions and the control surfaces. The elevons and rudders were the primary control surfaces. The elevons provided both pitch and roll control, and the rudders (on the center vertical stabilizer) provided directional control and, with a symmetrical outward deflection, functioned as a speed brake. These surfaces were positioned by hydraulic actuators.

Secondary control surfaces were on the tip fins and the upper surface of the elevons. These surfaces, which were positioned by electric motors, changed the basic configuration to provide additional stability at transonic Mach numbers. The deflections of the secondary surfaces for the subsonic and transonic vehicle configurations are given in the following table:

Configuration	Elevon flaps, degrees up from elevon	Speed brakes, degrees outboard from faired position	Tip-fin flaps, degrees from faired position	
			Inboard	Outboard
Subsonic	5	0	3	3
Transonic	30	8	32.5	30

A standard control stick and rudder pedals were connected by control cables and push rods to the control valves of the hydraulic actuators. Fore and aft movement of the control stick caused synchronous movement of the elevons for pitch control. Left and right movement of the control stick caused differential movement of the elevons for roll control. Rudder pedal displacement actuated the left and right surfaces of the split rudder for yaw control. Stick and rudder pedal forces were provided by coil spring bungees. Trim was accomplished by using electronic motors to change the neutral position of the coil spring bungees.

Stability augmentation systems provided damping inputs to the aerodynamic flight control surfaces in pitch, roll, and yaw. Control surface displacement was commanded in proportion to angular rate. The ratio of control surface displacement to angular rate was controlled by the pilot. Normal gains in flight were 0.4, 0.2, and 0.4 deg/deg/sec in pitch, roll, and yaw, respectively.

The HL-10 vehicle was powered by one four-chamber XLR11-13 rocket engine. A solution of 80 percent ethyl alcohol and 20 percent water was used as fuel, and liquid oxygen was used as an oxidizer. Each chamber was rated at approximately 8900 newtons (approximately 2000 pounds) of thrust. The rocket engine could be fired for approximately 360 chamber seconds with the fuel carried on the vehicle.

DATA ACQUISITION

Table 2 shows the parameters that were measured to determine stability and control characteristics. The table also lists the normal recording range of the instrument used and the range covered during maneuvers in terms of the normal change from a nominal value. The probable resolution of the parameter and the percentage of the nominal range used is shown. The instrumentation errors were much less than the basic resolution.

All parameters were sampled at 200 samples per second and were telemetered to a ground station, where the data were recorded in the form of bits on magnetic tape. Then the data were processed, corrected for instrument location, and plotted by using digital programs.

TEST PROCEDURES

The HL-10 vehicle was carried aloft under the wing of a B-52 airplane and launched at an altitude of approximately 13,716 meters (45,000 feet) and a Mach number of approximately 0.7. The rocket engine was fired after launch, and a planned Mach number and angle-of-attack profile was flown. After engine burnout the vehicle was glided to a landing site at Edwards Air Force Base.

The vehicle was unpowered for the test maneuvers, so flight time at a desired Mach number and angle of attack was short. Dynamic pressure changed significantly during most of the maneuvers because of the loss of altitude that accompanied the attempt to hold Mach number and angle of attack constant. Generally, the high angle-of-attack data were obtained at low dynamic pressure, and the low angle-of-attack data were obtained at high dynamic pressure. For most maneuvers the dampers were at a low gain. The longitudinal damper gains were 0 or 0.1 deg/deg/sec, and the lateral-directional damper gains were 0 or 0.1 deg/deg/sec in roll and 0.2 deg/deg/sec in yaw.

Data from several types of maneuvers were recorded and analyzed to determine the type of maneuver most suitable for stability derivative analysis. The lateral-directional maneuver selected was composed of a rudder pulse followed by a period without pilot control inputs and then an aileron pulse and recovery (fig. 3). The longitudinal maneuver was made up of a pitch control pulse followed by a period without pilot control input (fig. 4).

Only a limited number of test conditions and configurations could be investigated during the program. Stability and control maneuvers were performed at a Mach number of approximately 0.7 in the subsonic configuration and at Mach numbers of approximately 0.7, 0.9, and 1.2 in the transonic configuration to evaluate the effects of angle of attack. Also, stability and control maneuvers were performed at an angle of attack of 14° over the Mach number range from 0.6 to 1.4 to assess Mach number effects. Trim data were obtained over the entire Mach number and angle-of-attack range covered in the program.

METHOD OF ANALYSIS

An analog-matching technique, described in reference 10, was used to solve the equations of motion for the aerodynamic stability and control derivatives. This method of analysis is best suited for the analysis of airplane response data when significant changes in parameters such as dynamic pressure and angle of attack occur and when only one or two cycles of free oscillation are available for analysis. Several innovations to the basic analysis method were made during the program. A digital computer was used to generate the flight time histories at 50 samples per second. Previously, only the flight control inputs were generated and only a few data points were used to represent them. Also, the flight time history for the maneuver being analyzed was displayed on an oscilloscope together with the calculated time histories as standing waves. Before, the flight data were plotted on transparent overlays for comparison with scope displays of calculated time histories.

The equations of motion were rearranged (see appendix) so that solutions for matching could be obtained faster. Each equation could be solved independently or in combination with the other equations. For example, the $\dot{\beta}$ equation,

$$\Delta\dot{\beta} = \Delta p \sin(\alpha_o + \Delta\alpha) - \Delta r \cos(\alpha_o + \Delta\alpha) + \frac{g}{V}\left[\Delta a_t + \cos \Theta_o \sin(\varphi_o + \Delta\varphi)\right] - \dot{\beta}_o$$

could be solved using the actual flight values of $\Delta\beta$, Δr, Δp, $\Delta\alpha$, $\Delta\varphi$, and Δa_t (termed uncoupled operation), or could be solved using values from the complete equations of motion (coupled operation), or with any combination of equations. Because $\Delta\beta = \int \Delta\beta dt$, it could be compared with the flight-measured sideslip. The desired solution was obtained when the computed sideslip agreed with the flight-measured sideslip.

The α_o and $\dot{\beta}_o$ quantities were used in the uncoupled operation to determine the flight sideslip. Often, portions of the time histories could not be matched. The differences were apparently caused by gusts encountered by the vehicle, resulting in sideslip angles on the order of 0.5°. Because most planned maneuvers resulted in sideslip angles of 2° or less, sideslip was often used as a forcing function for the equations of motion.

Analysis of the longitudinal pulse data indicated that C_{m_α} appeared to be a function of elevator position. Therefore, the pilot input portion of the time histories was analyzed for the control derivatives, and the vehicle static and dynamic derivatives were obtained during periods without pilot inputs. Similarly, the rudder and aileron effectiveness derivatives were obtained during the portions of the time histories when the controls were used, and the vehicle static and dynamic lateral-directional derivatives were obtained during the periods of free vehicle response.

For the selected Mach numbers the experimental derivative data were faired as a function of angle of attack, and dynamic response parameters were calculated at various levels of dynamic pressure for comparison with similar parameters calculated from wind-tunnel data. The flight and vehicle conditions for which comparisons were made are shown in the following table:

M	$\bar{q}$, N/m^2 (lb/ft^2)	m, kg (slugs)	I_X, kg-m^2 (slug-ft^2)	I_Y, kg-m^2 (slug-ft^2)	I_Z, kg-m^2 (slug-ft^2)	I_{XZ}, kg-m^2 (slug-ft^2)
0.7	976.4 (200)	2933 (201)	1834.5 (1353)	8695.4 (6413)	10043.2 (7407)	541 (399)
.9	732.3 (150)	2933 (201)	1834.5 (1353)	8695.4 (6413)	10043.2 (7407)	541 (399)
1.2	488.2 (100)	2933 (201)	1834.5 (1353)	8695.4 (6413)	10043.2 (7407)	541 (399)

All results were corrected to a center of gravity of 53 percent of the body length. The wind-tunnel data were corrected to the required elevator position for trim.

PRESENTATION OF RESULTS

The flight results are presented and compared with wind-tunnel predictions in figures 5 to 22. (See following table.) Most of the wind-tunnel values were obtained from references 2 to 4. The rudder derivatives were obtained from references 5 and 6, and the rotary derivatives were obtained from references 7 and 8 and from estimates made by the Langley Research Center.

Title	Figure
Comparison of flight and wind-tunnel trim elevator deflection as a function of angle of attack.	5
Comparison of flight and wind-tunnel trim elevator deflection as a function of Mach number for an angle of attack of 14°. Transonic configuration.	6
Comparison of flight and wind-tunnel pitching-moment derivatives as a function of angle of attack.	7
Comparison of flight and wind-tunnel pitching-moment derivatives as a function of Mach number for an angle of attack of 14°. Transonic configuration.	8
Comparison of flight and wind-tunnel normal-force derivatives as a function of angle of attack.	9
Comparison of flight and wind-tunnel normal-force derivatives as a function of Mach number for an angle of attack of 14°. Transonic configuration.	10
Comparison of flight and wind-tunnel longitudinal period and time to damp to one-half amplitude as a function of angle of attack.	11
Comparison of flight and wind-tunnel sideslip derivatives as a function of angle of attack.	12
Comparison of flight and wind-tunnel sideslip derivatives as a function of Mach number for an angle of attack of 14°. Transonic configuration.	13
Comparison of flight and wind-tunnel aileron derivatives as a function of angle of attack.	14
Comparison of flight and wind-tunnel aileron derivatives as a function of Mach number for an angle of attack of 14°. Transonic configuration.	15
Comparison of flight and wind-tunnel rudder derivatives as a function of angle of attack.	16
Comparison of flight and wind-tunnel rudder derivatives as a function of Mach number for an angle of attack of 14°. Transonic configuration.	17
Comparison of flight and predicted damping derivatives as a function of angle of attack.	18
Comparison of flight and predicted damping derivatives as a function of Mach number for an angle of attack of 14°. Transonic configuration.	19
Comparison of flight and predicted lateral-directional period and time to damp to one-half amplitude as a function of angle of attack.	20
Comparison of flight and predicted roll spiral modes as a function of angle of attack.	21
Comparison of flight and predicted magnitude and phase angle of the ratio of roll angle to sideslip angle as a function of angle of attack.	22

RESULTS AND DISCUSSION

The results presented were obtained from an analysis of several maneuvers performed at Mach numbers within ±0.05 of specified Mach numbers less than 1.2 and within ±0.1 of Mach 1.2. The angle of attack cited is the average angle of attack during the maneuver analyzed; it generally remained within ±0.5° of the average value for the lateral-directional maneuvers.

Longitudinal Characteristics

The faired trim elevon deflections presented in figures 5 and 6 are representative of the data obtained in flight. The actual trim points were generally within one-half of a degree of the fairing shown. The variation of elevon deflection required for trim for any angle of attack was in general agreement with the wind-tunnel data at most Mach numbers; however, the values of elevon required were 2° to 3° less positive than predicted by the wind-tunnel measurements. The difference shown resulted from combined differences in longitudinal static stability and control effectiveness.

Before flight tests were made, there was concern that the change in predicted trim between $M = 0.95$ and 1.0 (fig. 5(e)) would affect controllability during rapid deceleration from supersonic to subsonic speeds. The flight-measured elevon for trim was approximately 2° less than predicted, but the trends were accurately predicted. However, the pilots compensated easily for the change in trim in this Mach region.

Figures 7 to 10 compare the flight- and wind-tunnel-measured longitudinal stability and control derivatives. In general, values of the derivatives are approximately in agreement with or slightly higher than the wind-tunnel-predicted values at subsonic Mach numbers and approximately in agreement with or slightly lower at supersonic Mach numbers. The differences shown do not result in significantly different vehicle behavior during flight, as indicated by the calculated periods and the time to damp in figure 11. The flight-derived periods were similar to those predicted from wind-tunnel data. The pilots did not notice the difference in period between flight and the ground-based simulation. However, they did notice the greater magnitude of damping that existed in flight below Mach 1.0, possibly because the flight longitudinal damping derivative was somewhat larger than the estimated derivative or the flight control effectiveness was greater, or both, since most flying was done with the pitch damper on except when derivative data were being obtained. At supersonic speeds damping was somewhat less than predicted and longitudinal dampers were used. With dampers on at subsonic speeds, the longitudinal short period became two aperiodic modes; however, both were positively damped. The pilots did not notice the change from periodic to aperiodic modes on either the flight vehicle or the ground-based simulator.

Lateral-Directional Characteristics

Figures 12 to 19 compare the flight- and wind-tunnel-measured lateral-directional stability, control, and damping derivatives. In general, agreement was satisfactory; there were only minor differences between the flight characteristics and the wind-tunnel data. The only difference the pilots noticed was that the lateral-directional damping in flight was higher than the predicted values. This was attributed largely to differences between estimated and flight-determined values of C_{l_p} and C_{n_p}. Although figure 20(a) shows good agreement in the flight and wind-tunnel damping characteristics, the differences in damping are apparent in figures 20(b) to 20(d). These figures show a time to damp to half amplitude at low angles of attack of about 1 second less in flight than predicted. A different trend between flight and wind-tunnel damping characteristics with angle of attack is apparent in figure 20(d) at supersonic speed without the dampers. The lateral-directional dampers were especially appreciated at high angles of attack where damping was very low.

Figure 21 presents values of the roll spiral modes, $1/\tau_r$ and $1/\tau_s$, as a function of angle of attack with the lateral and directional dampers on and off derived from flight and wind-tunnel data. With the dampers off, a coupled roll-spiral mode formed in flight at low angles of attack at $M = 0.7$ (subsonic configuration) and 1.2 (transonic configuration). At $M = 0.9$ with the dampers off, predictions indicated that the coupled roll-spiral mode formed in the mid-angle-of-attack range. The vehicle was not flown with the dampers off in areas where the roll spiral could be encountered, so roll-spiral dynamics were not encountered in flight. Lifting body flight experience is summarized and the roll-spiral mode is analyzed in reference 11.

Figure 22 presents the amplitude ratio and phase angle of $|\varphi|/|\beta|$ as a function of angle of attack for Mach numbers of 0.7, 0.9, and 1.2. With lateral and directional dampers on and off, some differences may be noted between the flight and wind-tunnel-predicted characteristics; however, the pilots did not notice any differences between the characteristics of the flight vehicle and those of the fixed-base simulator except for the generally higher damping of the flight vehicle.

CONCLUDING REMARKS

Flight maneuvers performed with the HL-10 lifting body vehicle were analyzed to determine aerodynamic stability and control derivatives. Comparison of these results with wind-tunnel-measured derivatives showed little or no significant difference between the values, with the possible exception of the longitudinal and lateral damping derivatives. The elevon deflection required for longitudinal trim was approximately 2° to 3° less positive than predicted by the wind-tunnel results; however, the variation of elevon deflection with angle of attack and Mach number was similar to predictions. Although differences were noted in the dynamic response characteristics calculated from flight and wind-tunnel-measured derivatives, the pilots noticed only that the damping in flight was higher than that in the ground-based simulator which was programed with wind-tunnel predictions.

Innovations were made in the basic analog-matching method of analysis, including the use of sideslip resulting from gusts as a forcing function, to permit faster analysis of the flight data for flight derivatives.

Flight Research Center,
National Aeronautics and Space Administration,
Edwards, Calif., May 5, 1972.

APPENDIX

EQUATIONS USED TO DETERMINE AERODYNAMIC DERIVATIVES

The equations used in the analog-digital system to determine the aerodynamic derivatives are presented in this appendix. Because of zero shifts in measuring the flight data, $\dot{\alpha}_o$, $\dot{\Theta}_o$, $\dot{q}_o$, $\dot{\beta}_o$, $\dot{\varphi}_o$, $\dot{r}_o$, and $\dot{p}_o$ terms were used to balance out the equations.

The longitudinal equations used on the analog computer were:

$$\Delta\dot{\alpha} = \Delta q + \frac{g}{V_{av}}\left[\cos(\Theta_o + \Delta\Theta)\cos(\varphi_o + \Delta\varphi) - \Delta a_n\right]\cos(\alpha_o + \Delta\alpha)$$

$$+ \frac{g}{V_{av}}\left[\sin(\Theta_o + \Delta\Theta) - \Delta a_x\right]\sin(\alpha_o + \Delta\alpha) - \dot{\alpha}_o$$

$$\Delta\Theta = \Delta q\cos(\varphi_o + \Delta\varphi) - \dot{\Theta}_o$$

$$\Delta\dot{q} = \left(\frac{\bar{q}_o + \Delta\bar{q}}{\bar{q}_{av}}\right)\left[M_\alpha\Delta\alpha + M_{\delta_e}\Delta\delta_e + (M_q + M_{\dot{\alpha}})\,\Delta q\right] - \dot{q}_o$$

$$\Delta a_n = \left[\bar{N}_\alpha\Delta\alpha + \bar{N}_{\delta_e}\Delta\delta_e + (\bar{N}_q + \bar{N}_{\dot{\alpha}})\Delta q\right]\left(\frac{\bar{q}_o + \Delta\bar{q}}{\bar{q}_{av}}\right)\left(\frac{V_{av}}{g}\right)$$

$$\Delta a_x = \left(C_\alpha\Delta\alpha + C_{\delta_e}\Delta\delta_e + C_q\Delta q\right)\left(\frac{\bar{q}_o + \Delta\bar{q}}{\bar{q}_{av}}\right)\left(\frac{V_{av}}{g}\right)$$

The longitudinal equations used in the digital computer to reduce the data were:

$$C_{m_\alpha} = \frac{I_Y}{S\bar{c}\bar{q}_{av}}\,\frac{M_\alpha}{57.3}$$

$$C_{m_{\delta_e}} = \frac{I_Y}{S\bar{c}\bar{q}_{av}}\,\frac{M_{\delta_e}}{57.3}$$

$$C_{m_q} + C_{m_{\dot{\alpha}}} = \frac{2V_{av}I_Y}{S\bar{c}^2\bar{q}_{av}}(M_q + M_{\dot{\alpha}})$$

$$C_{N_\alpha} = \frac{mV_{av}}{S\bar{q}_{av}} \frac{\bar{N}_\alpha}{57.3}$$

$$C_{N_{\delta_e}} = \frac{mV_{av}}{S\bar{q}_{av}} \frac{\bar{N}_{\delta_e}}{57.3}$$

$$C_{N_q} = \frac{2mV_{av}^2}{S\bar{c}\bar{q}_{av}} \bar{N}_q$$

$$C_{c_\alpha} = \frac{mV_{av}}{S\bar{q}_{av}} \frac{C_\alpha}{57.3}$$

$$C_{c_{\delta_e}} = \frac{mV_{av}}{S\bar{q}_{av}} \frac{C_{\delta_e}}{57.3}$$

$$C_{c_q} = \frac{2mV_{av}^2}{S\bar{c}\bar{q}_{av}} C_q$$

The lateral-directional equations used on the analog computer were:

$$\Delta\dot{\beta} = \Delta p \sin(\alpha_o + \Delta\alpha) - \Delta r \cos(\alpha_o + \Delta\alpha) + \frac{g}{V}\left[\Delta a_t + \cos\Theta_o \sin(\varphi_o + \Delta\varphi)\right] - \dot{\beta}_o$$

$$\Delta\dot{\varphi} = \Delta p + \Delta r \cos(\varphi_o + \Delta\varphi)\tan\Theta_o - \dot{\varphi}_o$$

$$\Delta\dot{r} = \left[N'_\beta \Delta\beta + (N'_r - N'_{\dot{\beta}} \cos\alpha)\Delta r + (N'_p + N'_{\dot{\beta}} \sin\alpha)\Delta p + N'_{\delta_a}\Delta\delta_a + N'_{\delta_r}\Delta\delta_r\right]\left(\frac{\bar{q}_o + \Delta\bar{q}}{\bar{q}_{av}}\right) - \dot{r}_o$$

$$\Delta\dot{p} = \left[L'_\beta \Delta\beta + (L'_r - L'_{\dot{\beta}} \cos\alpha)\Delta r + (L'_p + L'_{\dot{\beta}} \sin\alpha)\Delta p + L'_{\delta_a}\Delta\delta_a + L'_{\delta_r}\Delta\delta_r\right]\left(\frac{\bar{q}_o + \Delta\bar{q}}{\bar{q}_{av}}\right) - \dot{p}_o$$

$$\Delta a_t = \frac{V_{av}}{g}\left(Y_\beta \Delta\beta + Y_{\delta_r}\Delta\delta_r + Y_{\delta_a}\Delta\delta_a\right)\left(\frac{\bar{q}_o + \Delta\bar{q}}{\bar{q}_{av}}\right)$$

The lateral-directional equations used in the digital computer to reduce the data were:

$$C_{l_\beta} = \frac{I_X}{\bar{q}_{av}Sb}\left(\frac{L'_\beta - \frac{I_{XZ}}{I_X}N'_\beta}{57.3}\right)$$

$$C_{l_{\delta_a}} = \frac{I_X}{\bar{q}_{av}Sb}\left(\frac{L'_{\delta_a} - \frac{I_{XZ}}{I_X}N'_{\delta_a}}{57.3}\right)$$

$$C_{l_{\delta_r}} = \frac{I_X}{\bar{q}_{av}Sb}\left(\frac{L'_{\delta_r} - \frac{I_{XZ}}{I_X}N'_{\delta_r}}{57.3}\right)$$

$$C_{l_p} + C_{l_{\dot{\beta}}} \sin\alpha = \frac{2I_X V_{av}}{\bar{q}_{av}Sb^2}\left[L'_p + L'_{\dot{\beta}} \sin\alpha - \frac{I_{XZ}}{I_X}(N'_p + N'_{\dot{\beta}} \sin\alpha)\right]$$

$$C_{l_r} - C_{l_{\dot{\beta}}} \cos\alpha = \frac{2I_X V_{av}}{\bar{q}_{av}Sb^2}\left[L'_r - L'_{\dot{\beta}} \cos\alpha - \frac{I_{XZ}}{I_X}(N'_r - N'_{\dot{\beta}} \cos\alpha)\right]$$

$$C_{n_\beta} = \frac{I_Z}{\bar{q}_{av}Sb}\left(\frac{N'_\beta - \frac{I_{XZ}}{I_Z}L'_\beta}{57.3}\right)$$

$$C_{n_{\delta_a}} = \frac{I_Z}{\bar{q}_{av}Sb}\left(\frac{N'_{\delta_a} - \frac{I_{XZ}}{I_Z}L'_{\delta_a}}{57.3}\right)$$

$$C_{n_{\delta_r}} = \frac{I_Z}{\bar{q}_{av}Sb}\left(\frac{N'_{\delta_r} - \frac{I_{XZ}}{I_Z}L'_{\delta_r}}{57.3}\right)$$

$$C_{n_p} + C_{n_{\dot{\beta}}} \sin\alpha = \frac{2I_Z V_{av}}{\bar{q}_{av}Sb^2}\left[N'_p + N'_{\dot{\beta}} \sin\alpha - \frac{I_{XZ}}{I_Z}(L'_p + L'_{\dot{\beta}} \sin\alpha)\right]$$

$$C_{n_r} - C_{n_{\dot{\beta}}} \cos \alpha = \frac{2I_Z V_{av}}{\bar{q}_{av} S b^2}\left[N'_r - N'_{\dot{\beta}} \cos \alpha - \frac{I_{XZ}}{I_Z}\left(L'_r - L'_{\dot{\beta}} \cos \alpha\right)\right]$$

$$C_{Y_\beta} = \frac{mV_{av}}{S\bar{q}_{av}} \; \frac{Y_\beta}{57.3}$$

$$C_{Y_{\delta_a}} = \frac{mV_{av}}{S\bar{q}_{av}} \; \frac{Y_{\delta_a}}{57.3}$$

$$C_{Y_{\delta_r}} = \frac{mV_{av}}{S\bar{q}_{av}} \; \frac{Y_{\delta_r}}{57.3}$$

REFERENCES

1. Kempel, Robert W.; Strutz, Larry W.; and Kirsten, Paul W.: Stability and Control Derivatives of the Lifting Body Vehicles. Flight Test Results Pertaining to the Space Shuttlecraft. NASA TM X-2101, 1970, pp. 11-27.

2. McKinney, Linwood W.; and Huffman, Jarrett K.: Subsonic Aerodynamic Characteristics of a Model of the HL-10 Flight Research Vehicle With Basic and Modified Tip Fins. NASA TM X-2119, 1971.

3. Ladson, Charles L.; and Hill, Acquilla S.: Aerodynamics of a Model of the HL-10 Flight-Test Vehicle at Mach 0.35 to 1.80. NASA TN D-6018, 1971.

4. Ware, George M.: Aerodynamic Characteristics of Models of Two Thick 74° Delta Manned Lifting Entry Vehicles at Low-Subsonic Speeds. NASA TM X-914, 1964.

5. Harris, Charles D.: Transonic Aerodynamic Characteristics of a Manned Lifting Entry Vehicle With and Without Tip Fins. NASA TM X-1248, 1966.

6. Henderson, William P.: Static Stability Characteristics of a Manned Lifting Entry Vehicle at High Subsonic Speeds. NASA TM X-1349, 1967.

7. Wiley, Harleth G.; and Brower, Margaret L.: Damping and Oscillatory Stability in Pitch and Yaw for a Model of an HL-10 Configuration at Mach Numbers From 0.20 to 1.00. NASA TM X-1467, 1967.

8. Ware, George M.: Investigation of the Flight Characteristics of a Model of the HL-10 Manned Lifting Entry Vehicle. NASA TM X-1307, 1967.

9. Mechtly, E. A.: The International System of Units – Physical Constants and Conversion Factors. NASA SP-7012, 1969.

10. Wolowicz, Chester H.; Strutz, Larry W.; Gilyard, Glenn B.; and Matheny, Neil W.: Preliminary Flight Evaluation of the Stability and Control Derivatives and Dynamic Characteristics of the Unaugmented XB-70-1 Airplane Including Comparisons With Predictions. NASA TN D-4578, 1968.

11. Kempel, Robert W.: Analysis of a Coupled Roll-Spiral-Mode, Pilot-Induced Oscillation Experienced With the M2-F2 Lifting Body. NASA TN D-6496, 1971.

TABLE 1. – PHYSICAL CHARACTERISTICS OF THE HL-10 VEHICLE

Body -	
Planform area, meters^2 (feet^2)	14.9 (160)
Length, meters (feet)	6.45 (21.17)
Span, meters (feet)	4.15 (13.6)
Aspect ratio (basic vehicle), $\frac{b^2}{S}$	1.156
Weight, including pilot, kilograms (pounds)	2722 (6000)
Center of gravity, percentage of reference length	53
Base area:	
Subsonic configuration, meters^2 (feet^2)	1.38 (14.83)
Transonic configuration	2.71 (29.13)
Elevons (two) -	
Area, each, meters^2 (feet^2)	1.00 (10.72)
Span, each, parallel to hinge line, meters (feet)	1.09 (3.58)
Chord, perpendicular to hinge line, meters (feet):	
Root	0.59 (1.93)
Tip	1.24 (4.06)
Elevon flaps (two) -	
Area, each, meters^2 (feet^2)	0.70 (7.50)
Span, each, parallel to hinge line, meters (feet)	1.09 (3.58)
Chord, perpendicular to hinge line, meters (feet):	
Root	0.48 (1.58)
Tip	0.80 (2.63)
Vertical stabilizer (one) -	
Area, meters^2 (feet^2)	1.47 (15.8)
Height, trailing edge, meters (feet)	1.53 (5.02)
Chord, meters (feet):	
Root	1.32 (4.32)
Tip	0.60 (1.97)
Leading-edge sweep, degrees	25
Rudders (two) -	
Area, each, meters^2 (feet^2)	0.41 (4.45)
Height, each, meters (feet)	1.26 (4.12)
Chord, meters (feet)	0.33 (1.08)
Outboard tip-fin flaps (two) -	
Area, each, meters^2 (feet^2)	0.35 (3.77)
Height, hinge line, meters (feet)	1.37 (4.50)
Chord, perpendicular to hinge line, meters (feet)	0.26 (0.84)
Inboard tip-fin flaps (two) -	
Area, each, meters^2 (feet^2)	0.23 (2.48)
Height, hinge line, meters (feet)	1.01 (3.31)
Chord, perpendicular to hinge line, meters (feet)	0.23 (0.75)

TABLE 2. – PARAMETERS MEASURED TO DETERMINE STABILITY AND CONTROL CHARACTERISTICS, INCLUDING PARAMETER RESOLUTION

Parameter	Range	Range covered during maneuvers	Processing resolution	Matching system resolution	Probable resolution	
					Absolute value	Percent of range used
α	-5° to 35°	±5°	0.2°	0.124°	0.235°	4.7
Θ	-30° to 60°	±5°	.3°	.062°	.306°	6.1
q	±40 deg/sec	±10 deg/sec	.5 deg/sec	.124 deg/sec	.515 deg/sec	5.1
a_n	-1g to 3g	±.5g	.03g	.004g	.030g	6.0
β	±10°	±2°	.2°	.012°	.20°	10.0
φ	±95°	±20°	1.44°	.12°	1.44°	7.2
p	±40 deg/sec	±30 deg/sec	.55 deg/sec	.124 deg/sec	.56 deg/sec	1.9
r	±40 deg/sec	±5 deg/sec	.5 deg/sec	.062 deg/sec	.50 deg/sec	10.1
a_t	±.5g	±.1g	.016g	.001g	.016g	16.0
$\delta_{e_{left}}$	8° to -32°	±5°	.3°	.062°	[1] .43°	8.7
$\delta_{e_{right}}$	8° to -32°	±5°	.3°	.062°	[1] .43°	8.7
δ_r	10° to -40°	±5°	.3°	.062°	[1] .43°	8.7

[1] Probable error is for two surfaces.

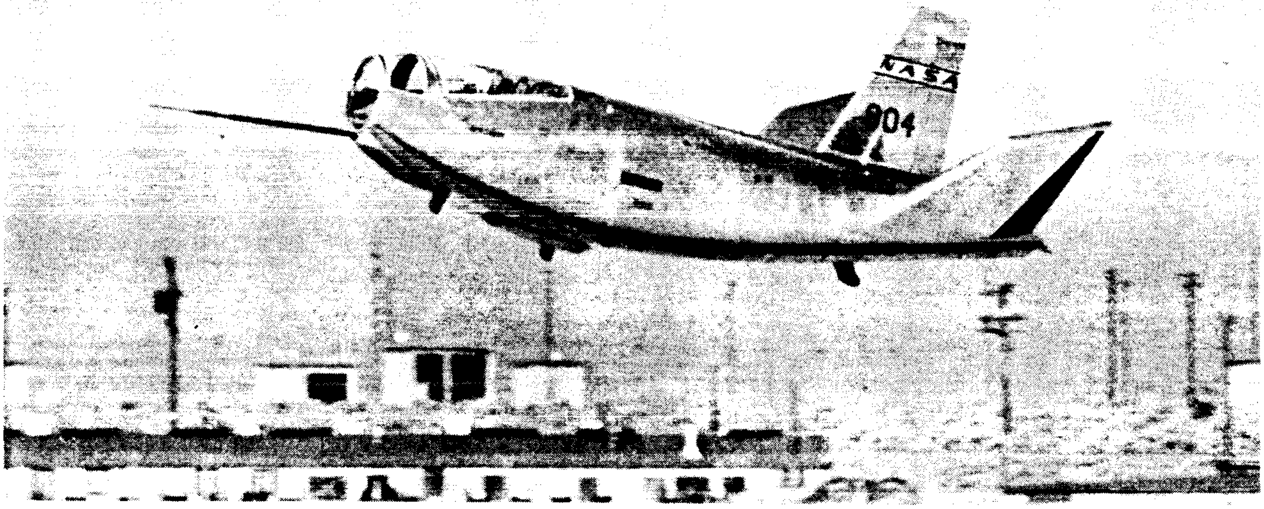

(a) Gear up.

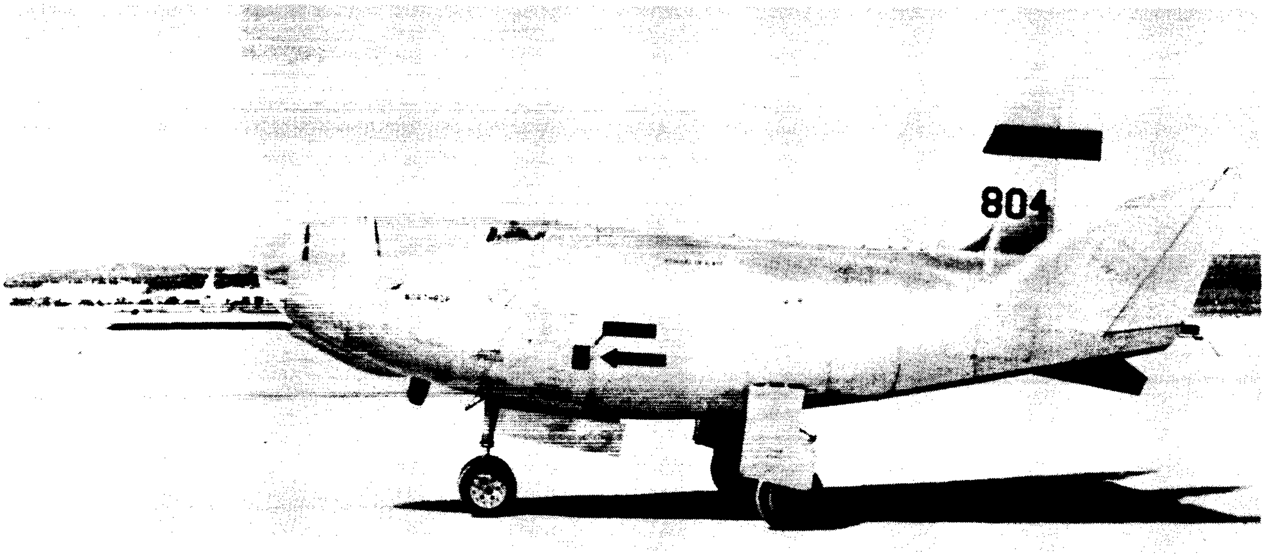

(b) Gear down.

Figure 1. HL-10 vehicle.

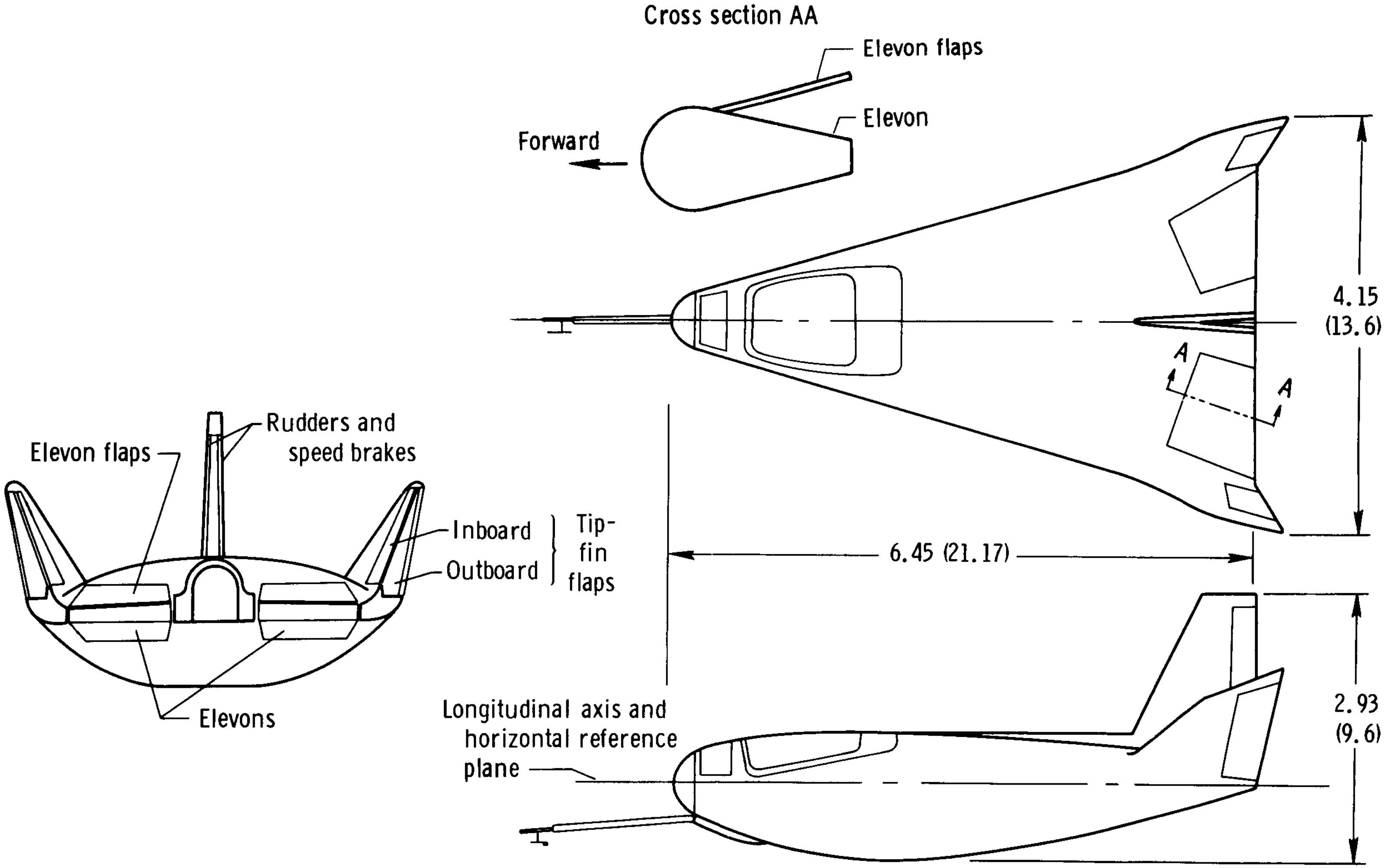

Figure 2. Three-view drawing of the HL-10 vehicle. Dimensions in meters (feet).

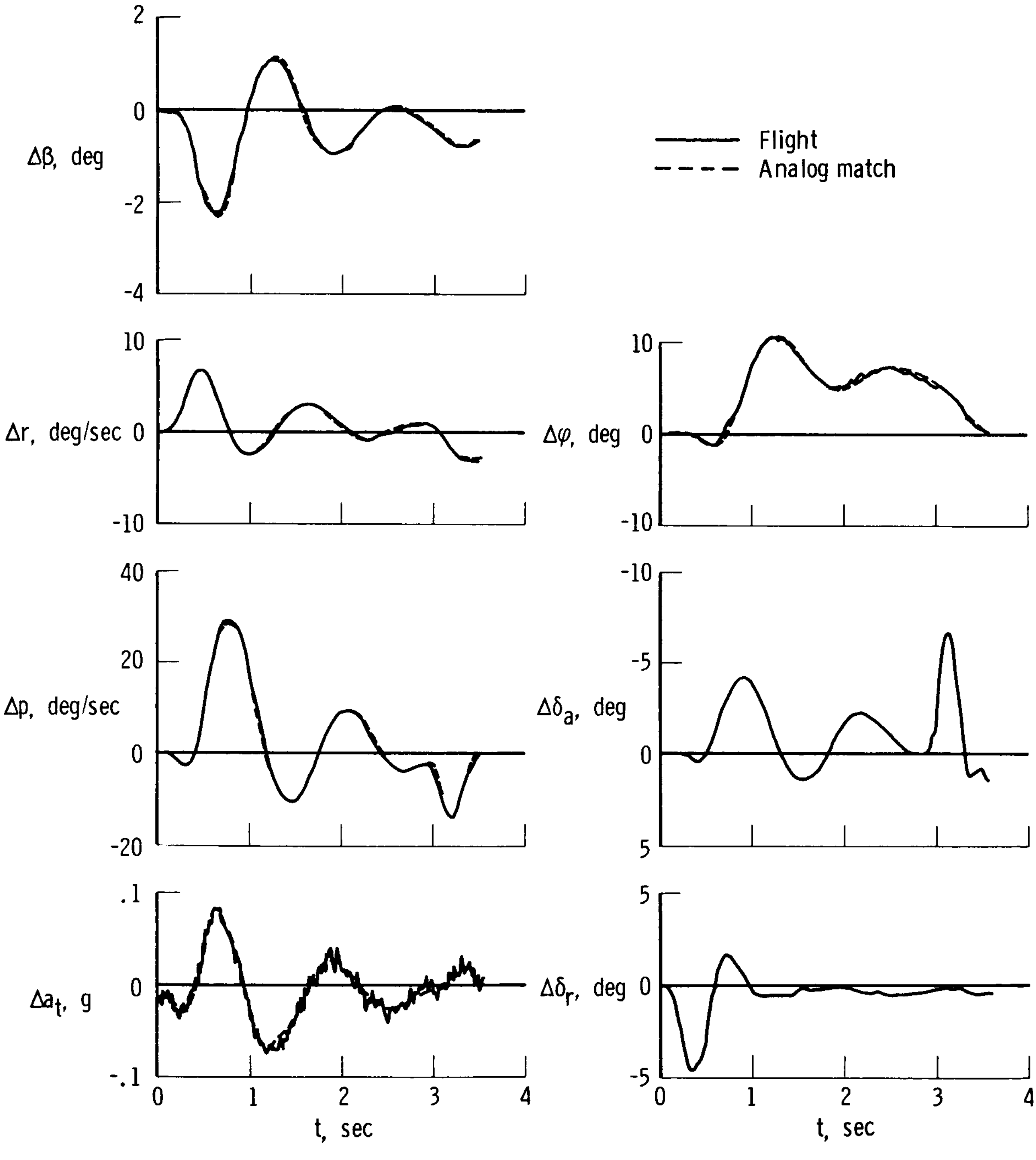

Figure 3. Comparison of lateral-directional flight time history with analog match. M = 0.88; α = 11.5°; transonic configuration.

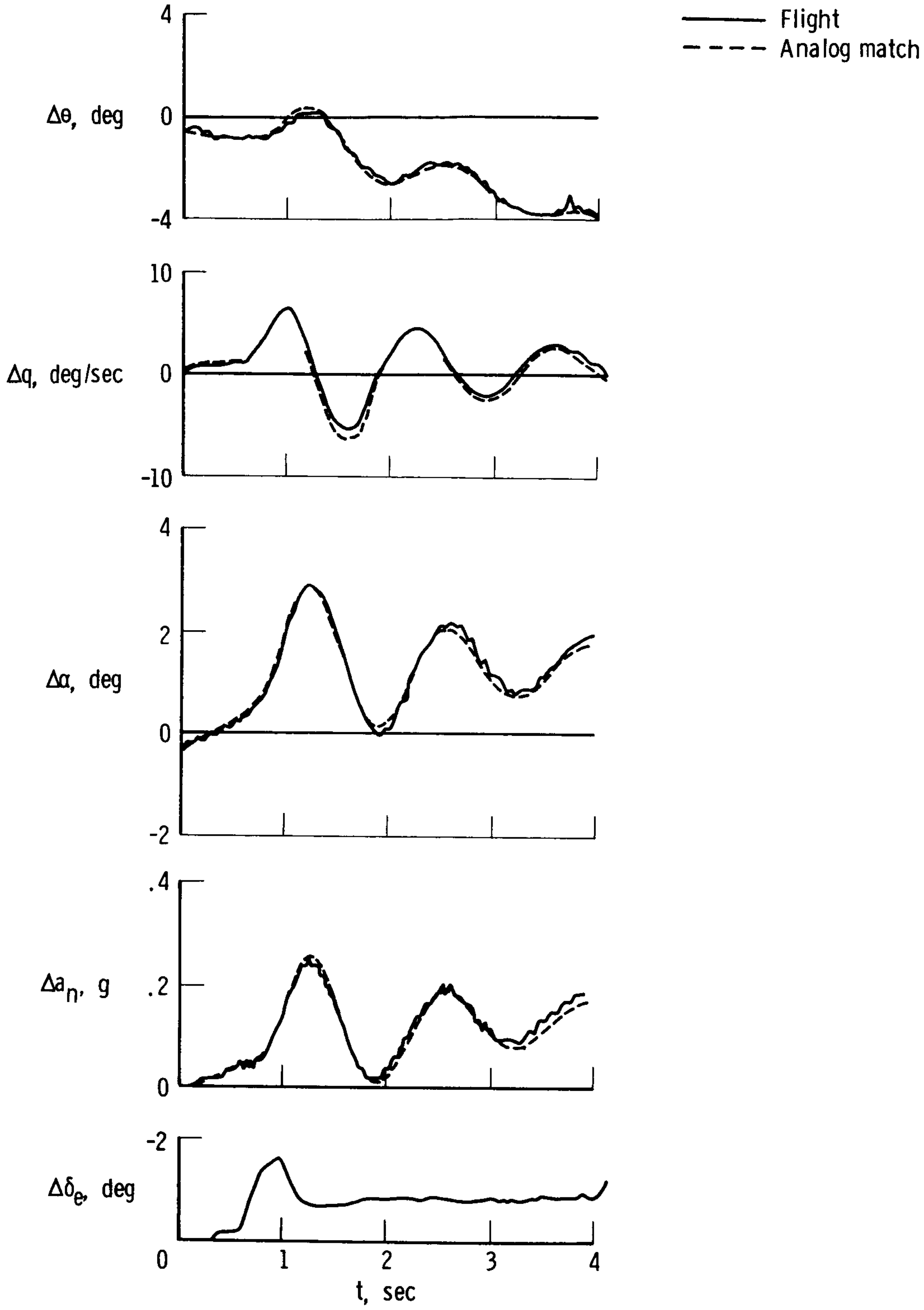

Figure 4. Comparison of longitudinal flight time history with analog match. M = 0.64; α = 9.1°; transonic configuration.

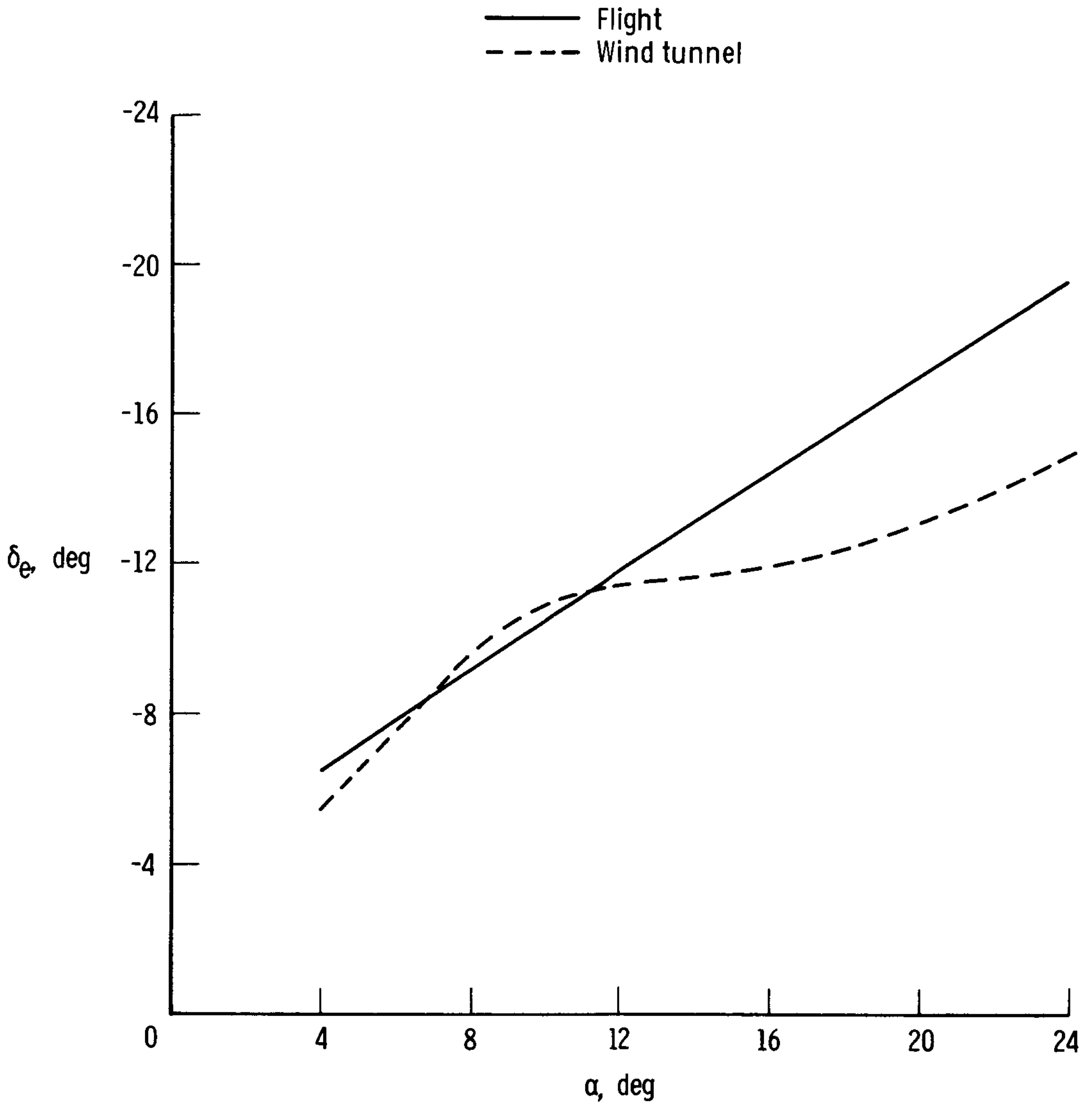

(a) M = 0.7, subsonic configuration.

Figure 5. Comparison of flight and wind-tunnel trim elevator deflection as a function of angle of attack.

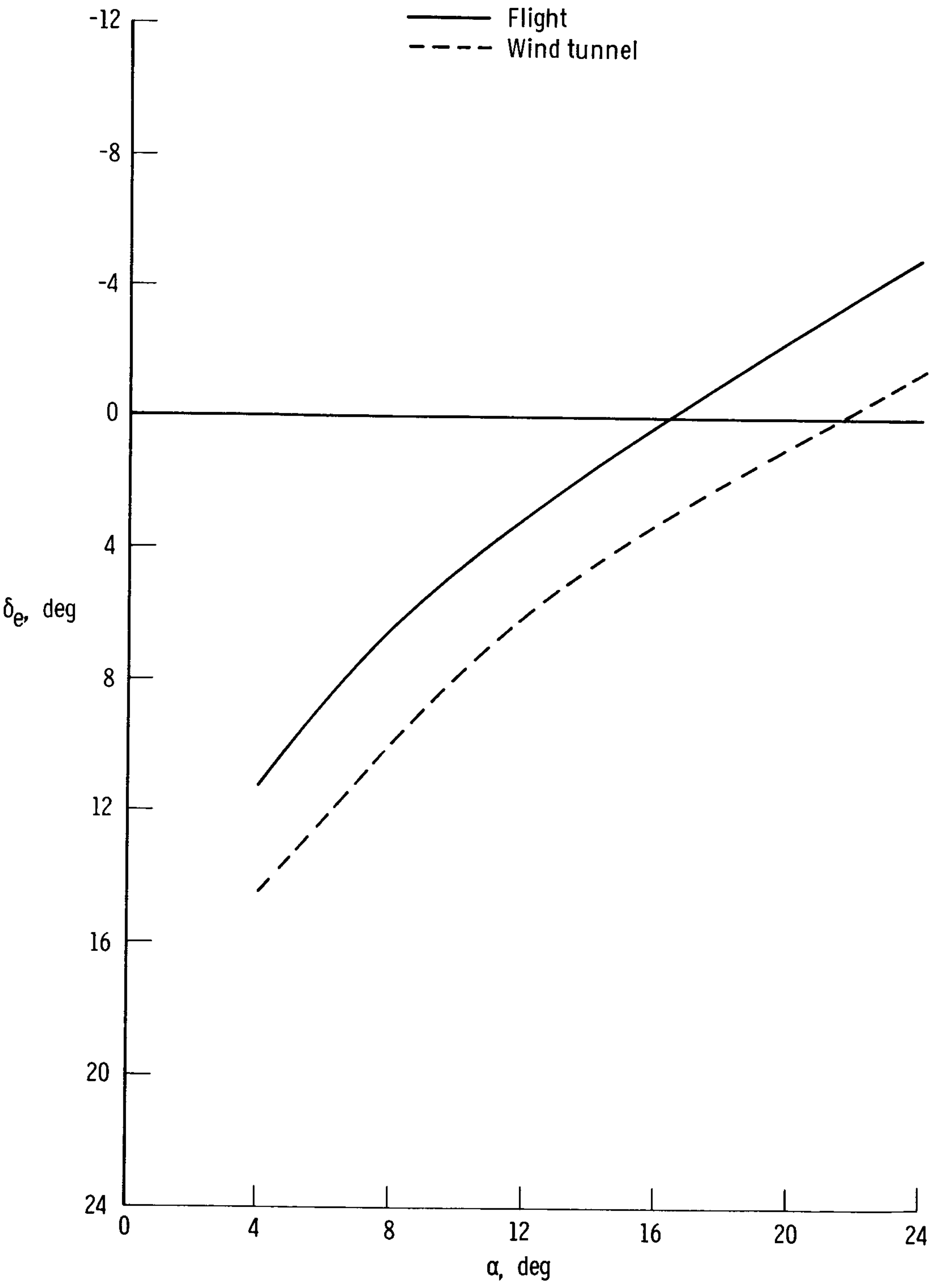

(b) M = 0.7, transonic configuration.

Figure 5. Continued.

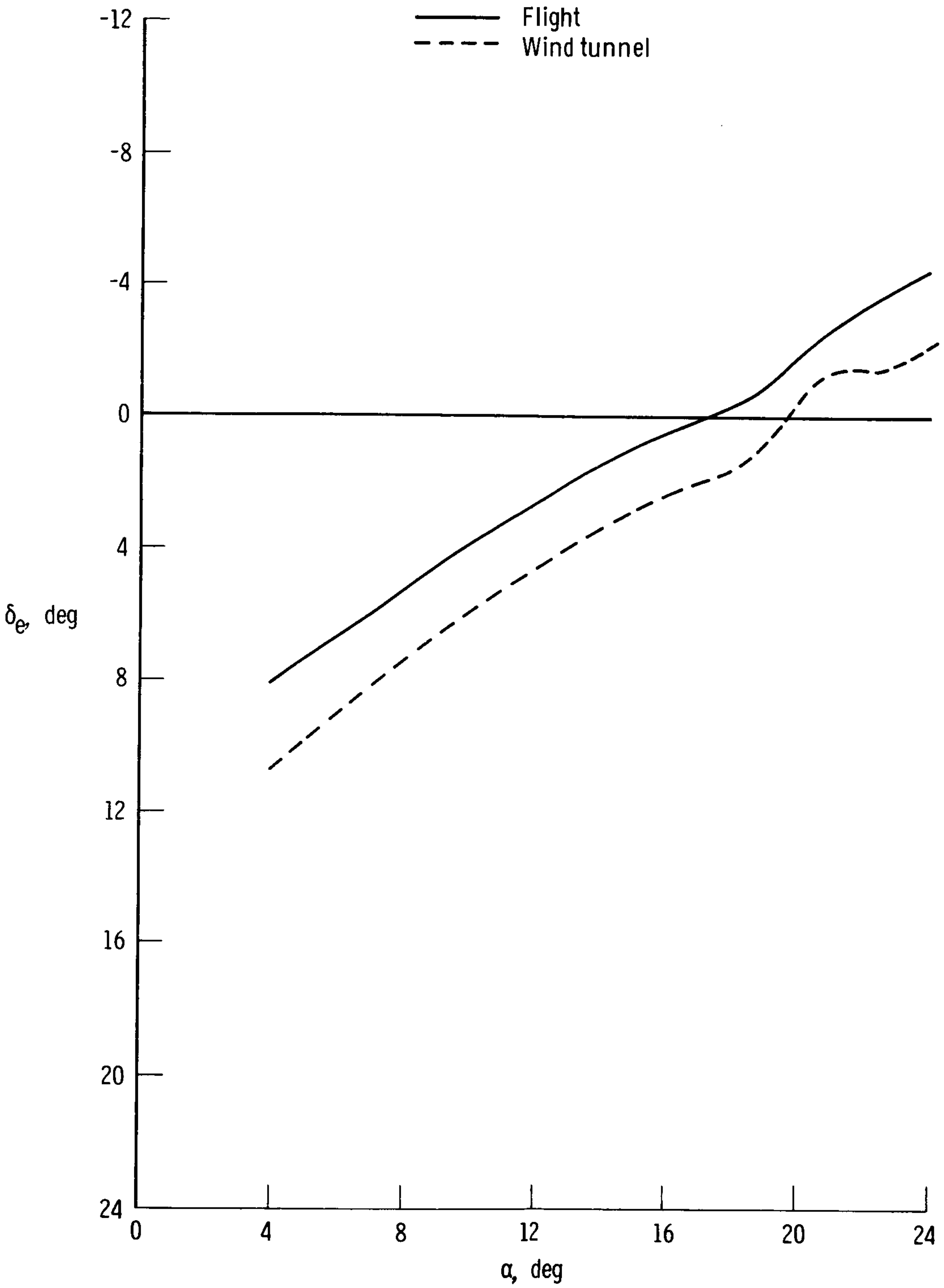

(c) M = 0.9, transonic configuration.

Figure 5. Continued.

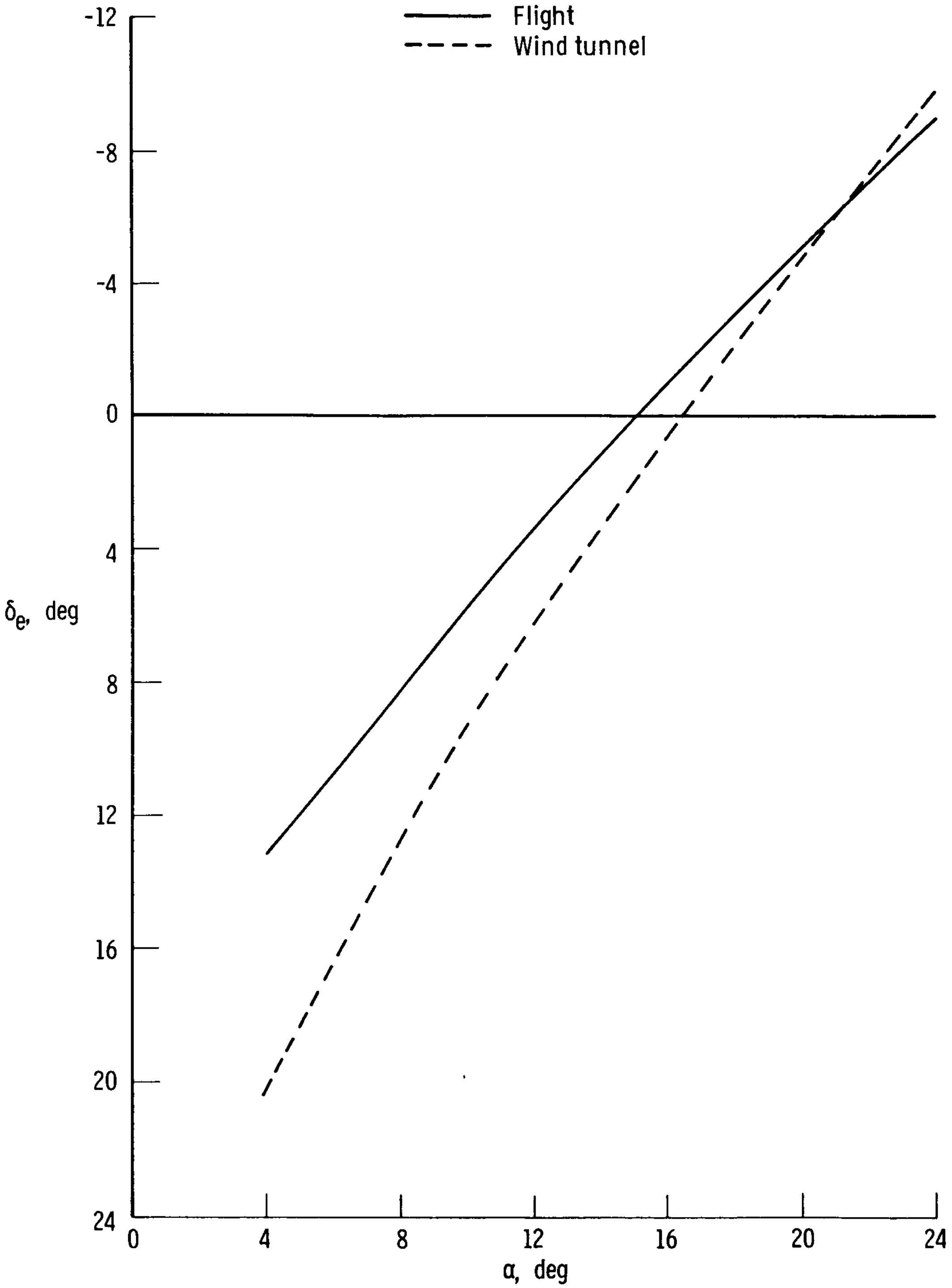

(d) M = 1.2, transonic configuration.

Figure 5. Continued.

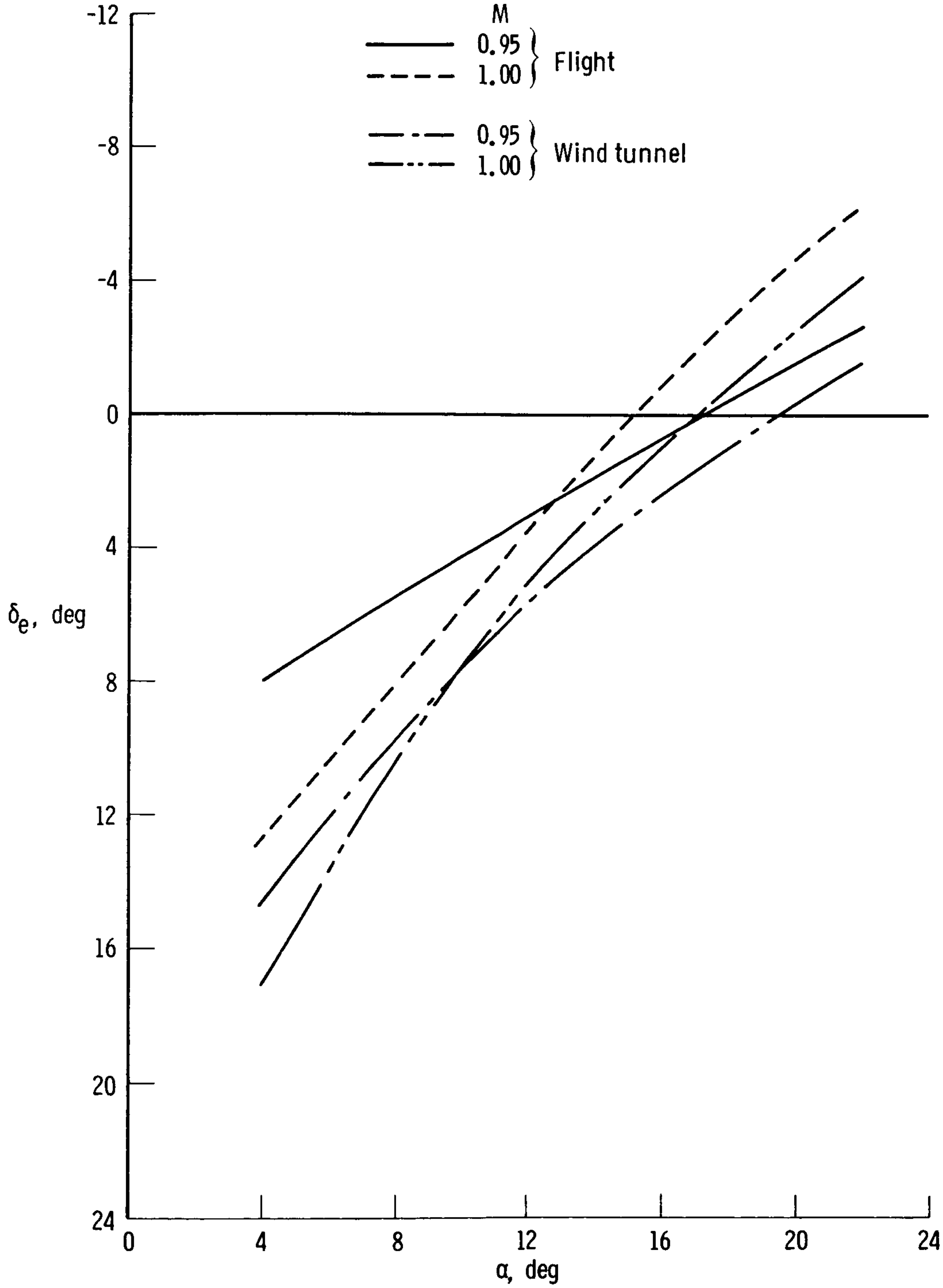

(e) M = 0.95 and 1.0, transonic configuration.

Figure 5. Concluded.

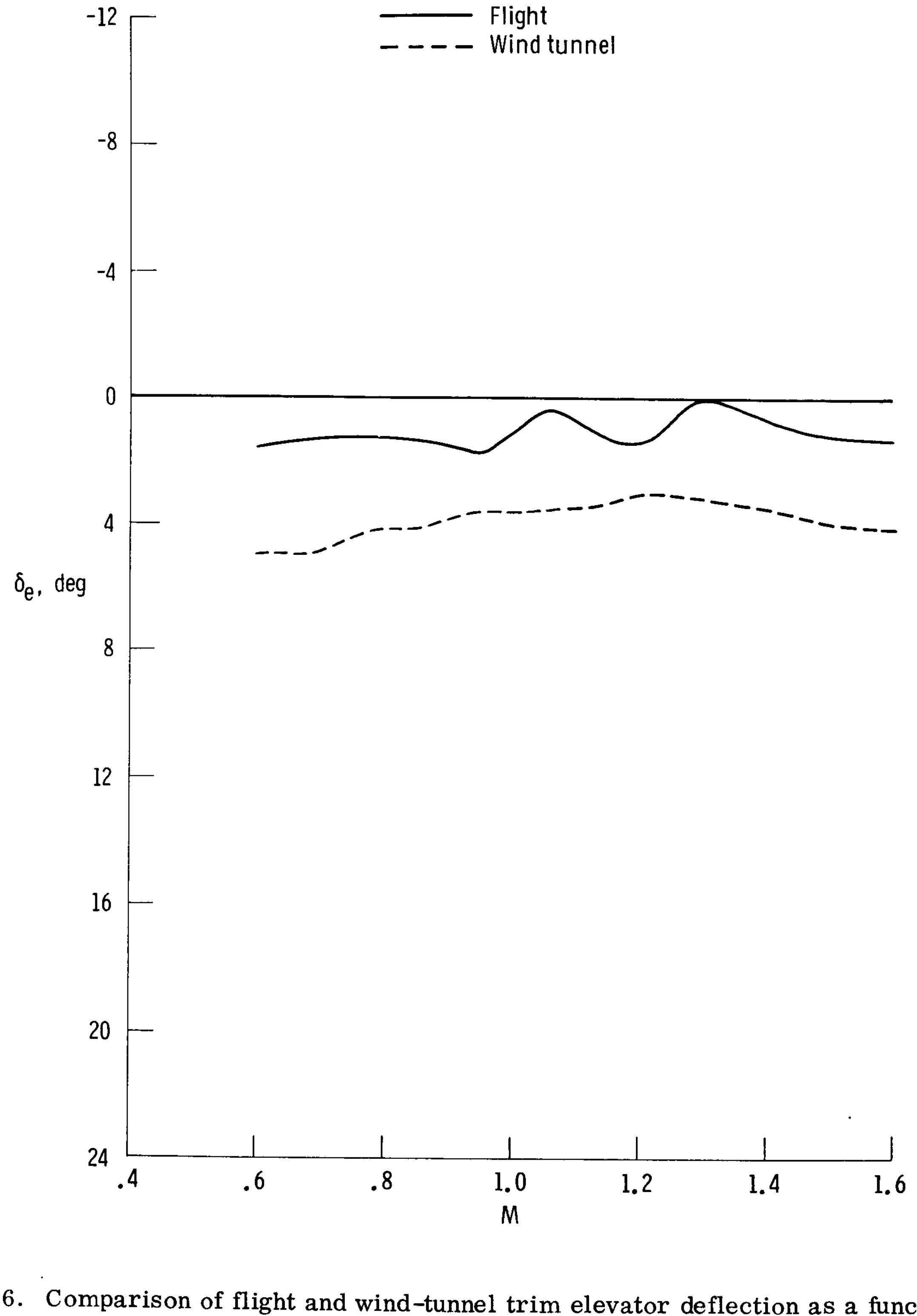

Figure 6. Comparison of flight and wind-tunnel trim elevator deflection as a function of Mach number for an angle of attack of 14°. Transonic configuration.

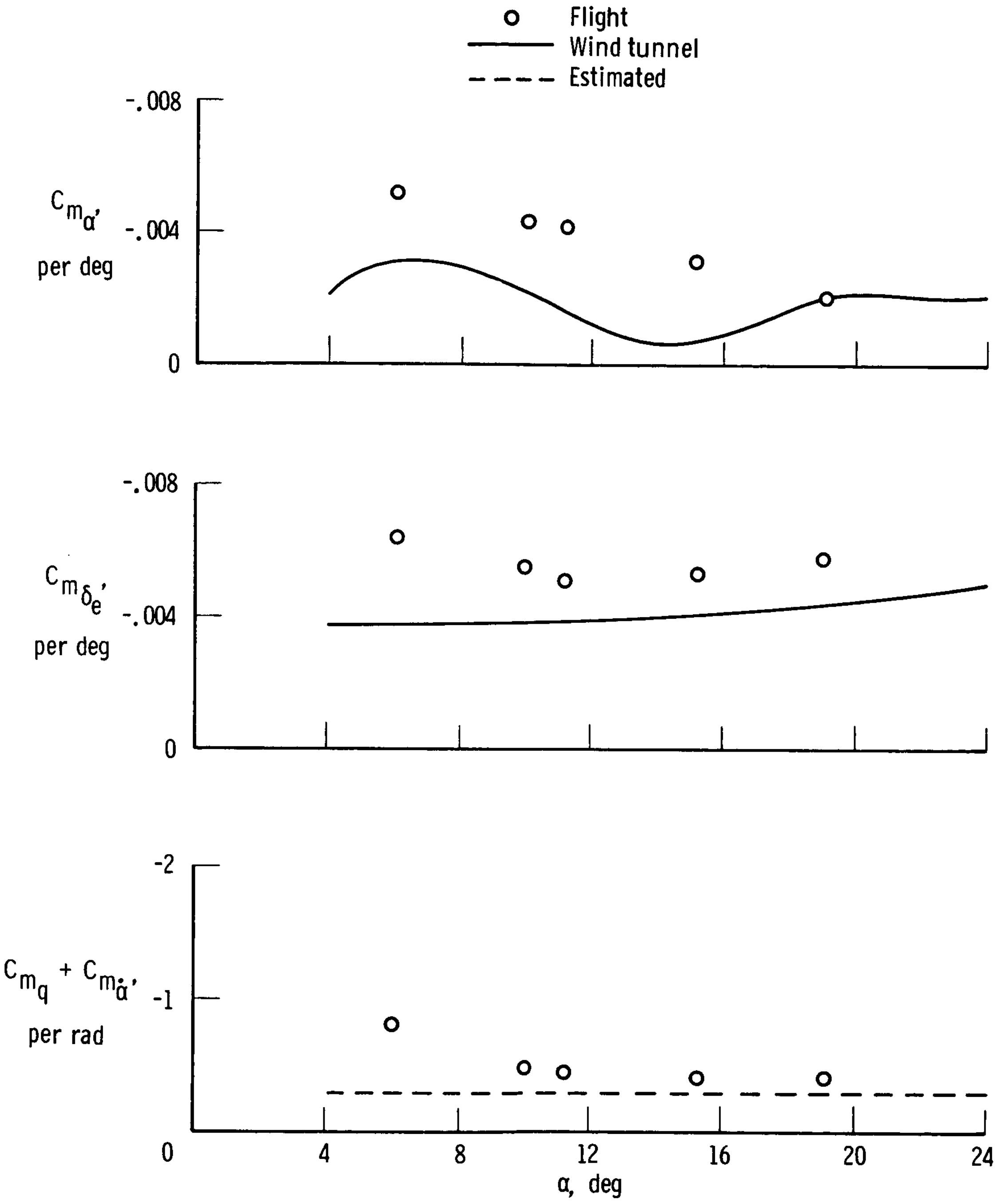

(a) M = 0.7, subsonic configuration.

Figure 7. Comparison of flight and wind-tunnel pitching-moment derivatives as a function of angle of attack.

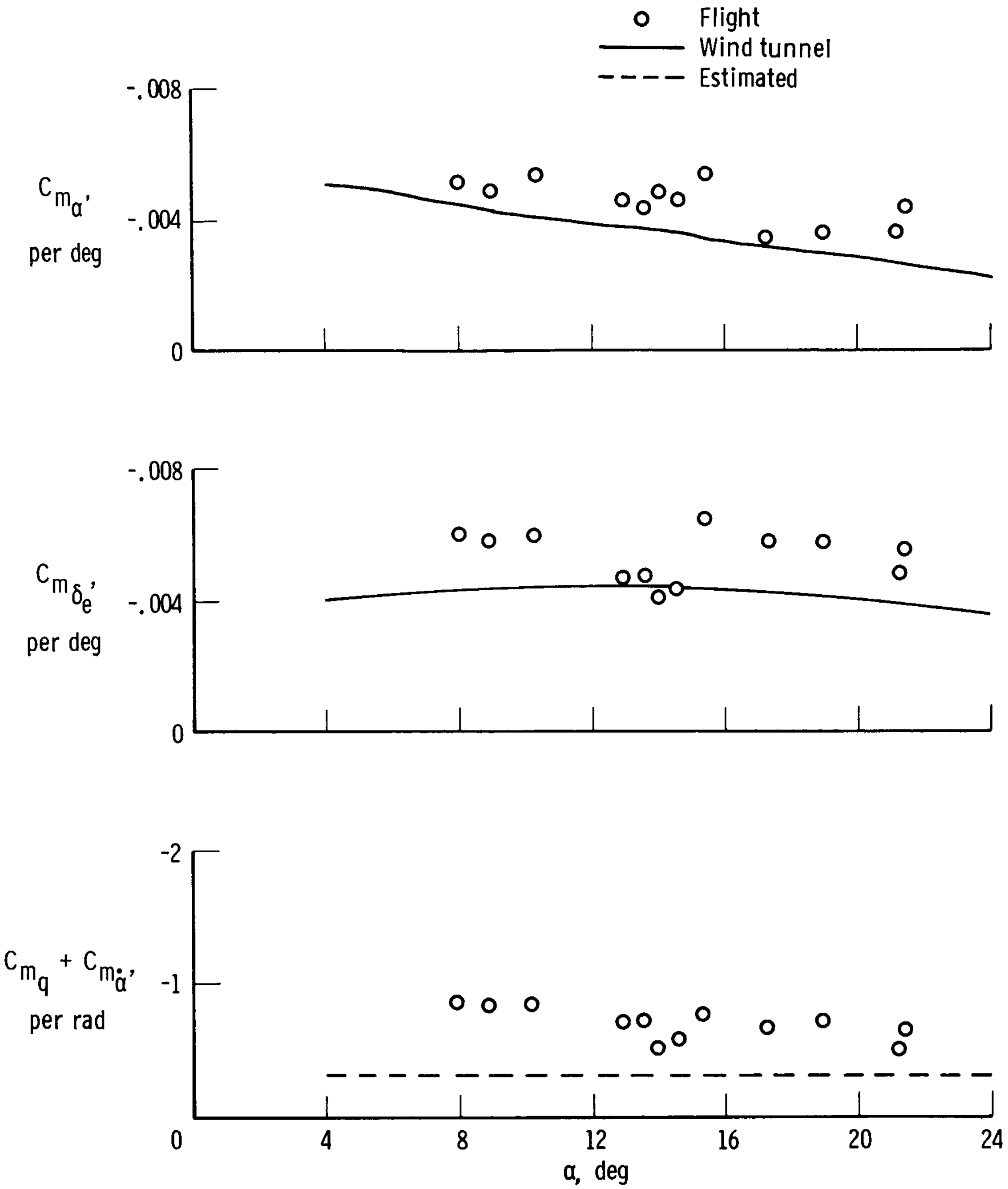

(b) M = 0.7, transonic configuration.

Figure 7. Continued.

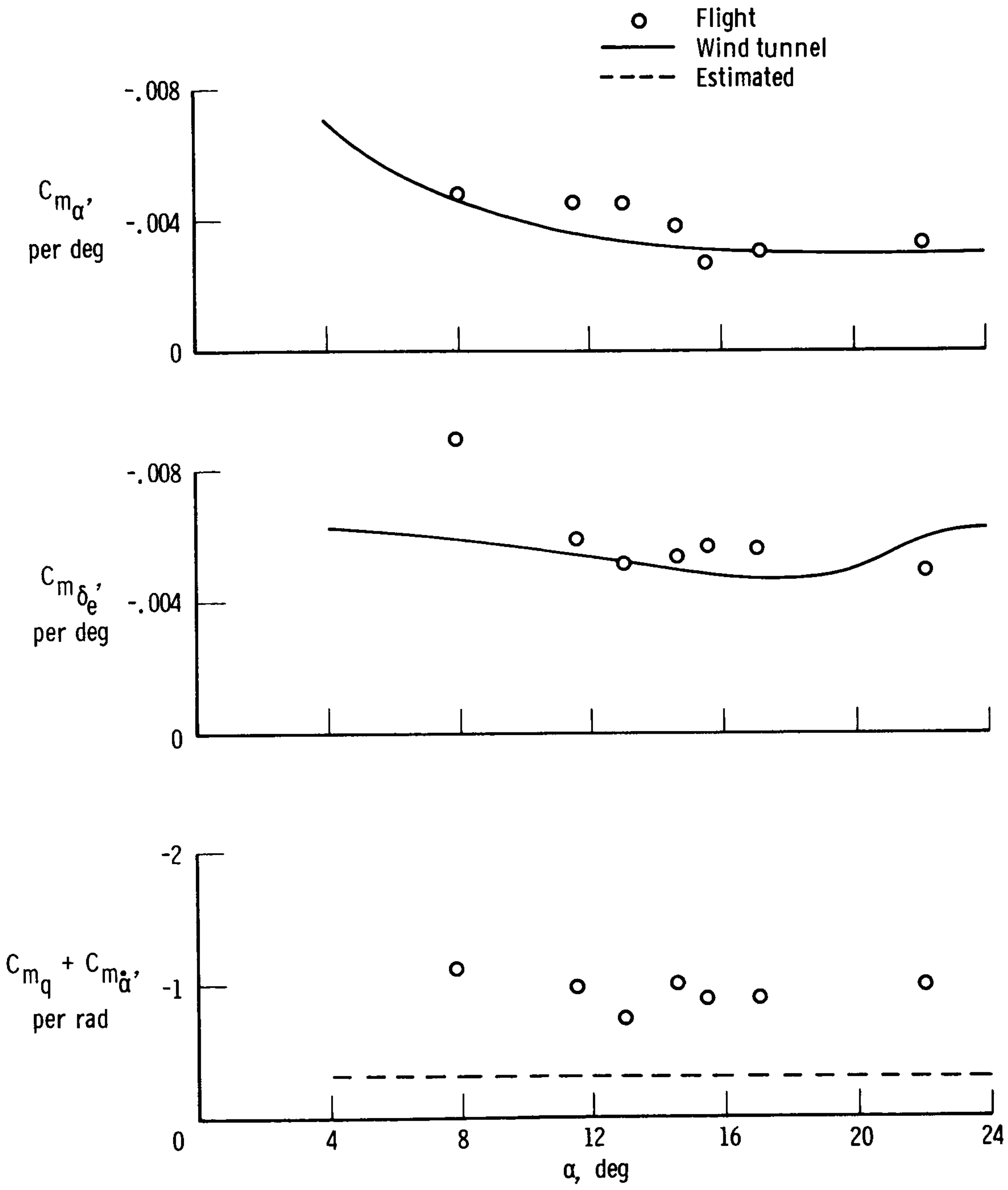

(c) M = 0.9, transonic configuration.

Figure 7. Continued.

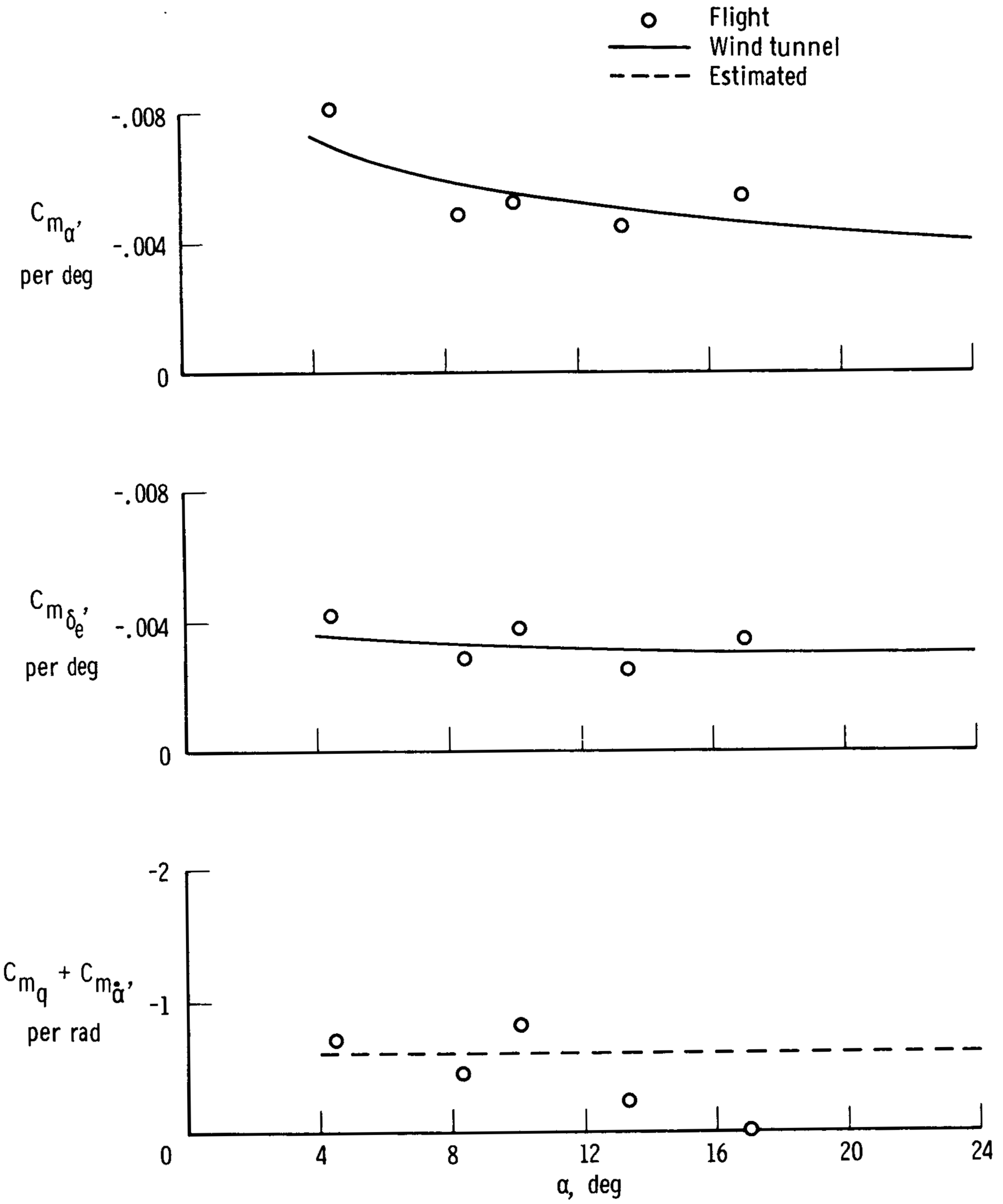

(d) M = 1.2, transonic configuration.

Figure 7. Concluded.

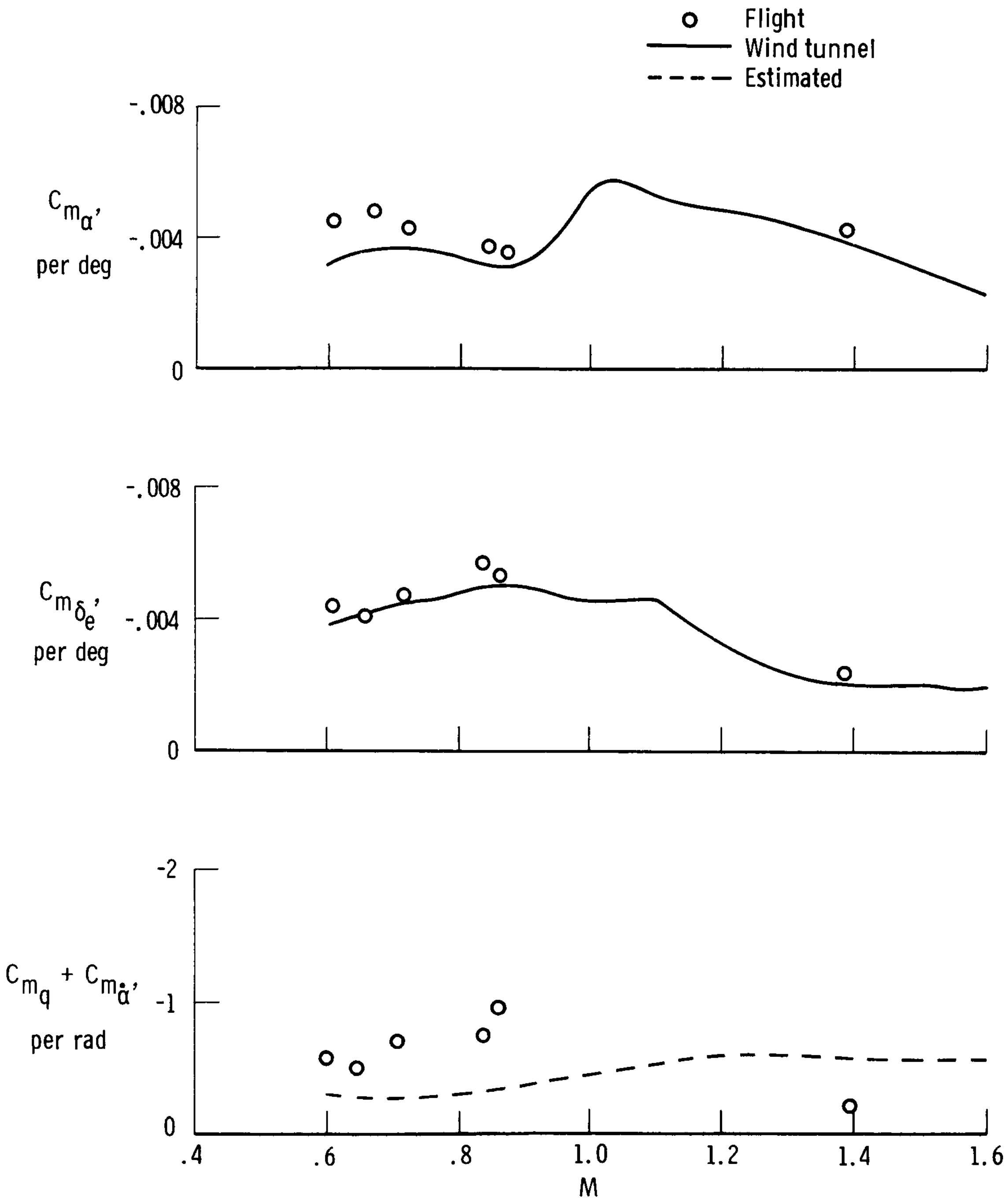

Figure 8. Comparison of flight and wind-tunnel pitching-moment derivatives as a function of Mach number for an angle of attack of 14°. Transonic configuration.

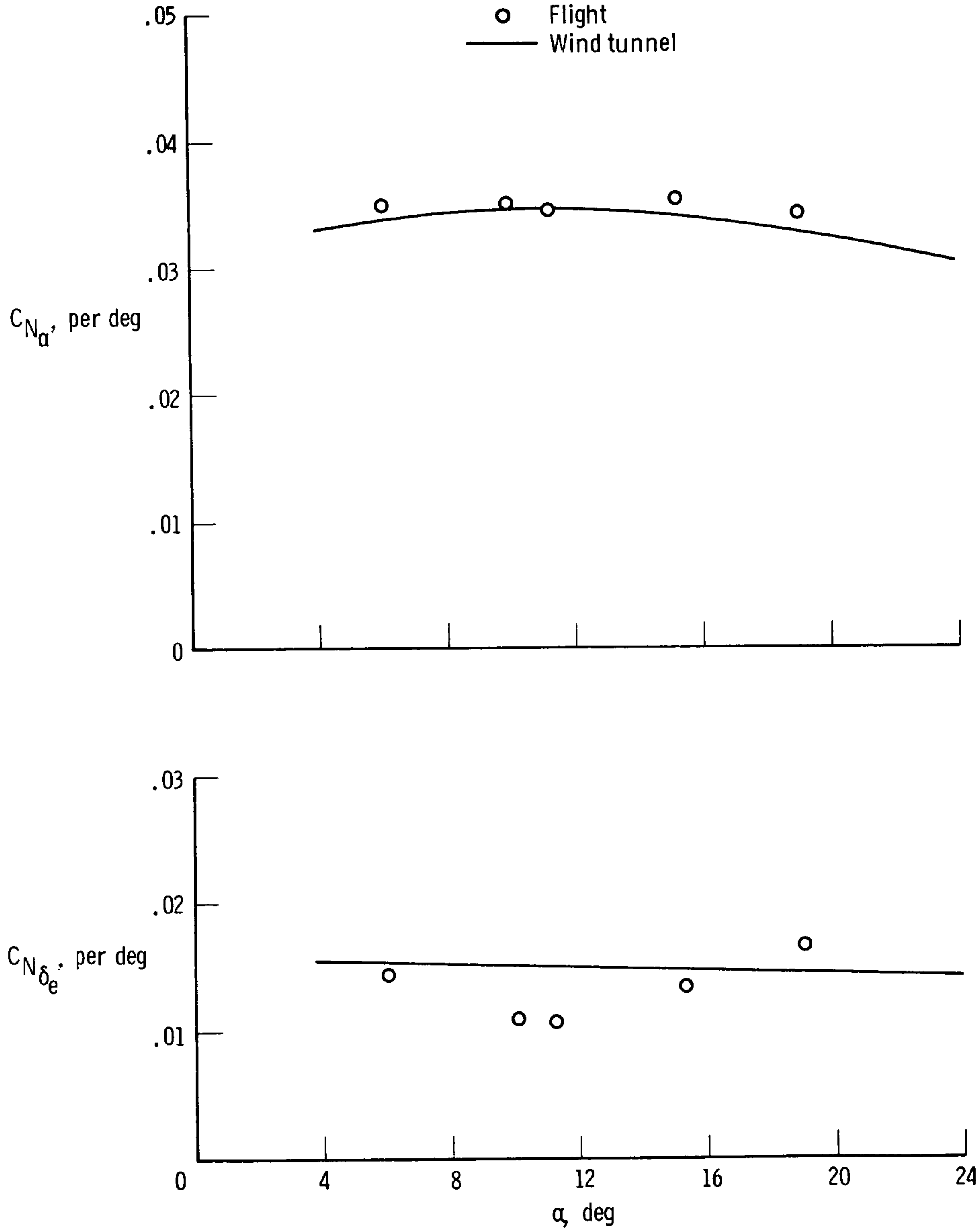

(a) M = 0.7, subsonic configuration.

Figure 9. Comparison of flight and wind-tunnel normal-force derivatives as a function of angle of attack.

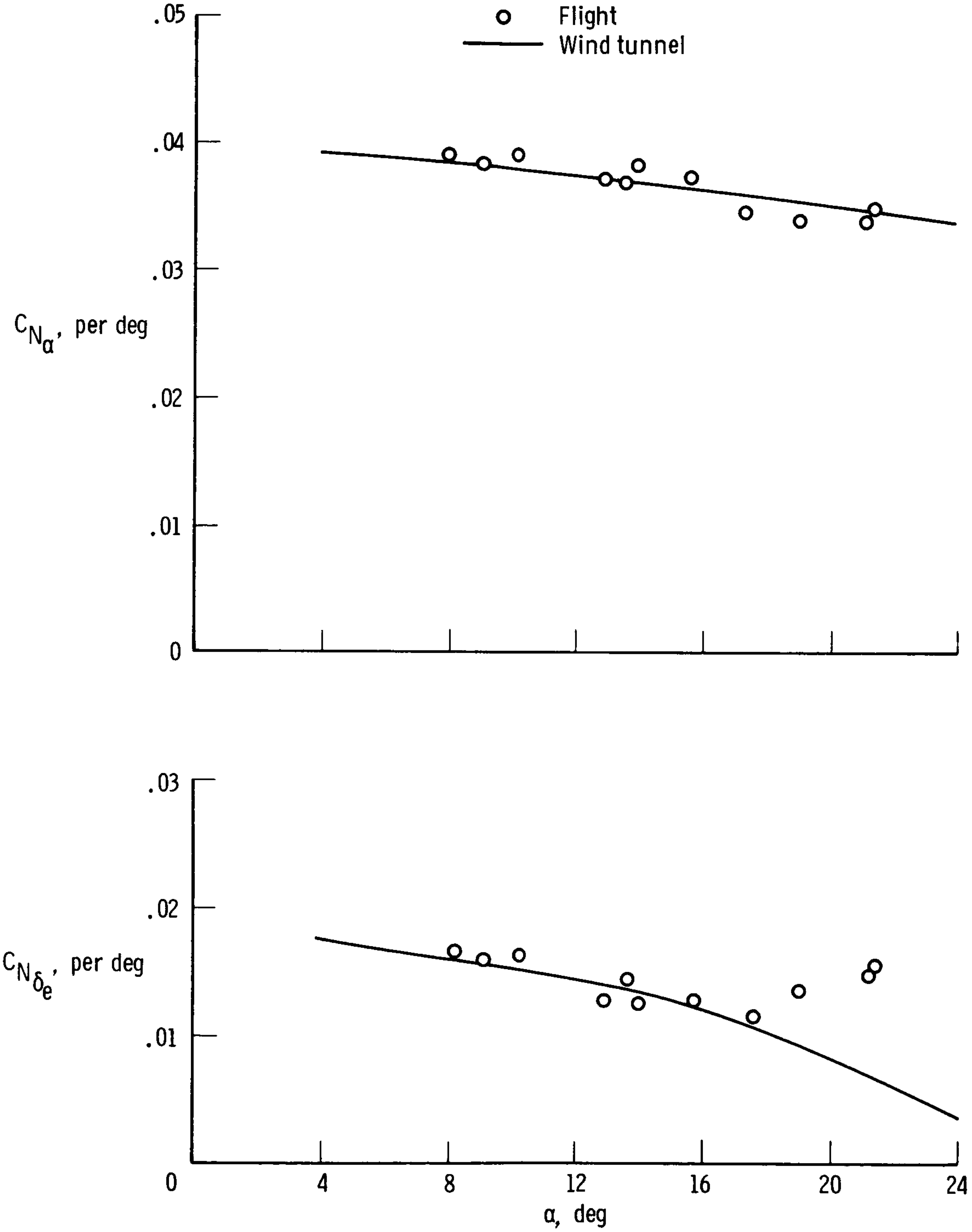

(b) M = 0.7, transonic configuration.

Figure 9. Continued.

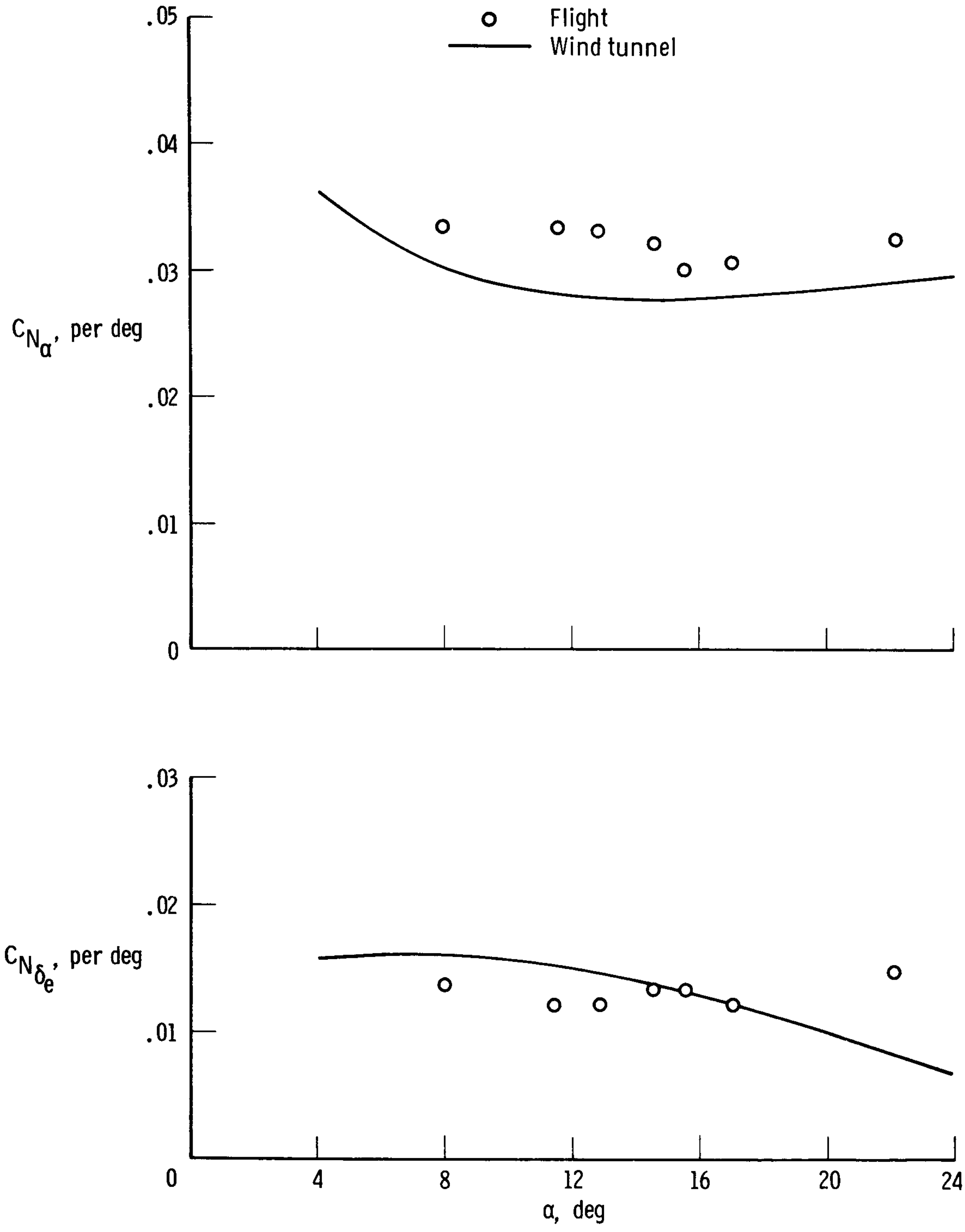

(c) M = 0.9, transonic configuration.

Figure 9. Continued.

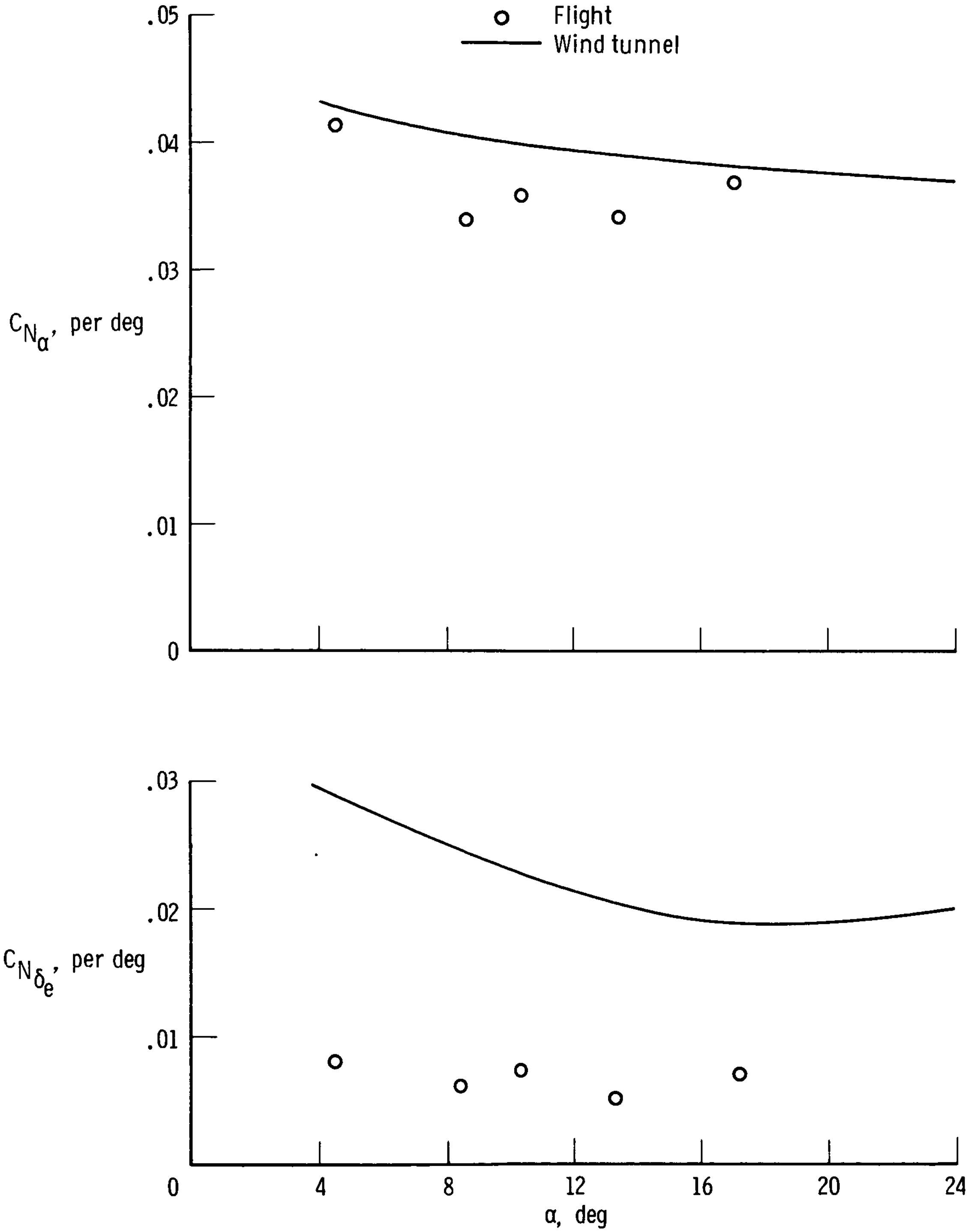

(d) M = 1.2, transonic configuration.

Figure 9. Concluded.

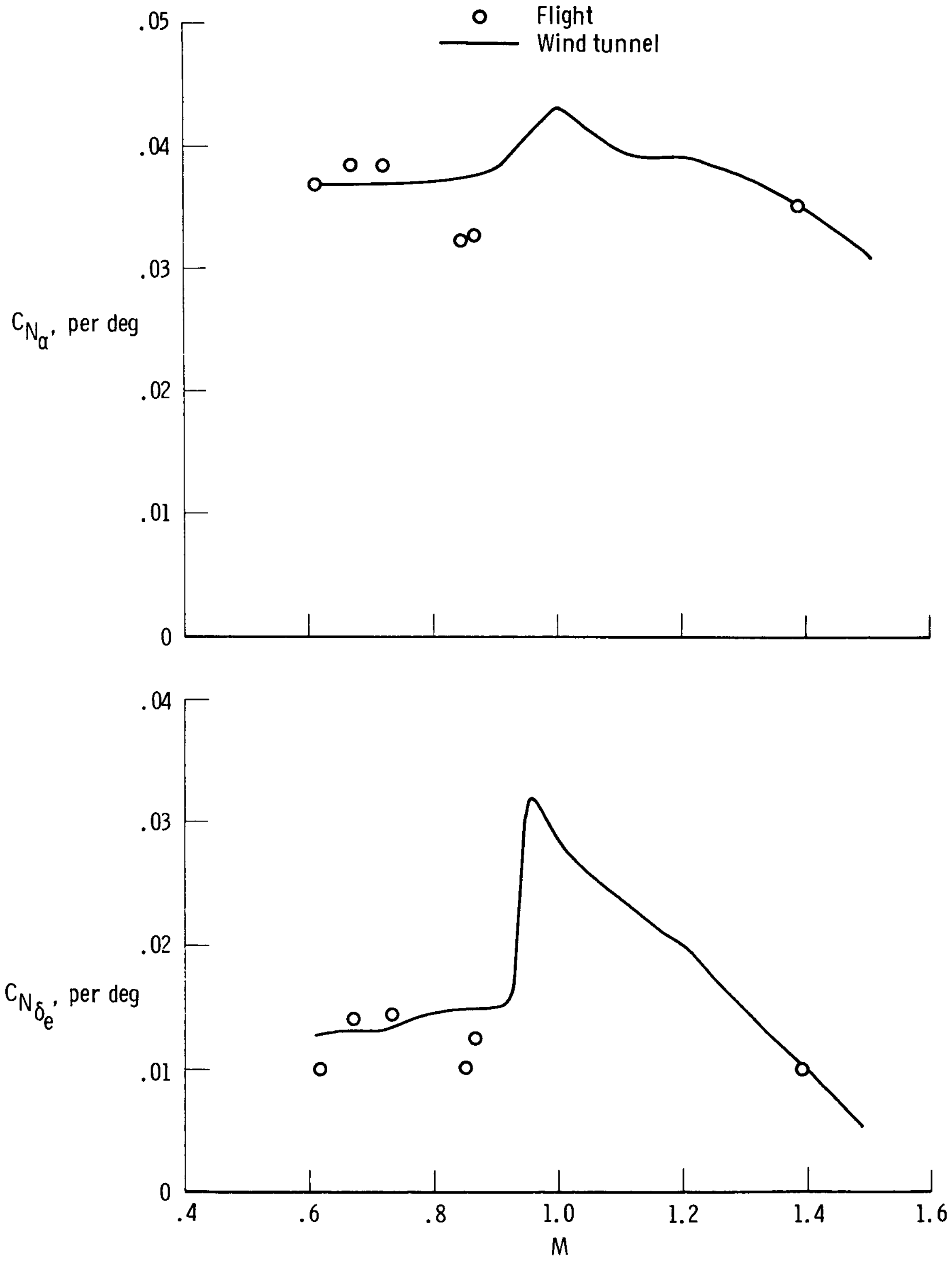

Figure 10. Comparison of flight and wind-tunnel normal-force derivatives as a function of Mach number for an angle of attack of 14°. Transonic configuration.

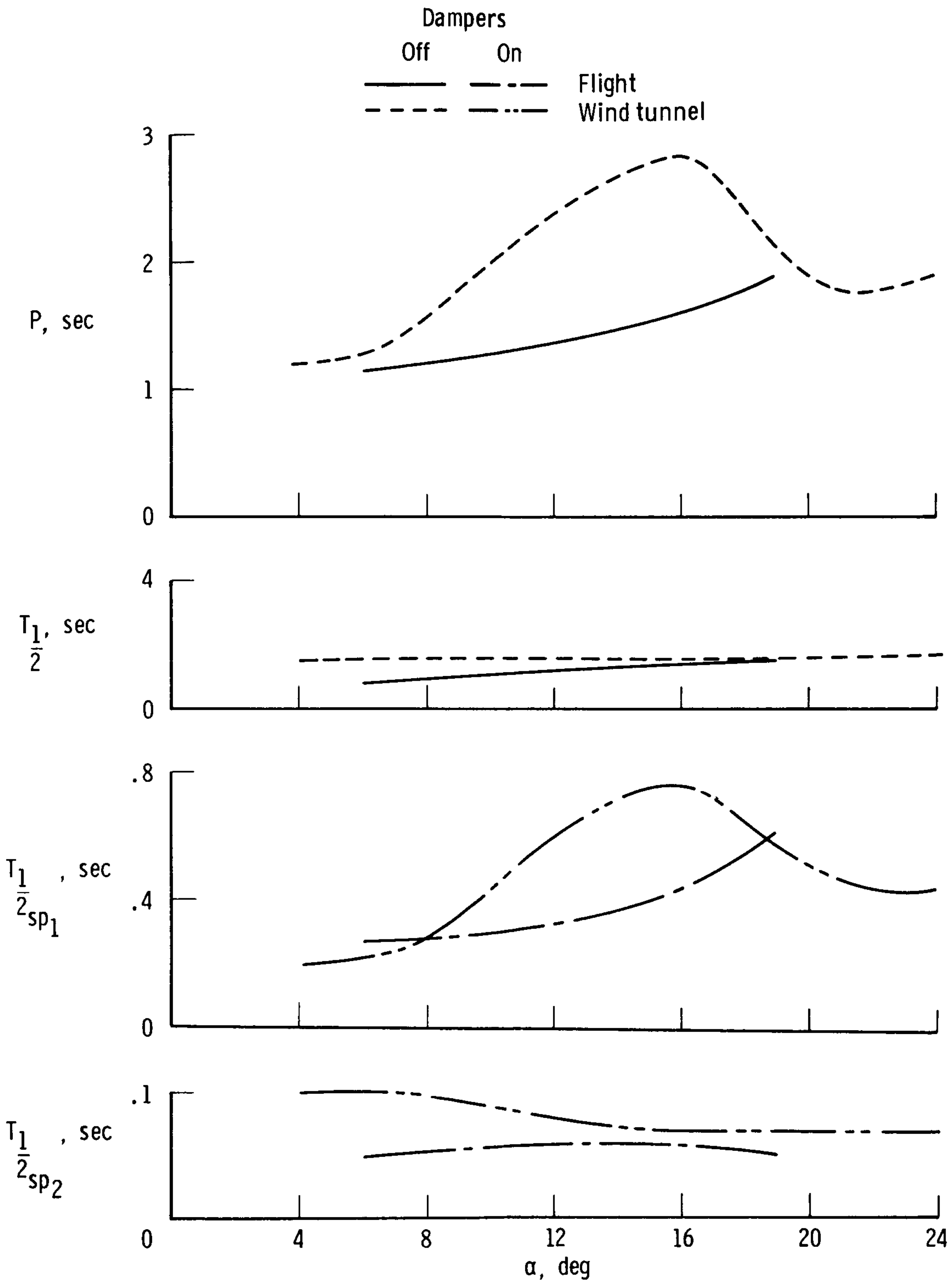

(a) M = 0.7, subsonic configuration.

Figure 11. Comparison of flight and wind-tunnel longitudinal period and time to damp to one-half amplitude as a function of angle of attack.

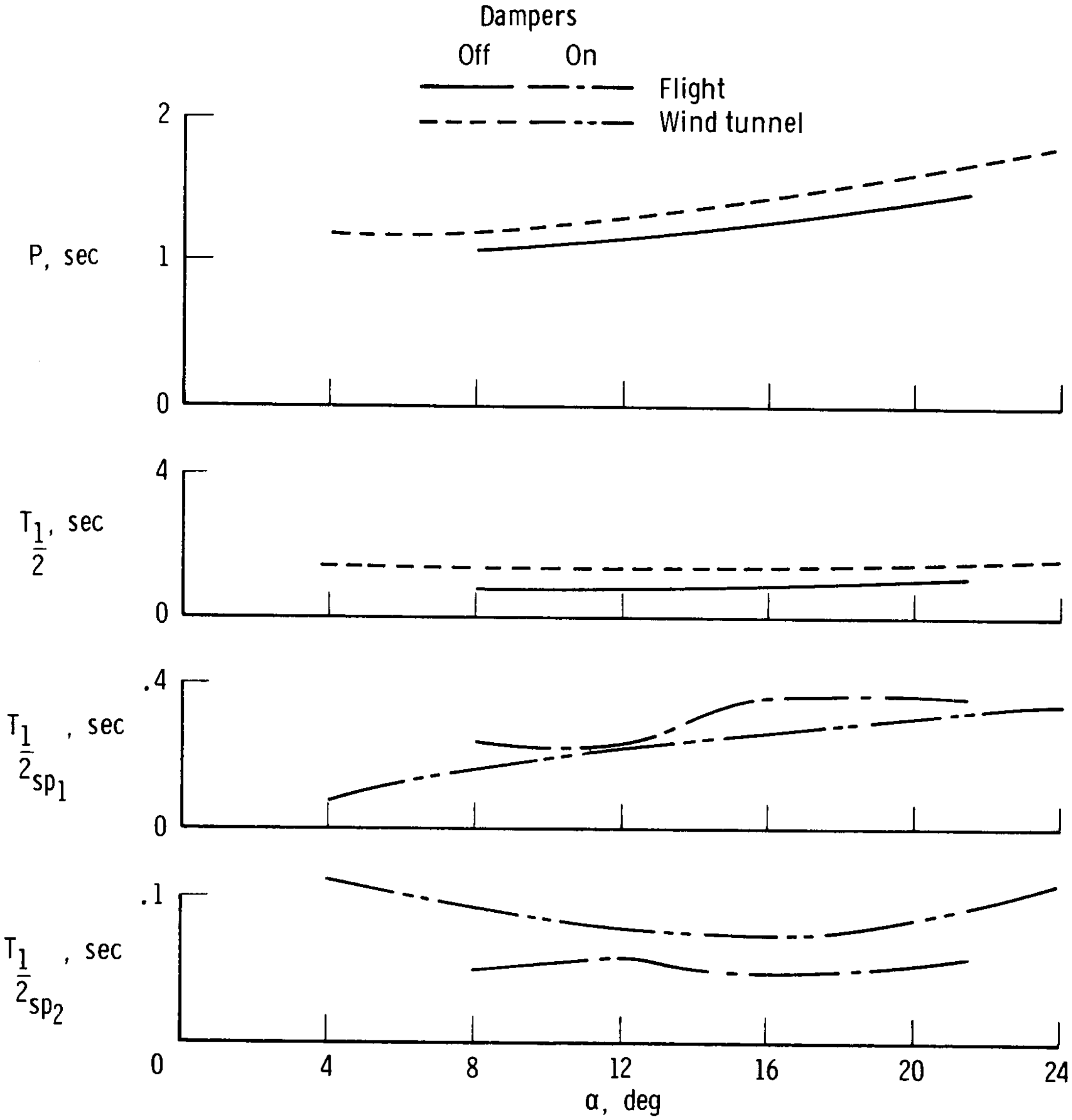

(b) M = 0.7, transonic configuration.

Figure 11. Continued.

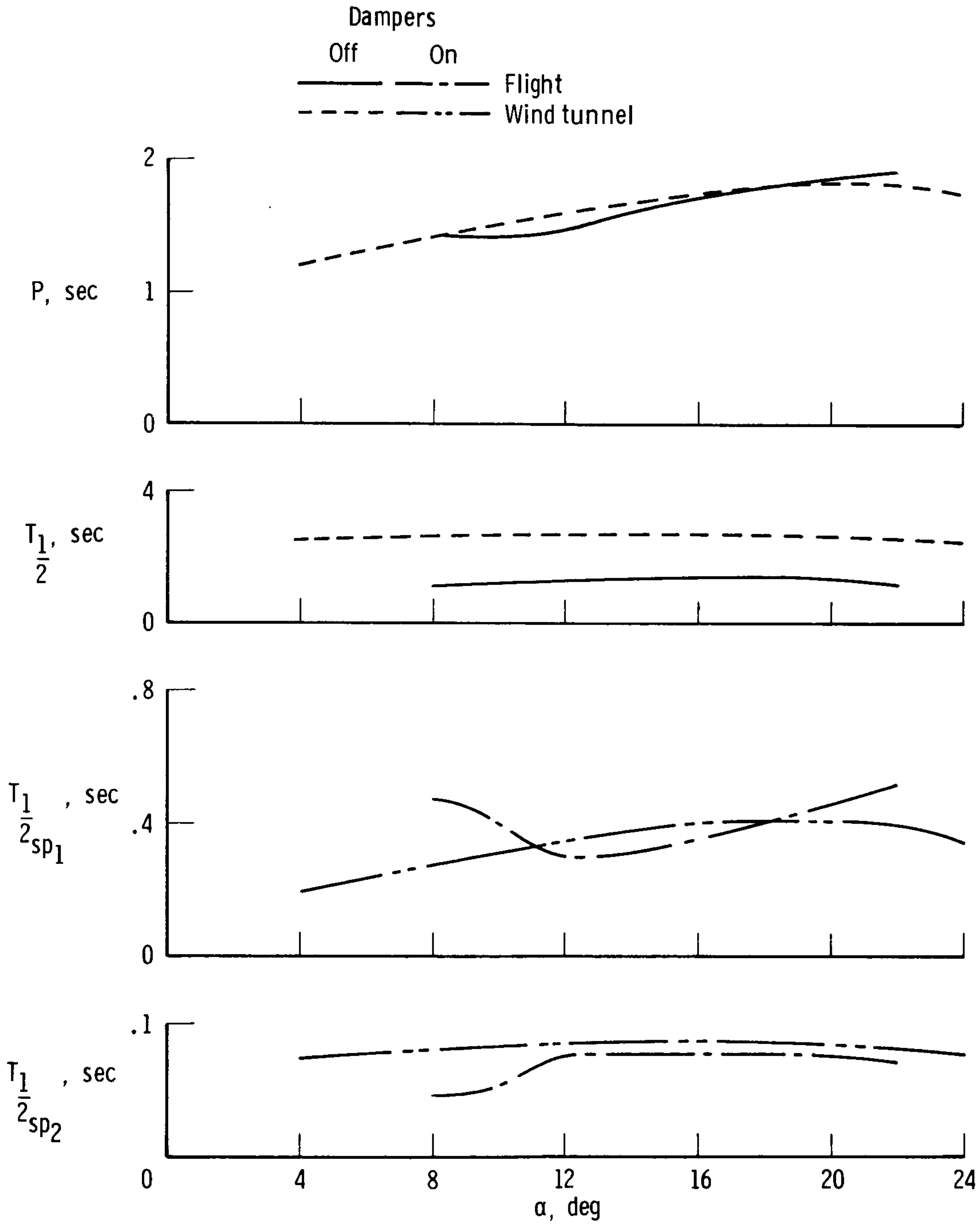

(c) M = 0.9, transonic configuration.

Figure 11. Continued.

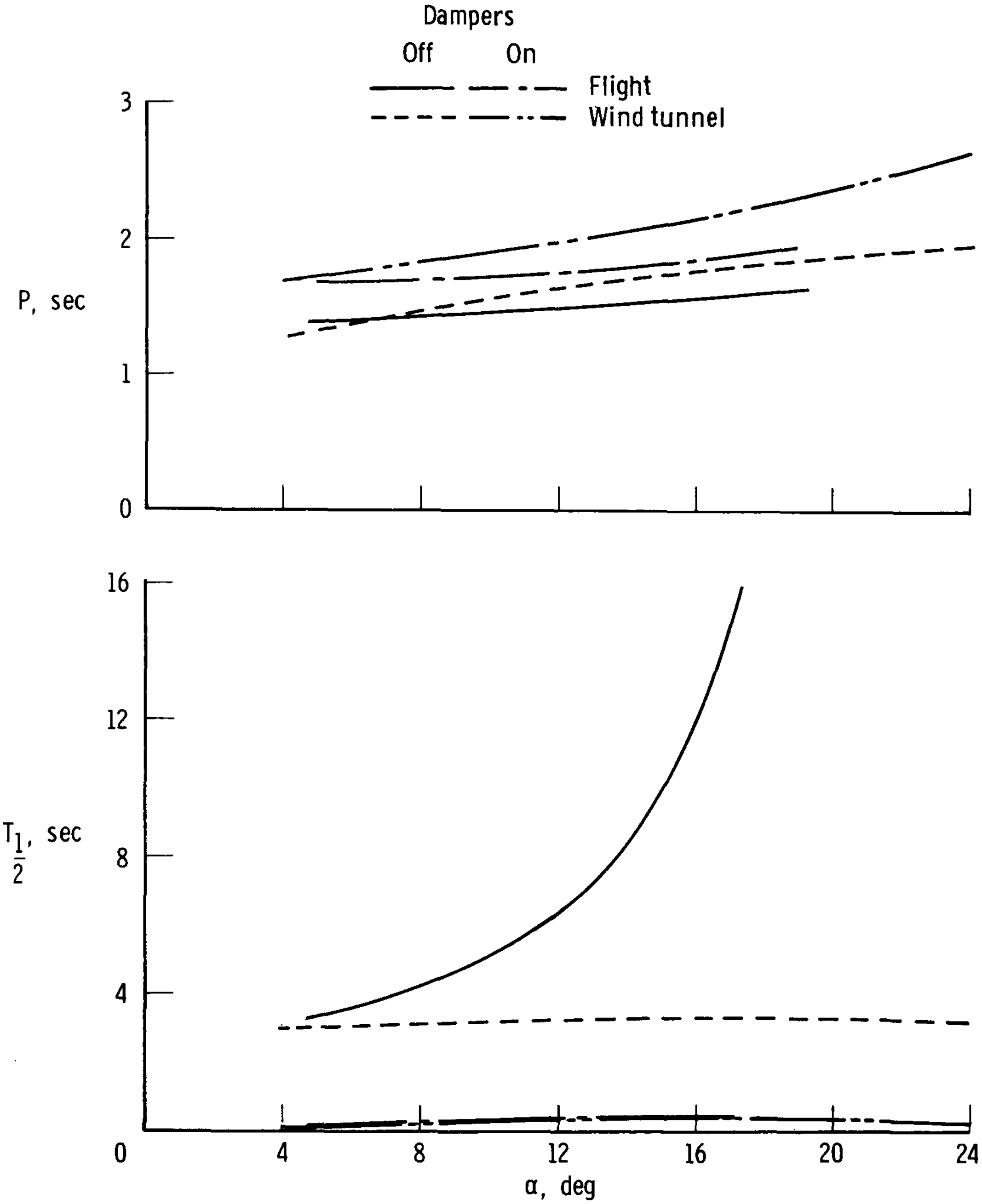

(d) M = 1.2, transonic configuration.

Figure 11. Concluded.

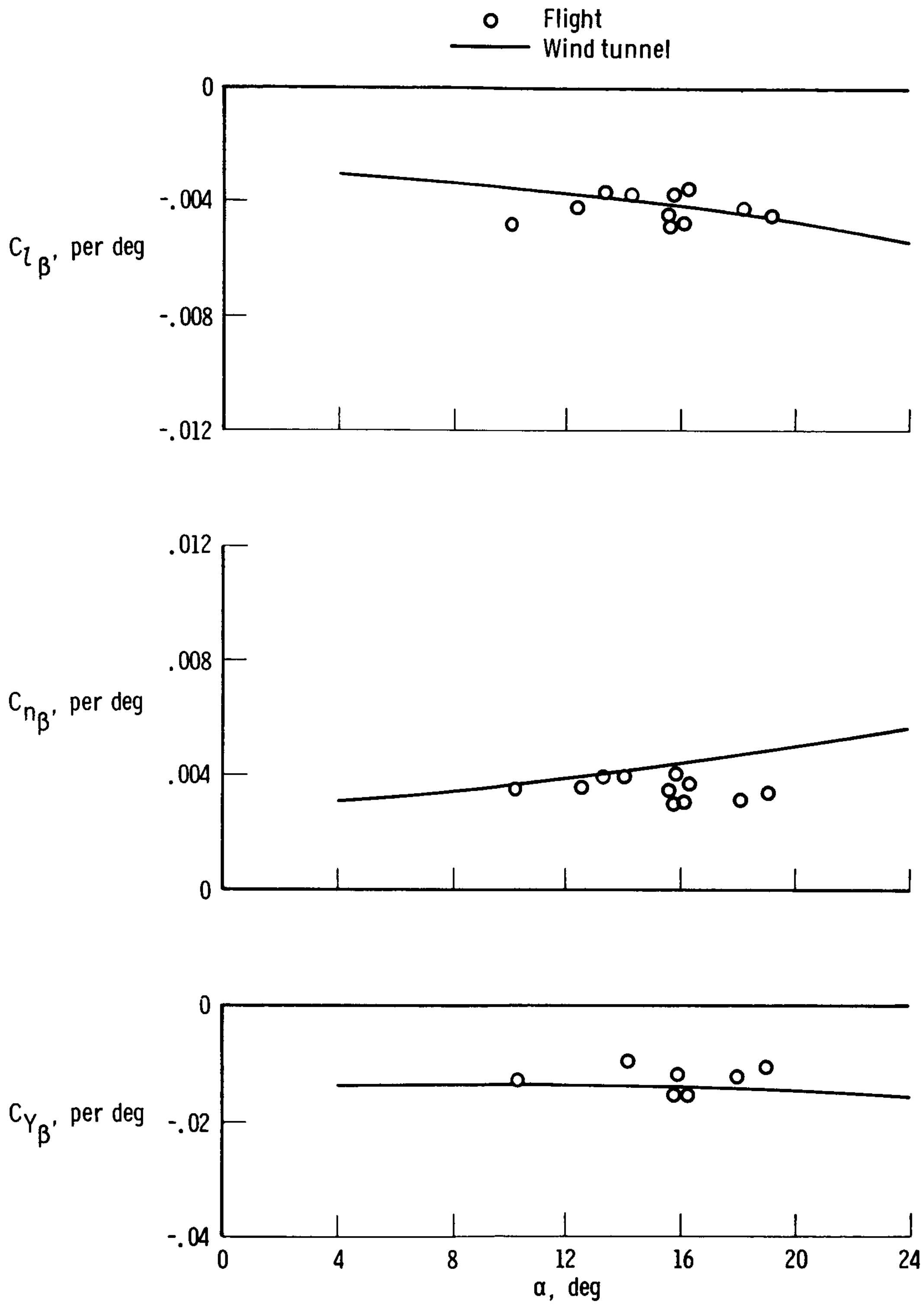

(a) M = 0.7, subsonic configuration.

Figure 12. Comparison of flight and wind-tunnel sideslip derivatives as a function of angle of attack.

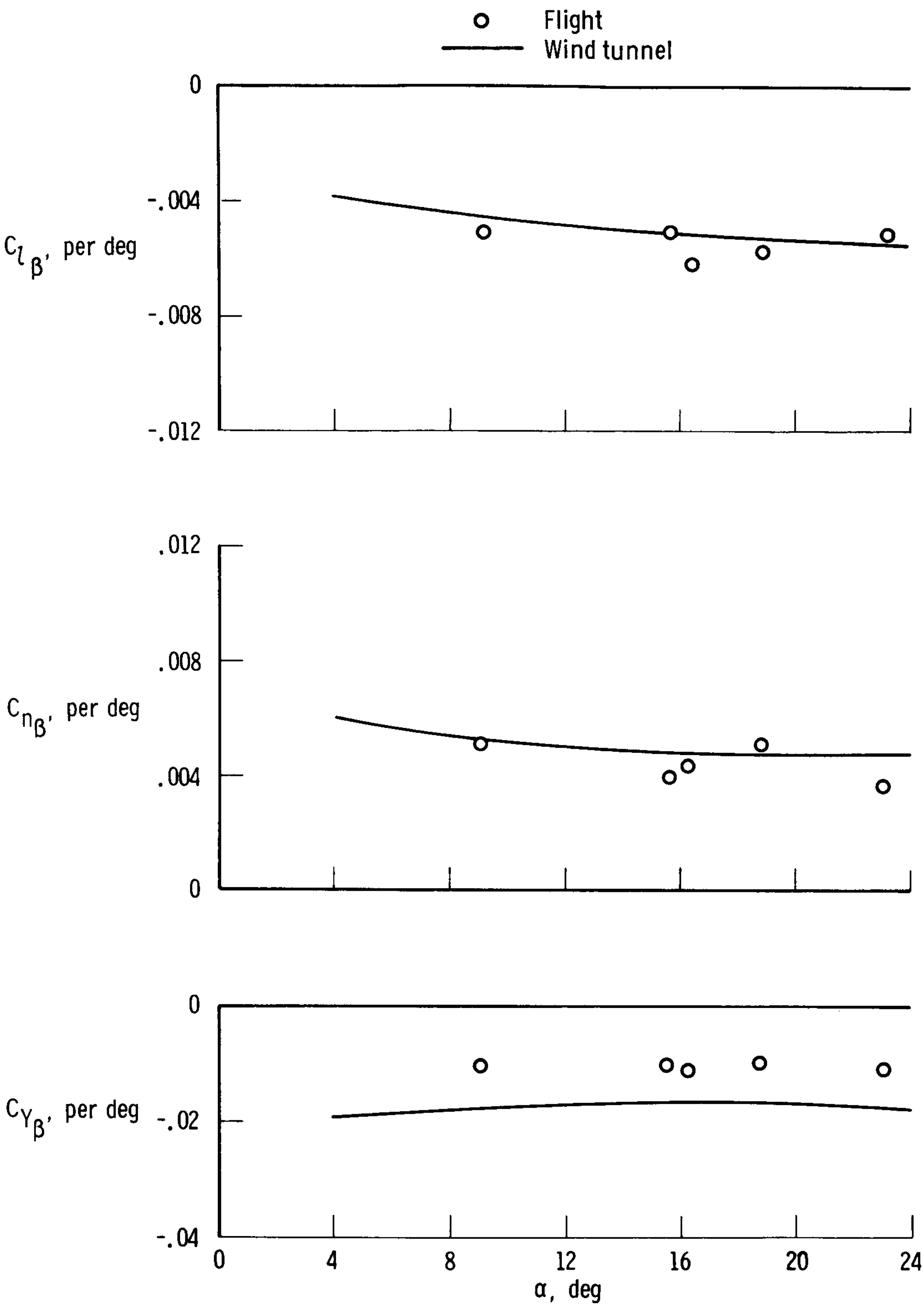

(b) M = 0.7, transonic configuration.

Figure 12. Continued.

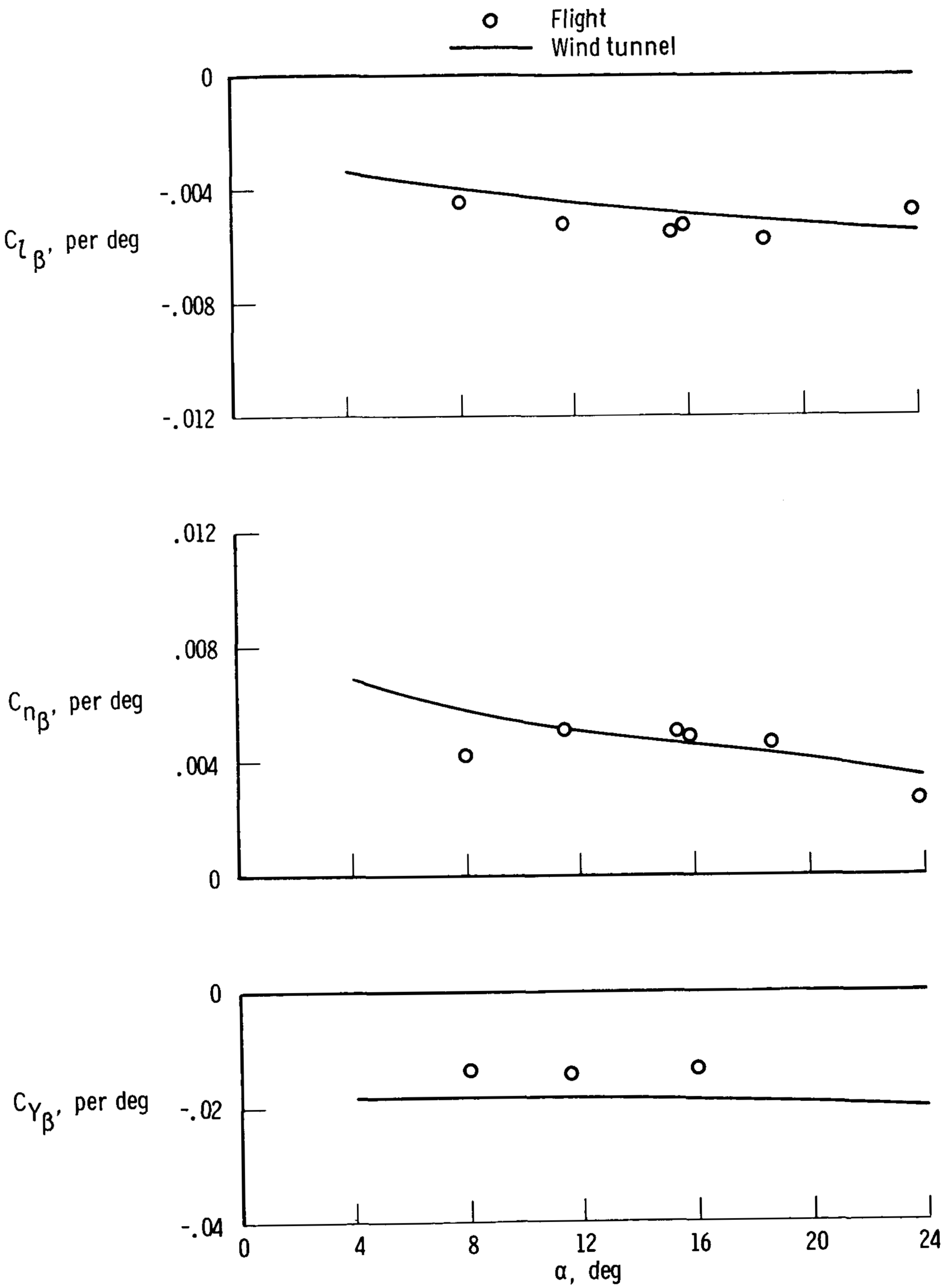

(c) M = 0.9, transonic configuration.

Figure 12. Continued.

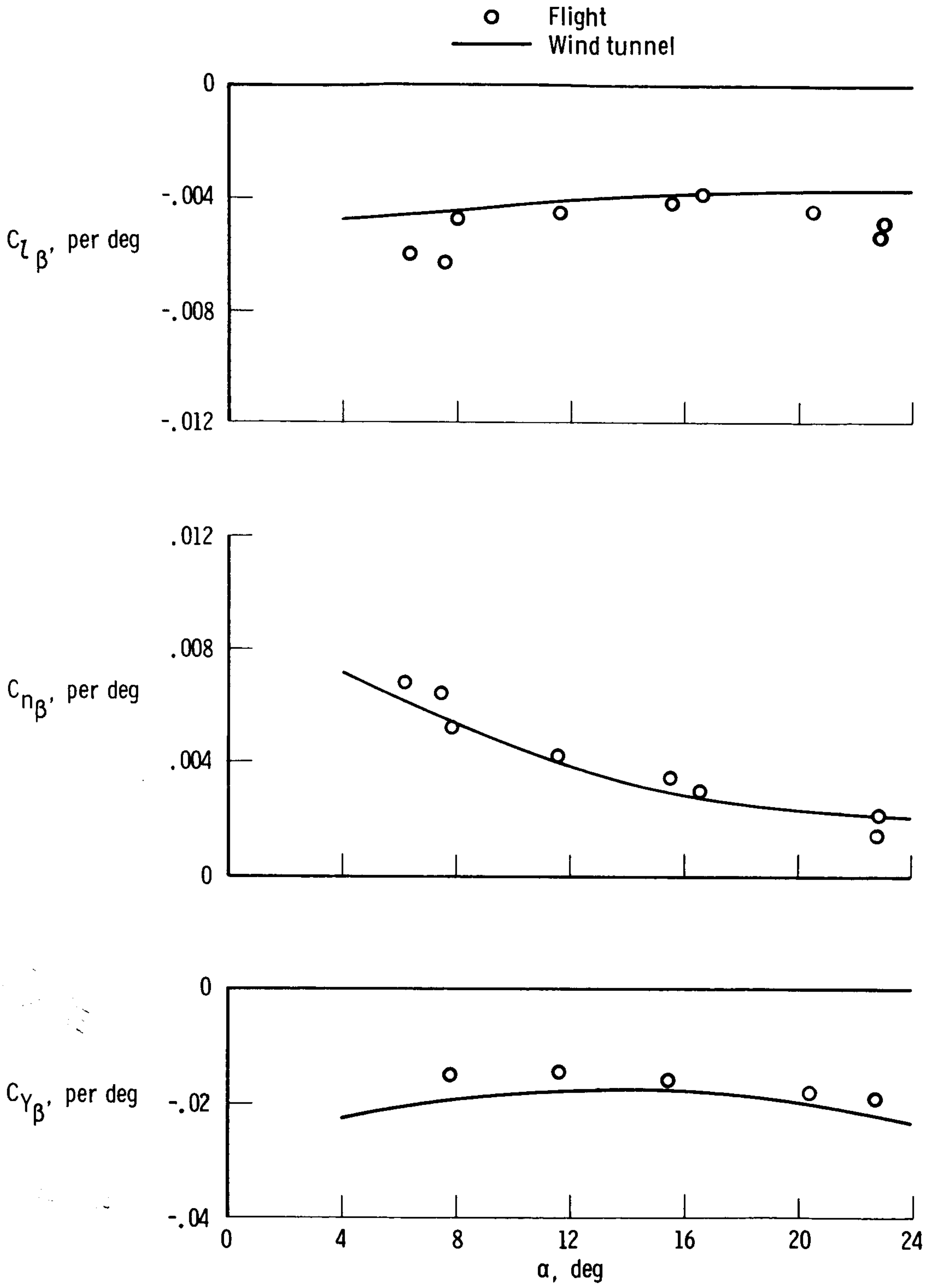

(d) M = 1.2, transonic configuration.

Figure 12. Concluded.

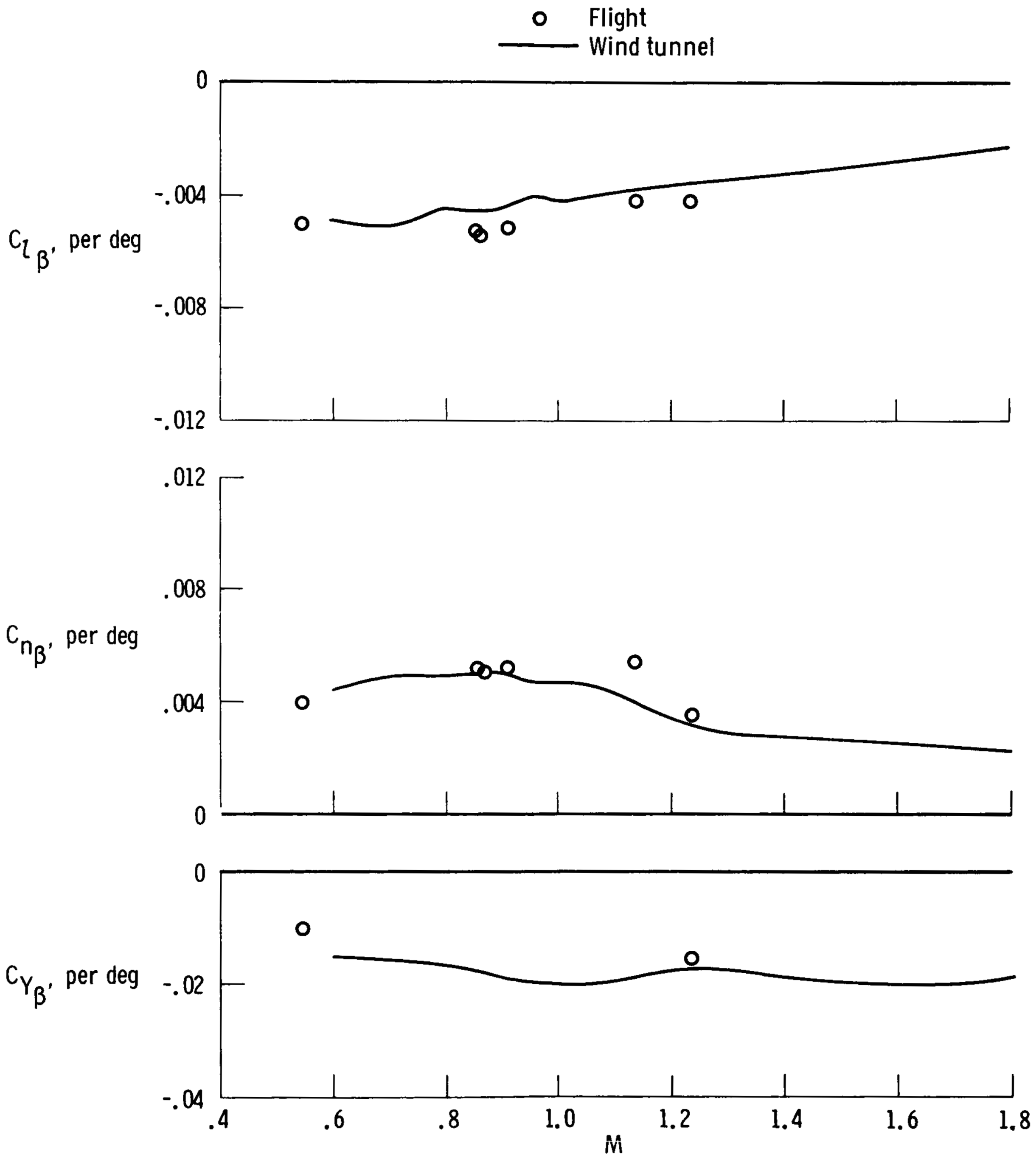

Figure 13. Comparison of flight and wind-tunnel sideslip derivatives as a function of Mach number for an angle of attack of 14°. Transonic configuration.

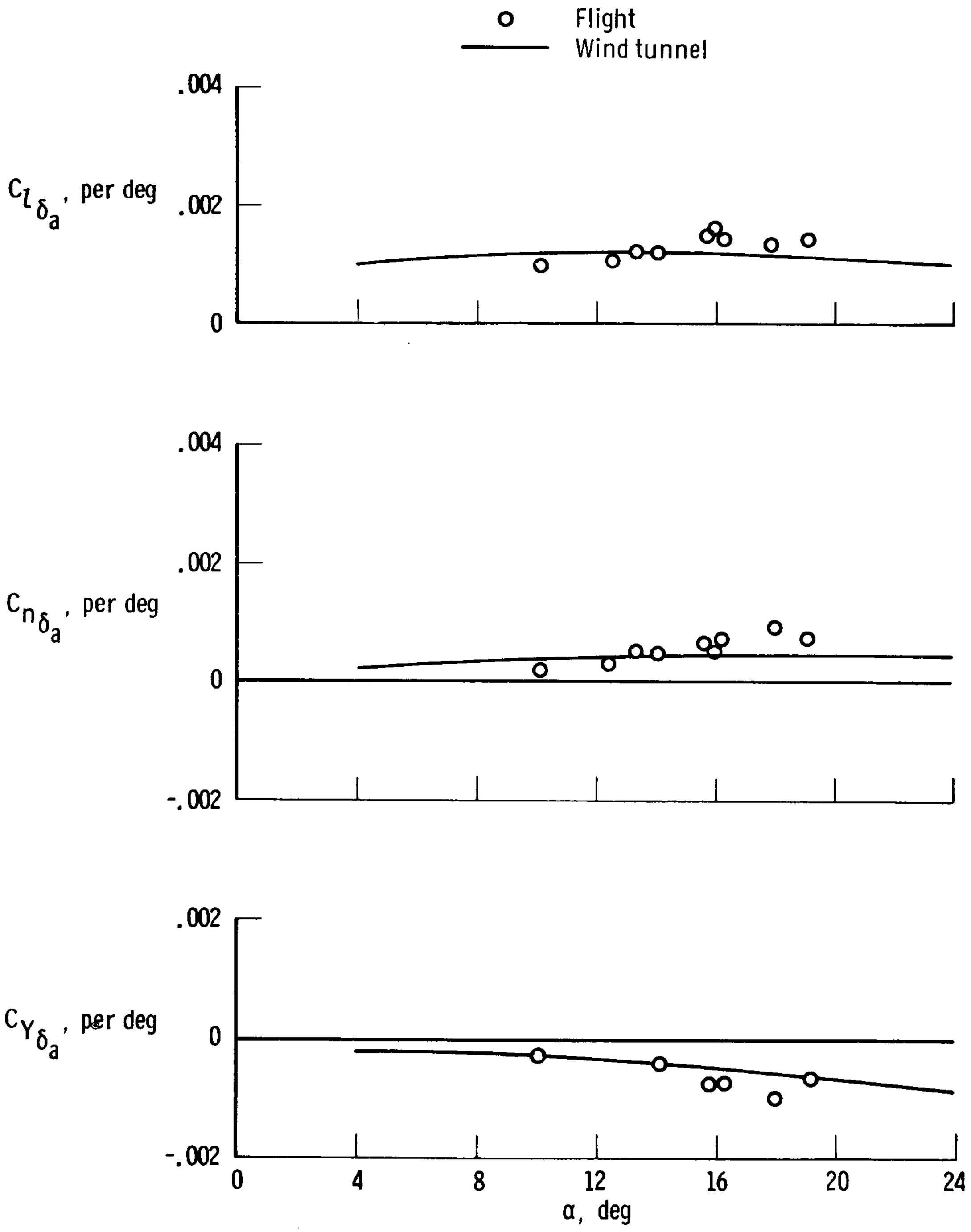

(a) M = 0.7, subsonic configuration.

Figure 14. Comparison of flight and wind-tunnel aileron derivatives as a function of angle of attack.

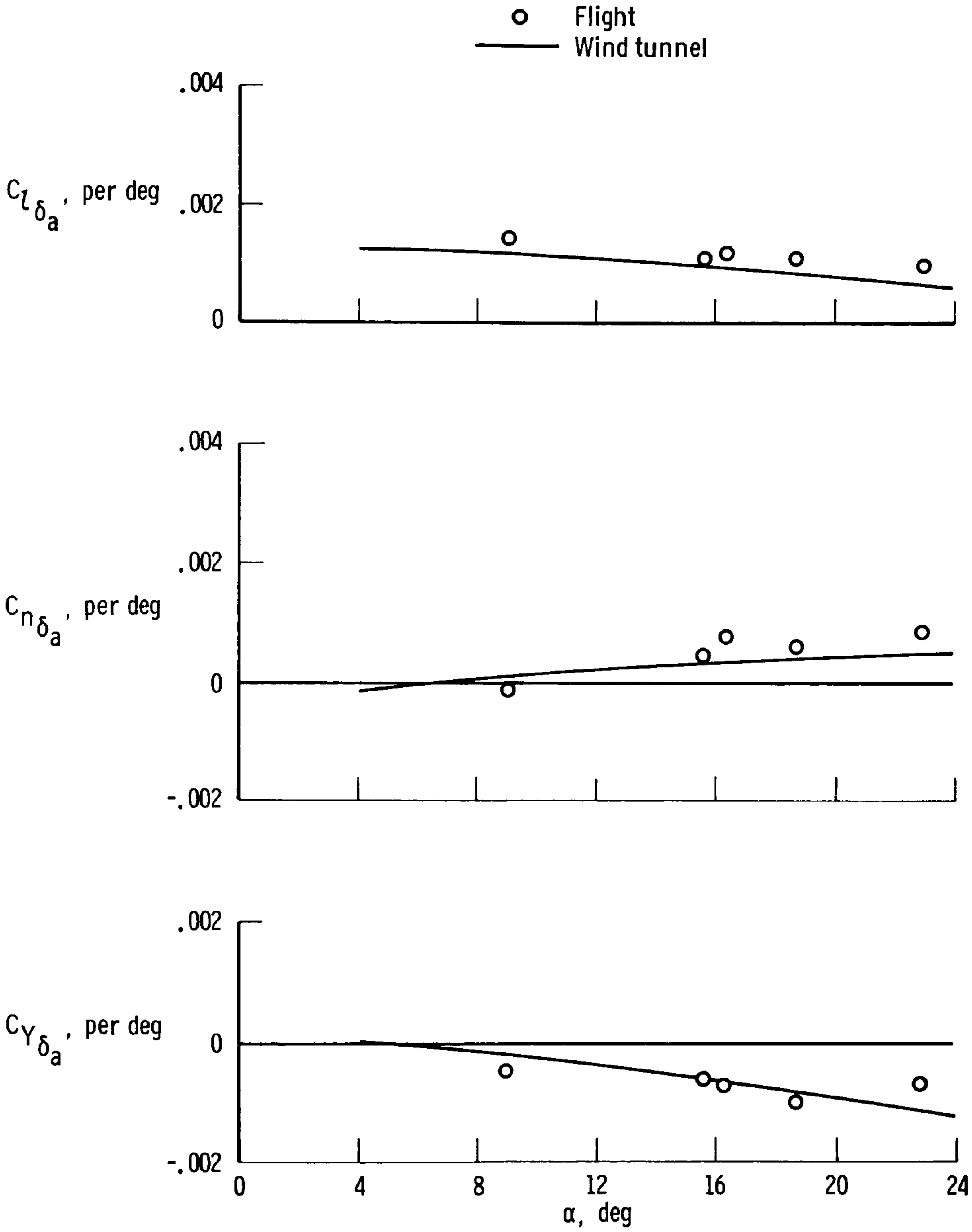

(b) M = 0.7, transonic configuration.

Figure 14. Continued.

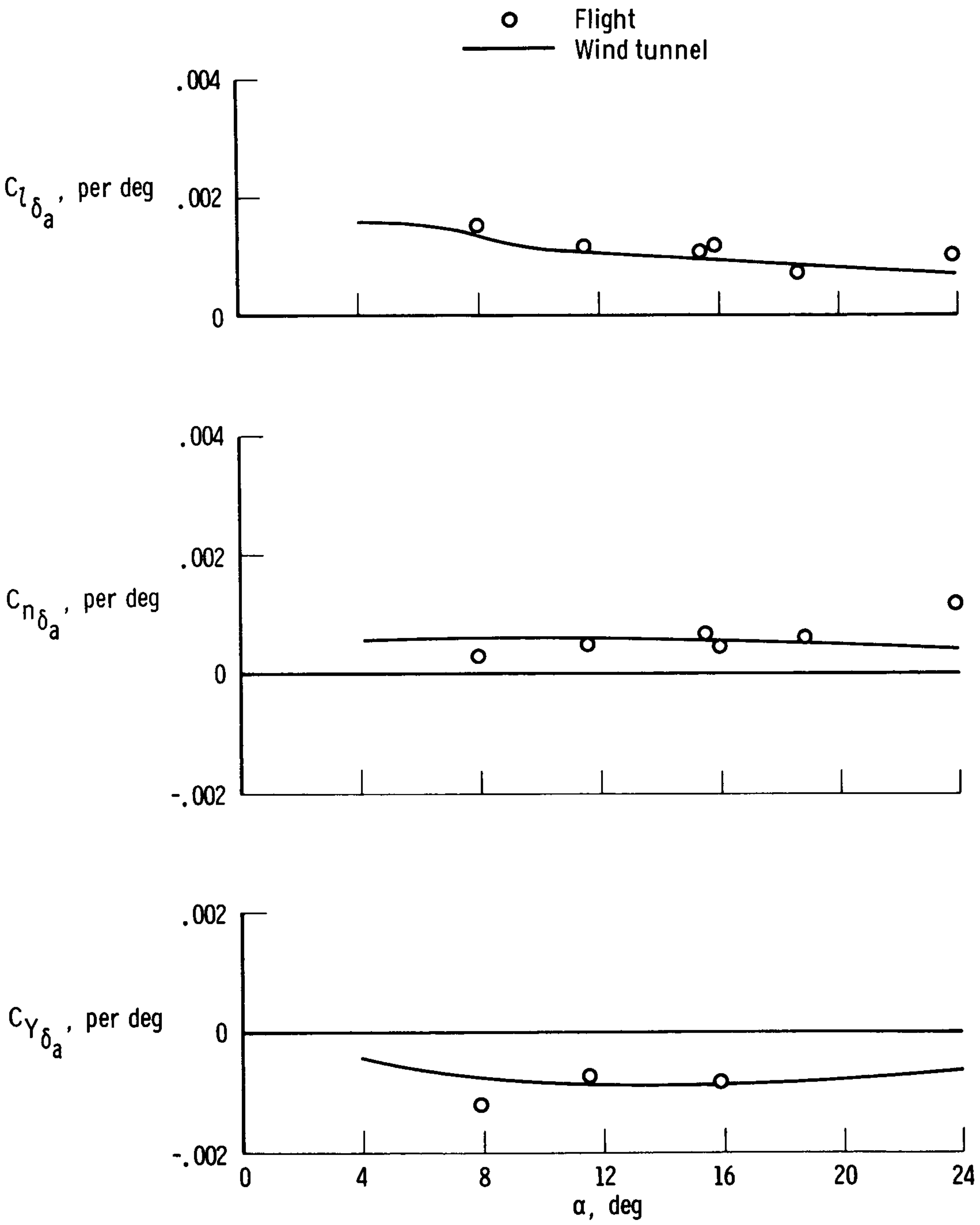

(c) M = 0.9, transonic configuration.

Figure 14. Continued.

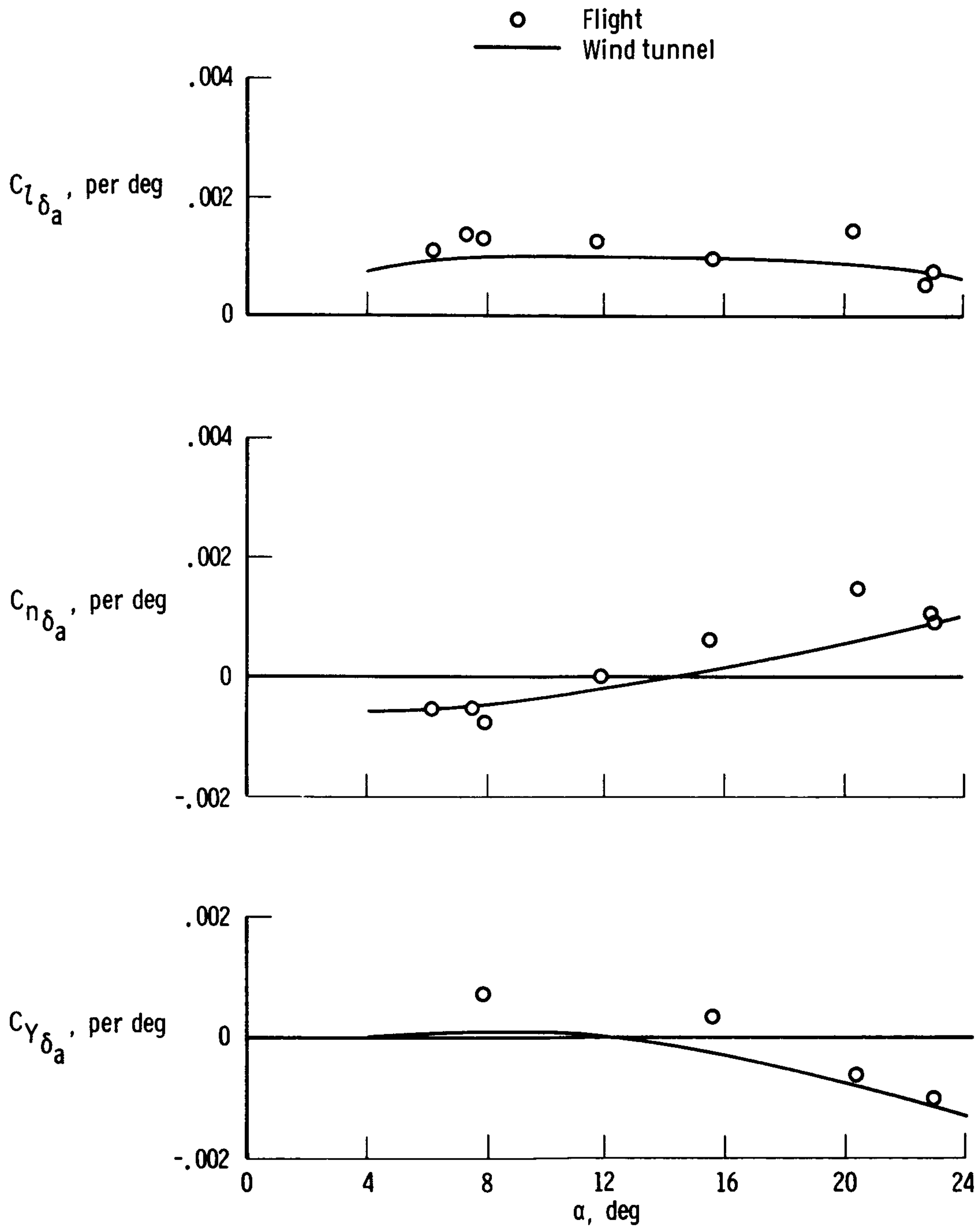

(d) M = 1.2, transonic configuration.

Figure 14. Concluded.

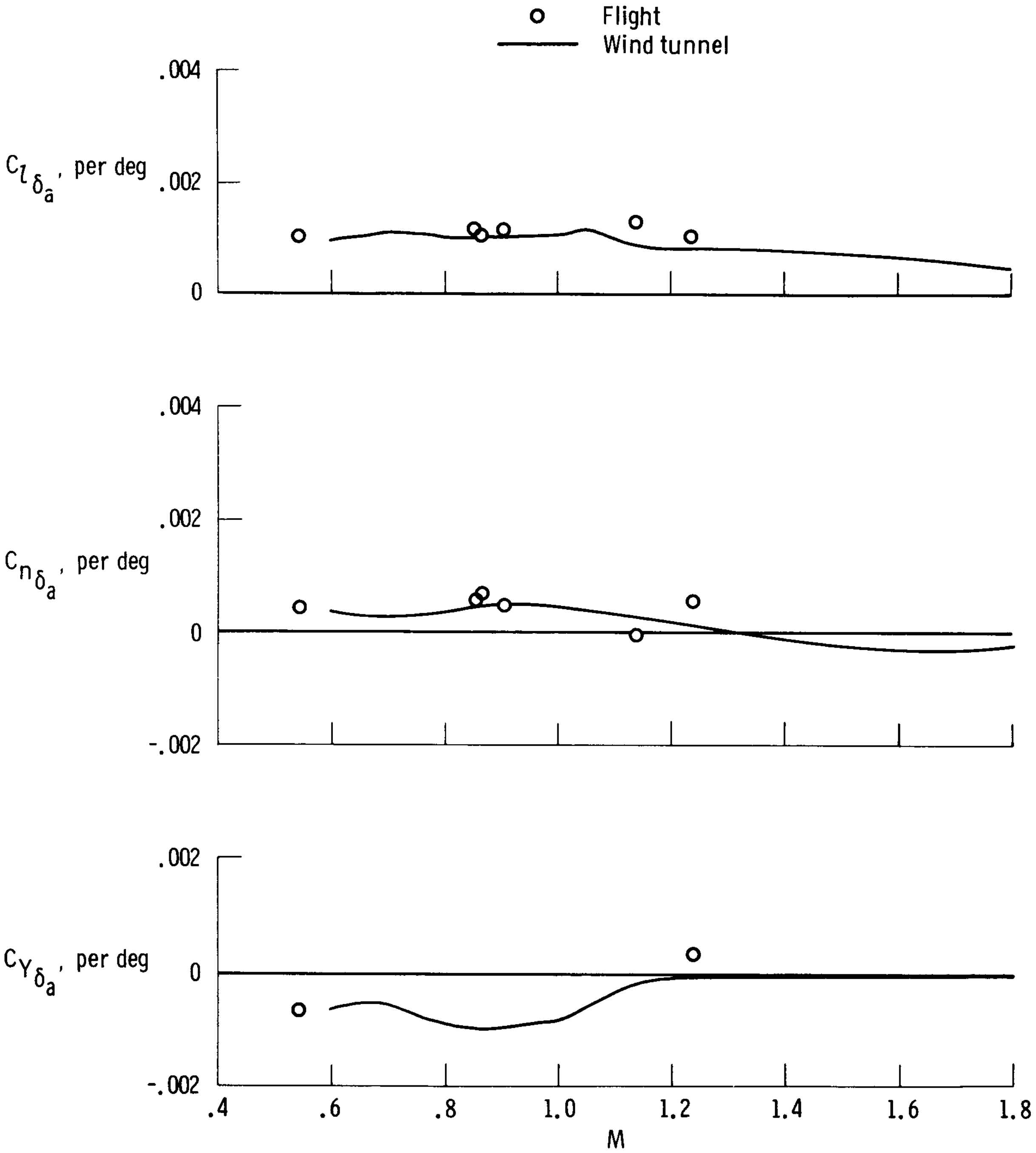

Figure 15. Comparison of flight and wind-tunnel aileron derivatives as a function of Mach number for an angle of attack of 14°. Transonic configuration.

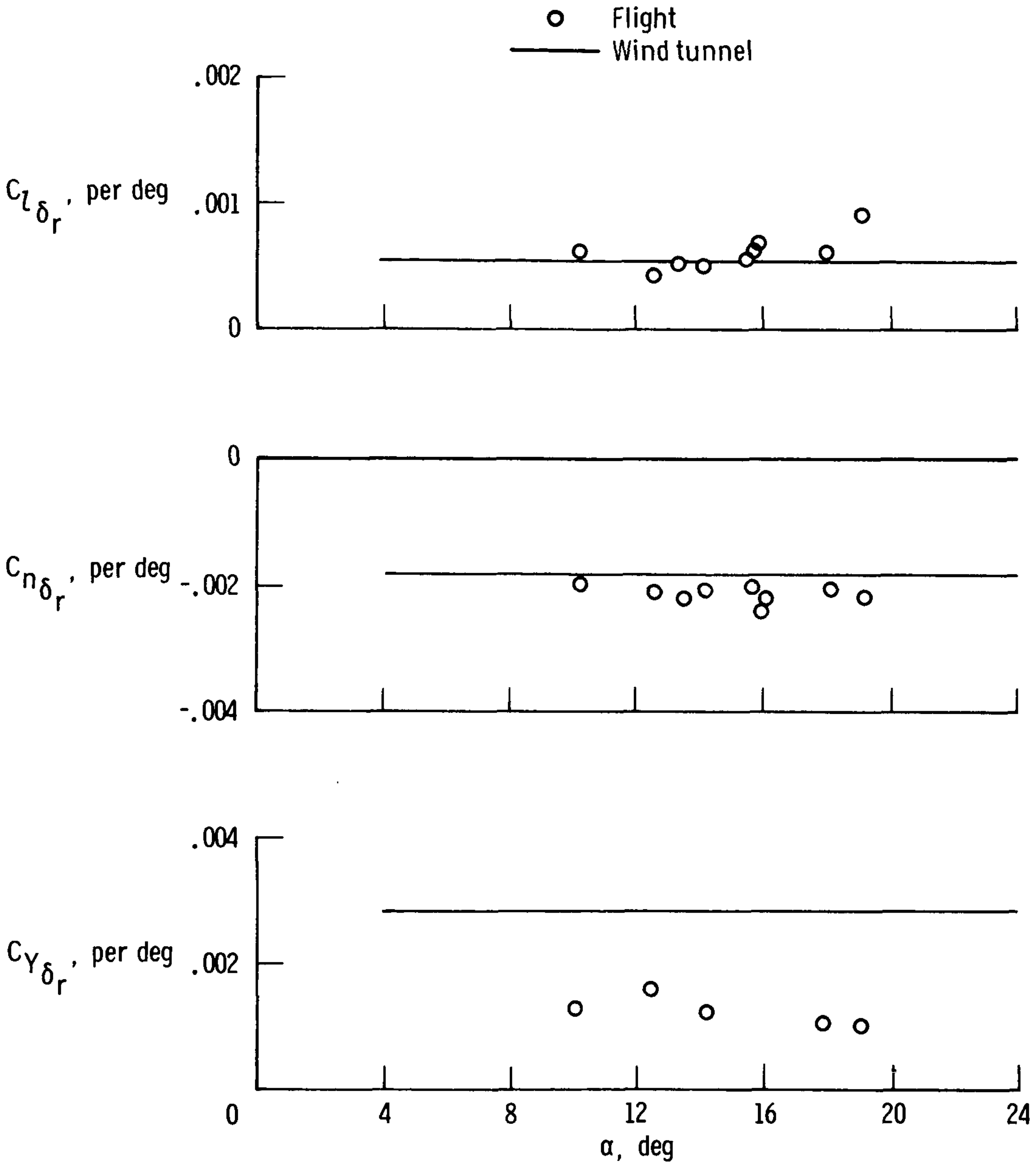

(a) M = 0.7, subsonic configuration.

Figure 16. Comparison of flight and wind-tunnel rudder derivatives as a function of angle of attack.

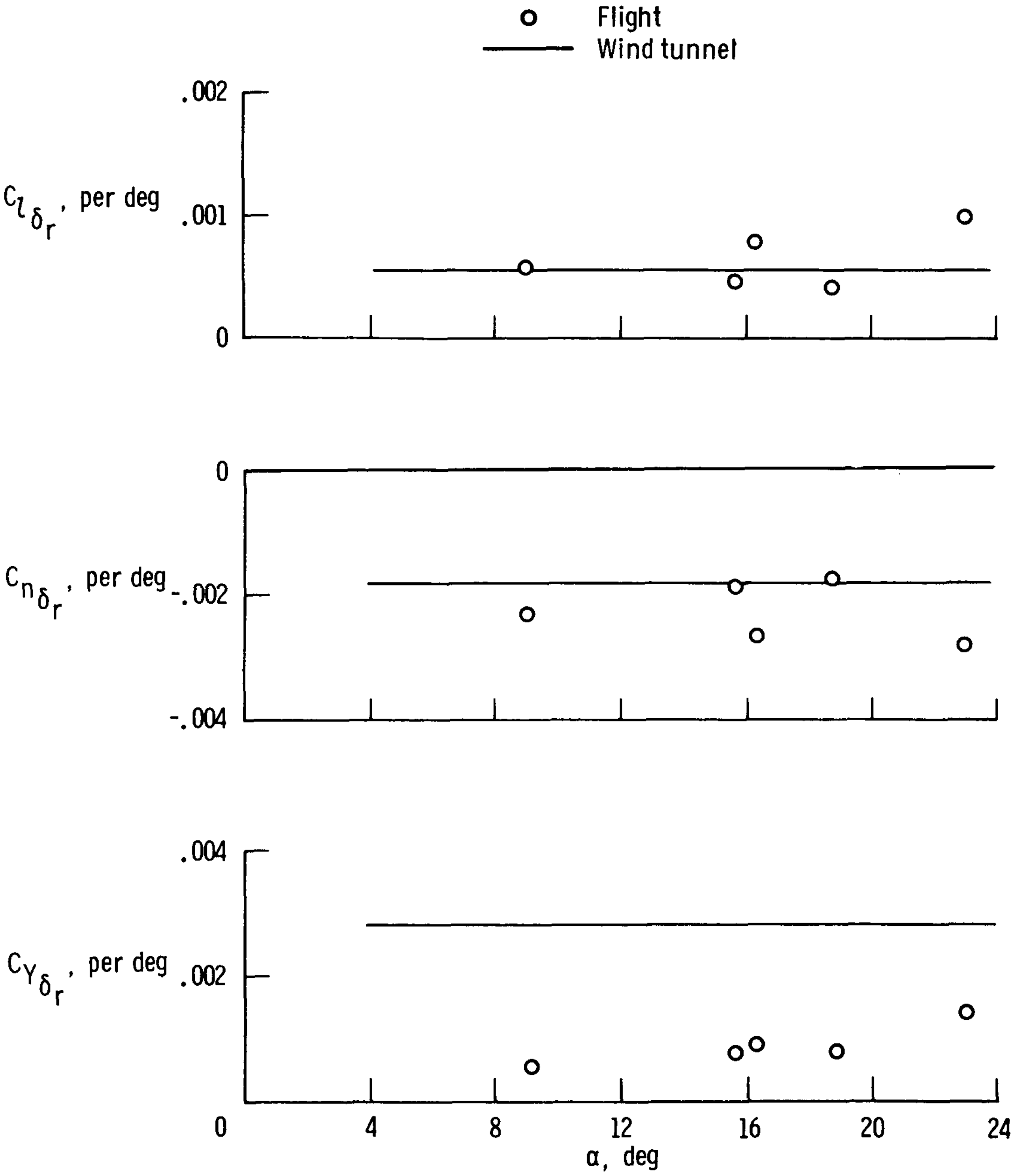

(b) M = 0.7, transonic configuration.

Figure 16. Continued.

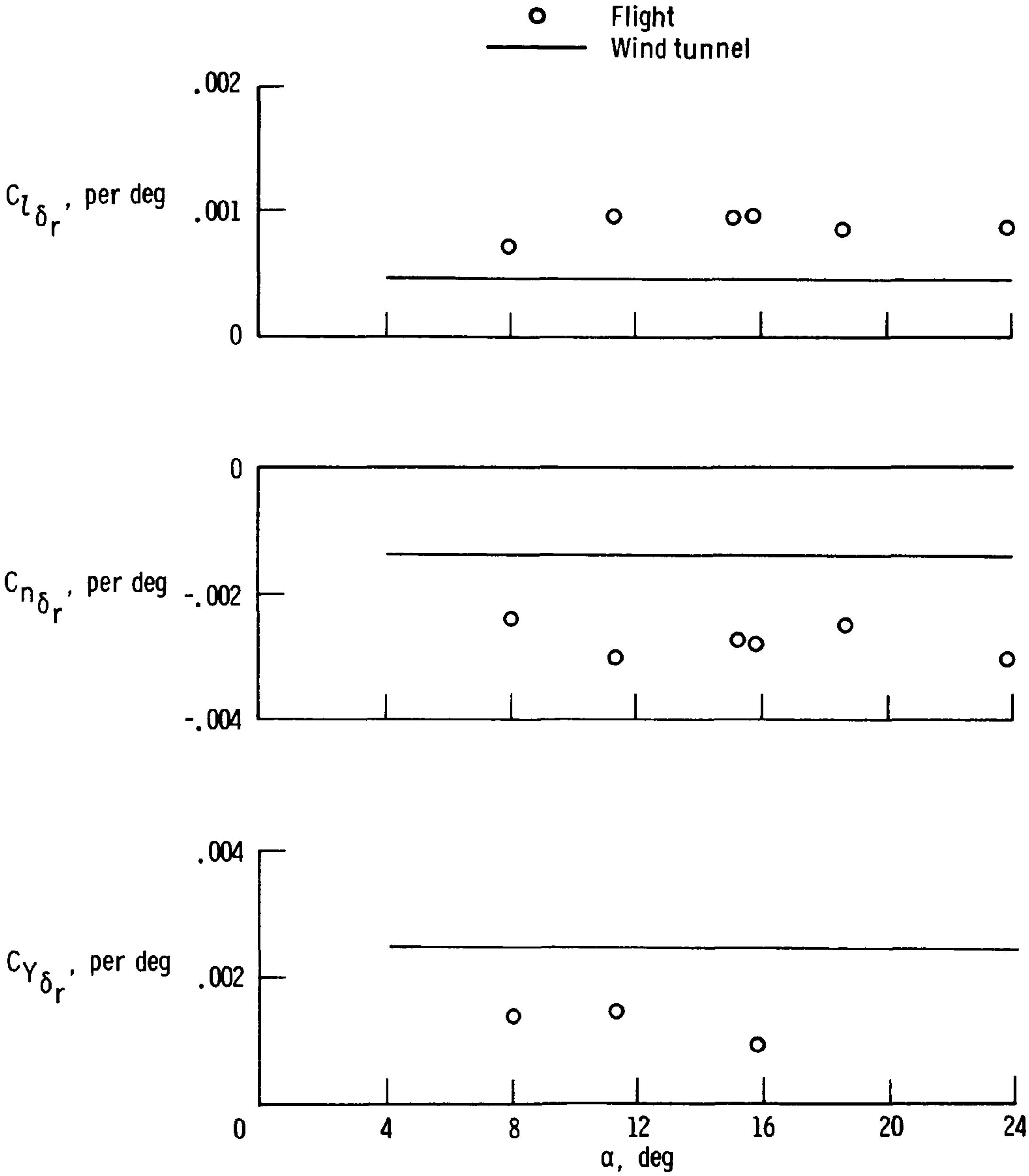

(c) M = 0.9, transonic configuration.

Figure 16. Continued.

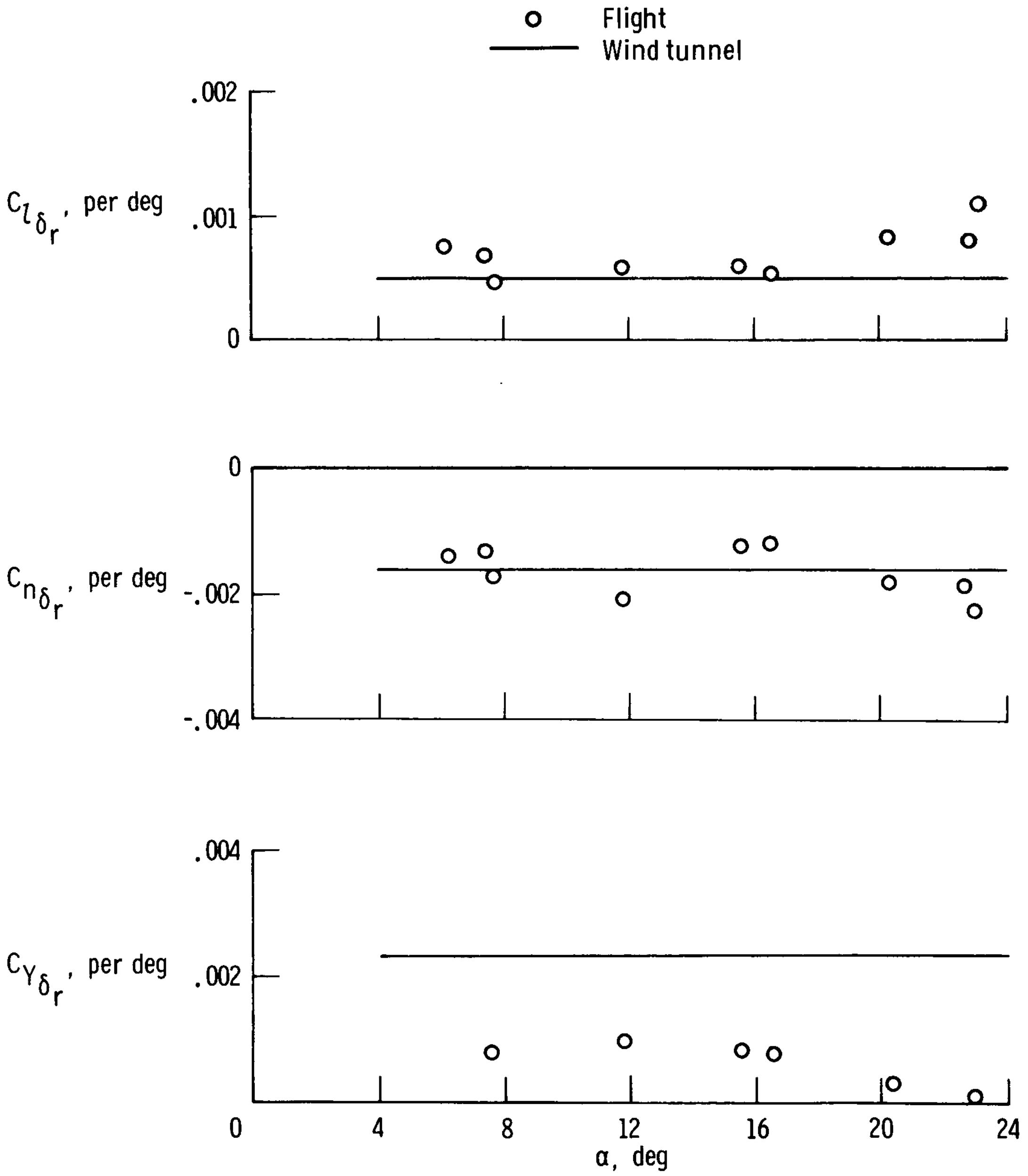

(d) M = 1.2, transonic configuration.

Figure 16. Concluded.

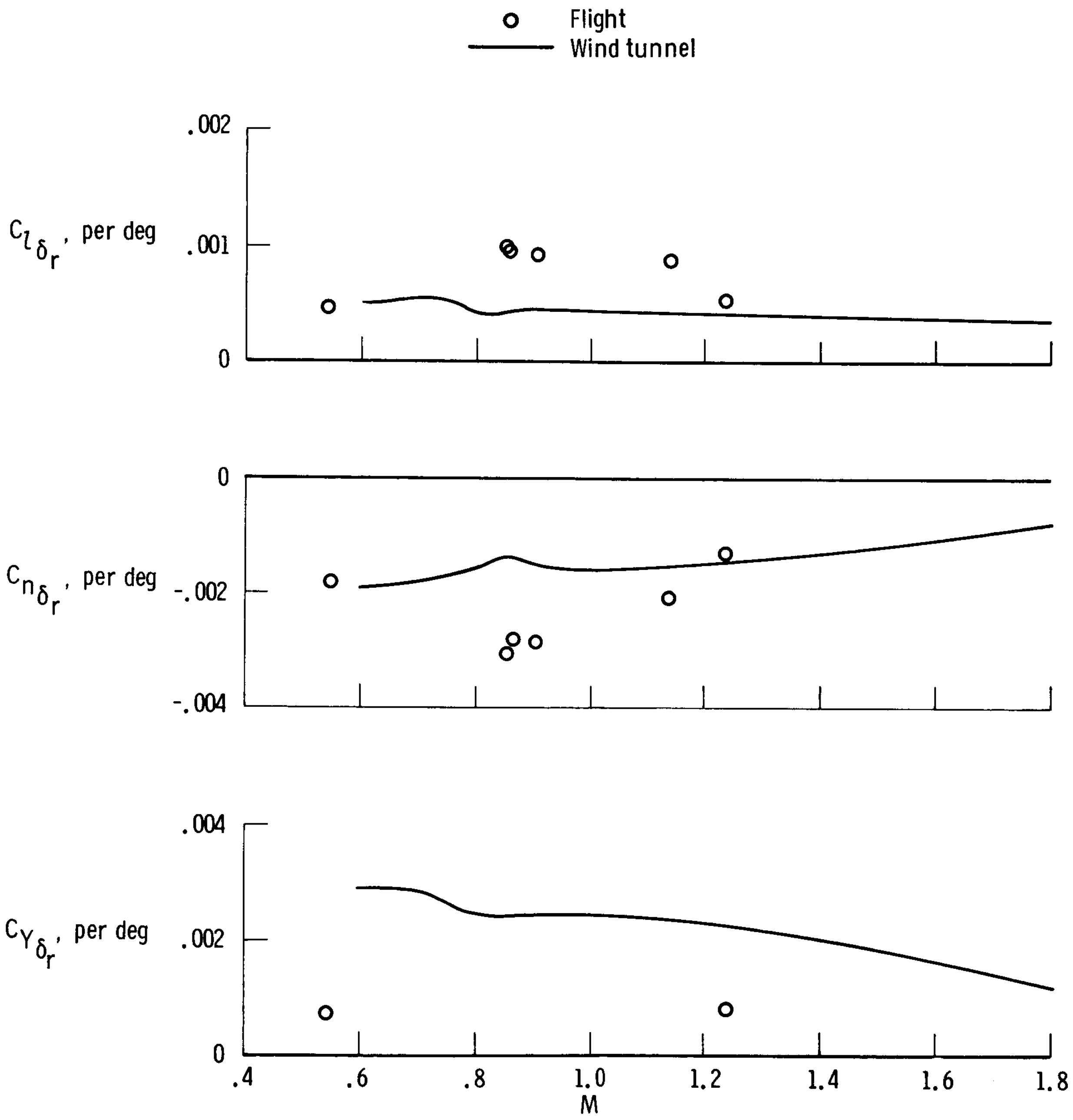

Figure 17. Comparison of flight and wind-tunnel rudder derivatives as a function of Mach number for an angle of attack of 14°. Transonic configuration.

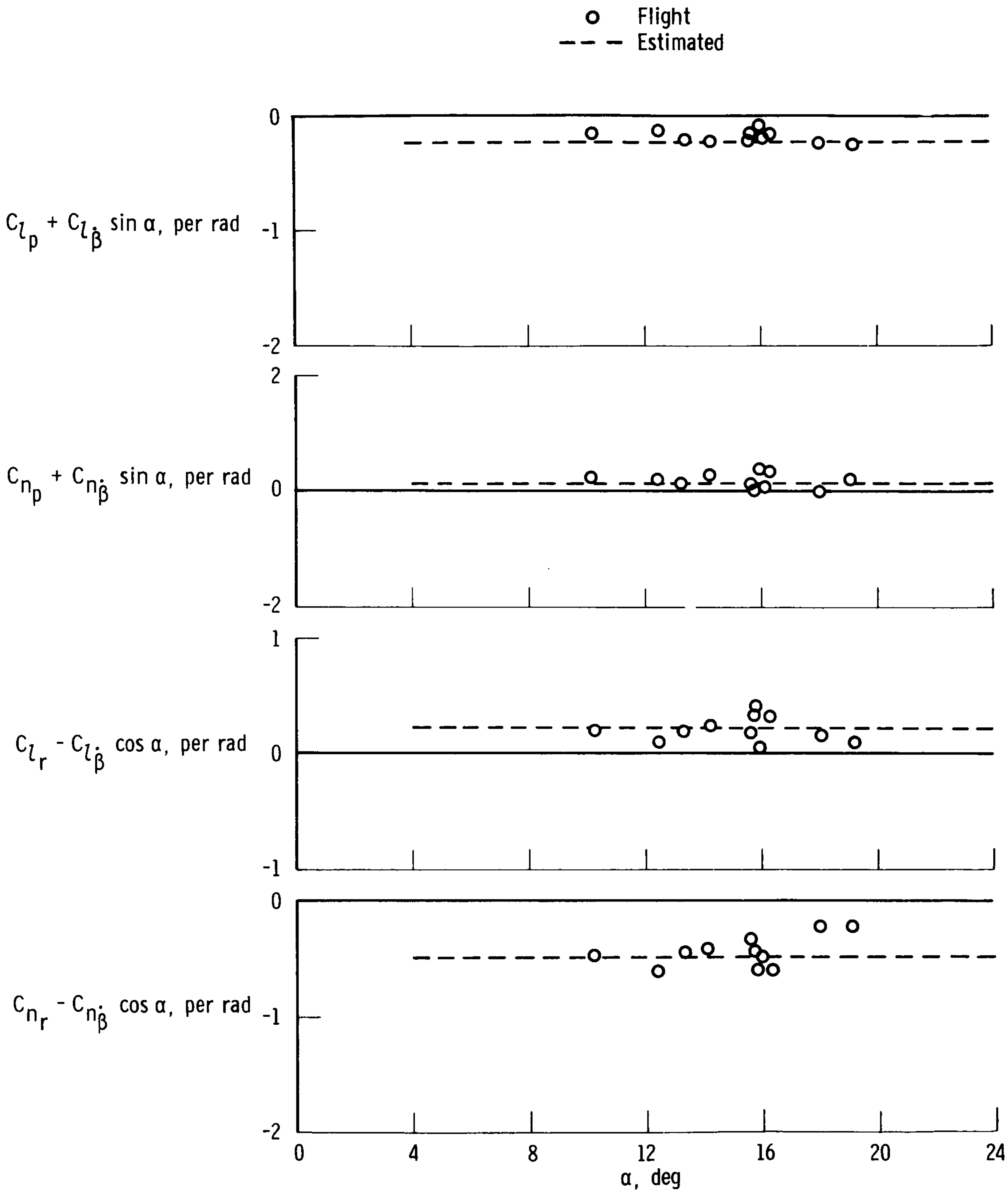

(a) M = 0.7, subsonic configuration.

Figure 18. Comparison of flight and predicted damping derivatives as a function of angle of attack.

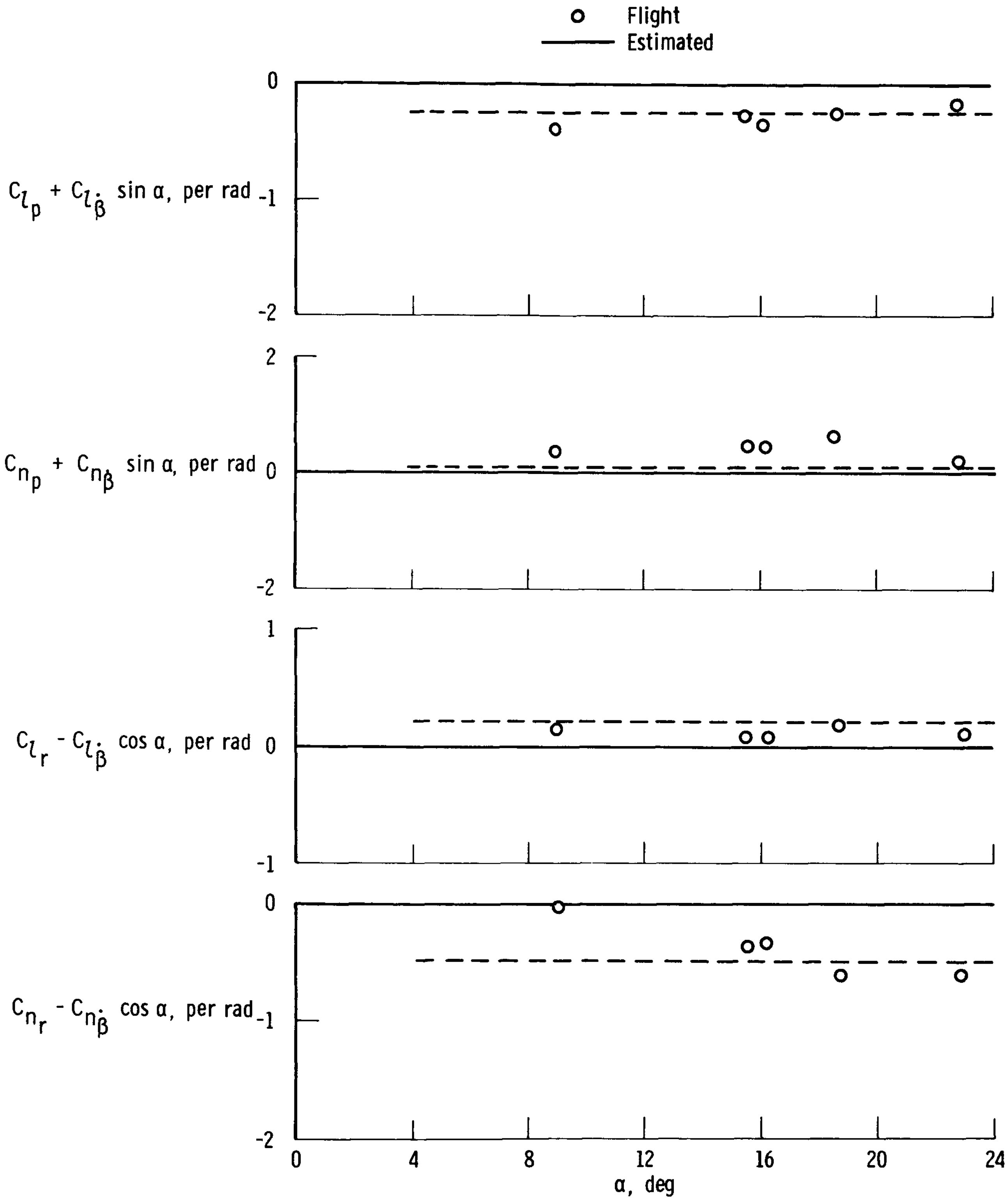

(b) M = 0.7, transonic configuration.

Figure 18. Continued.

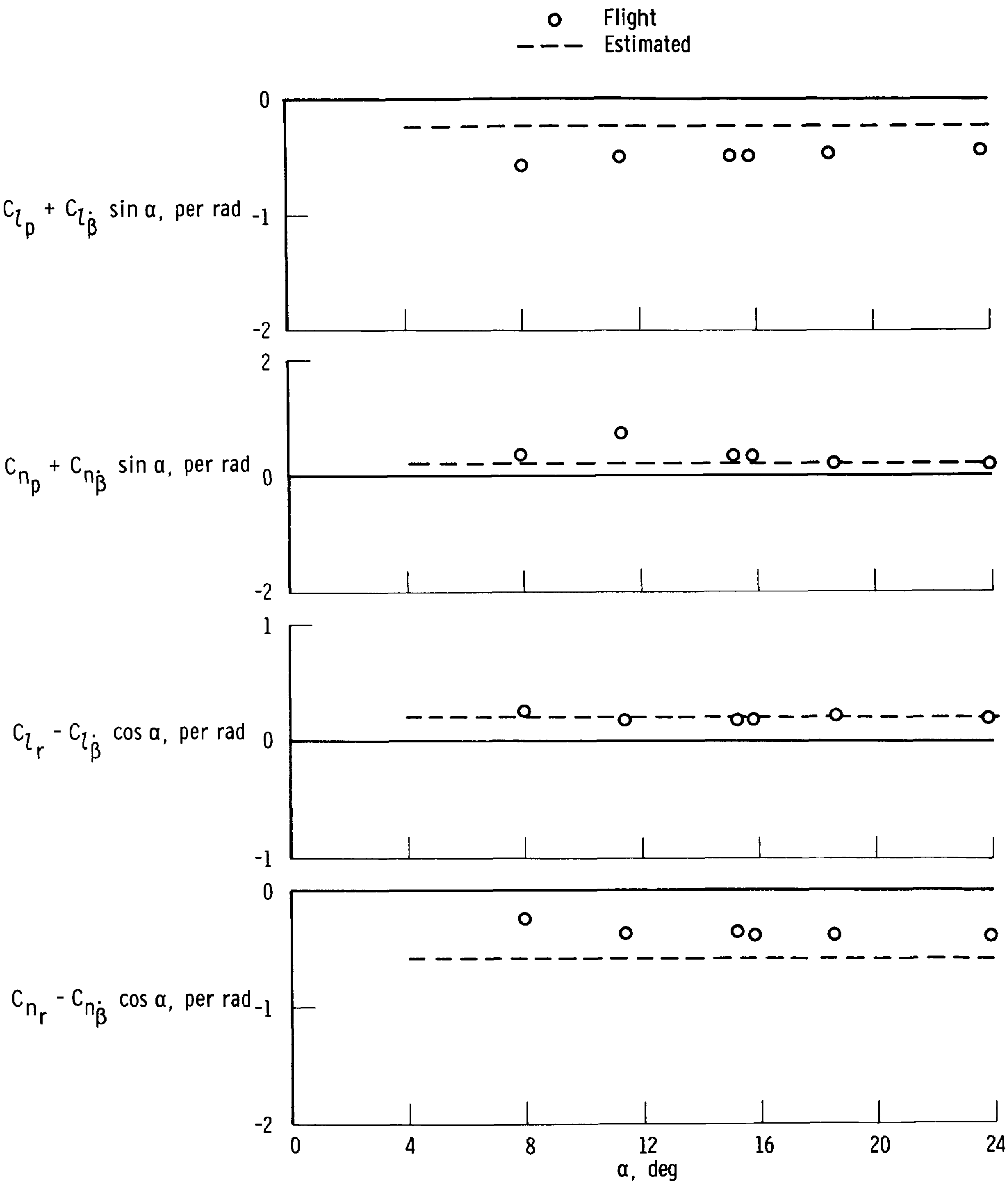

(c) M = 0.9, transonic configuration.

Figure 18. Continued.

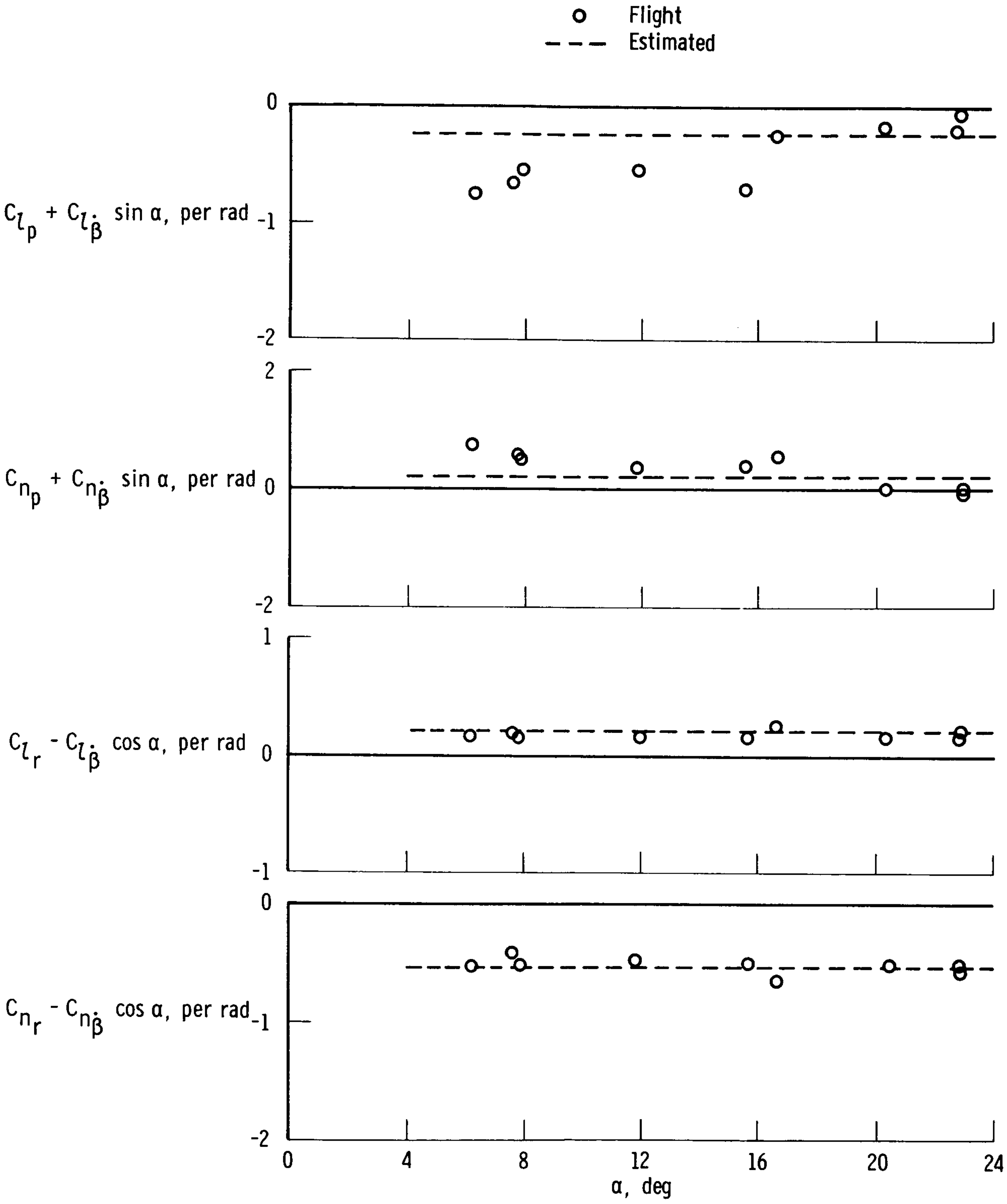

(d) M = 1.2, transonic configuration.

Figure 18. Concluded.

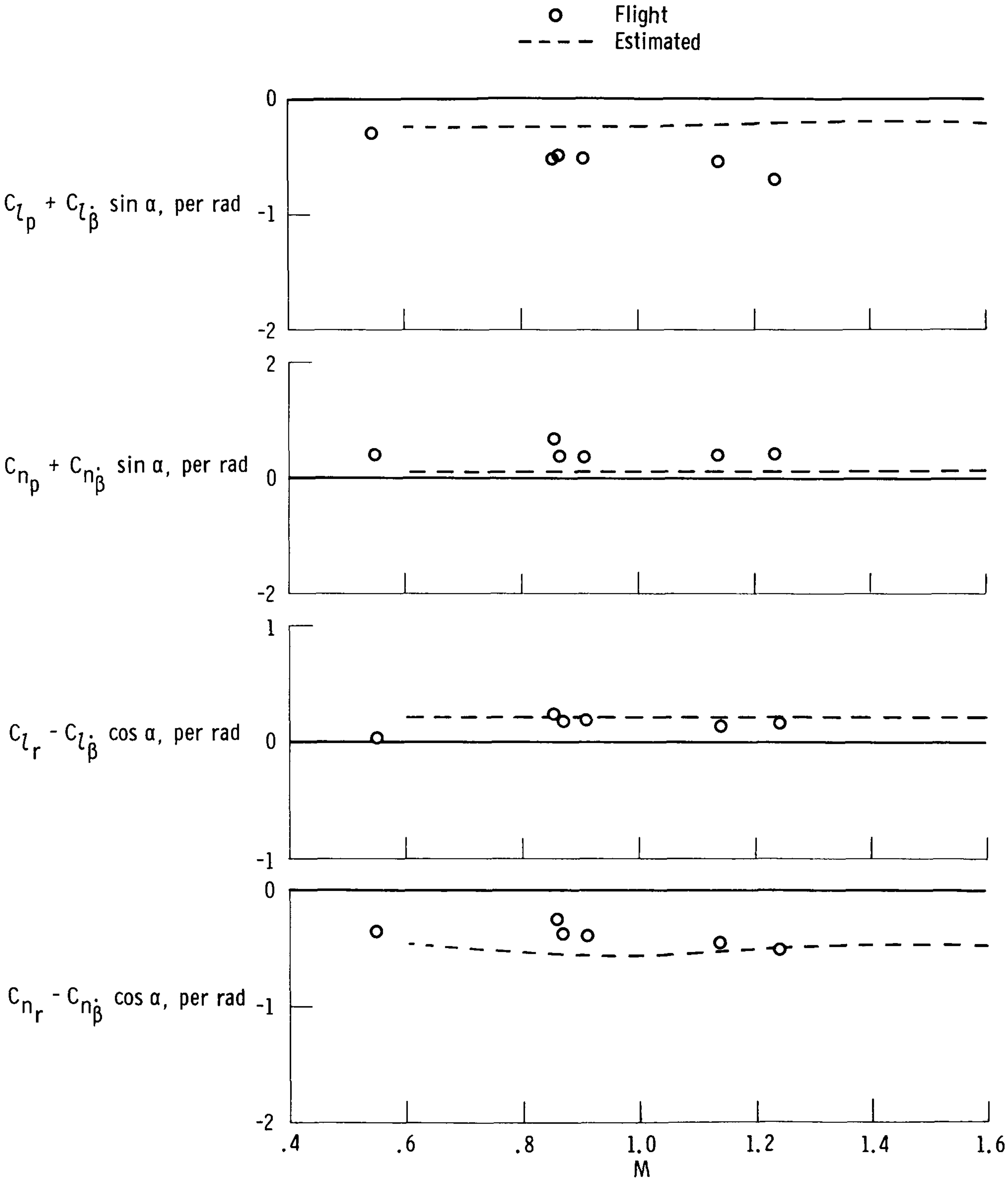

Figure 19. Comparison of flight and predicted damping derivatives as a function of Mach number for an angle of attack of 14°. Transonic configuration.

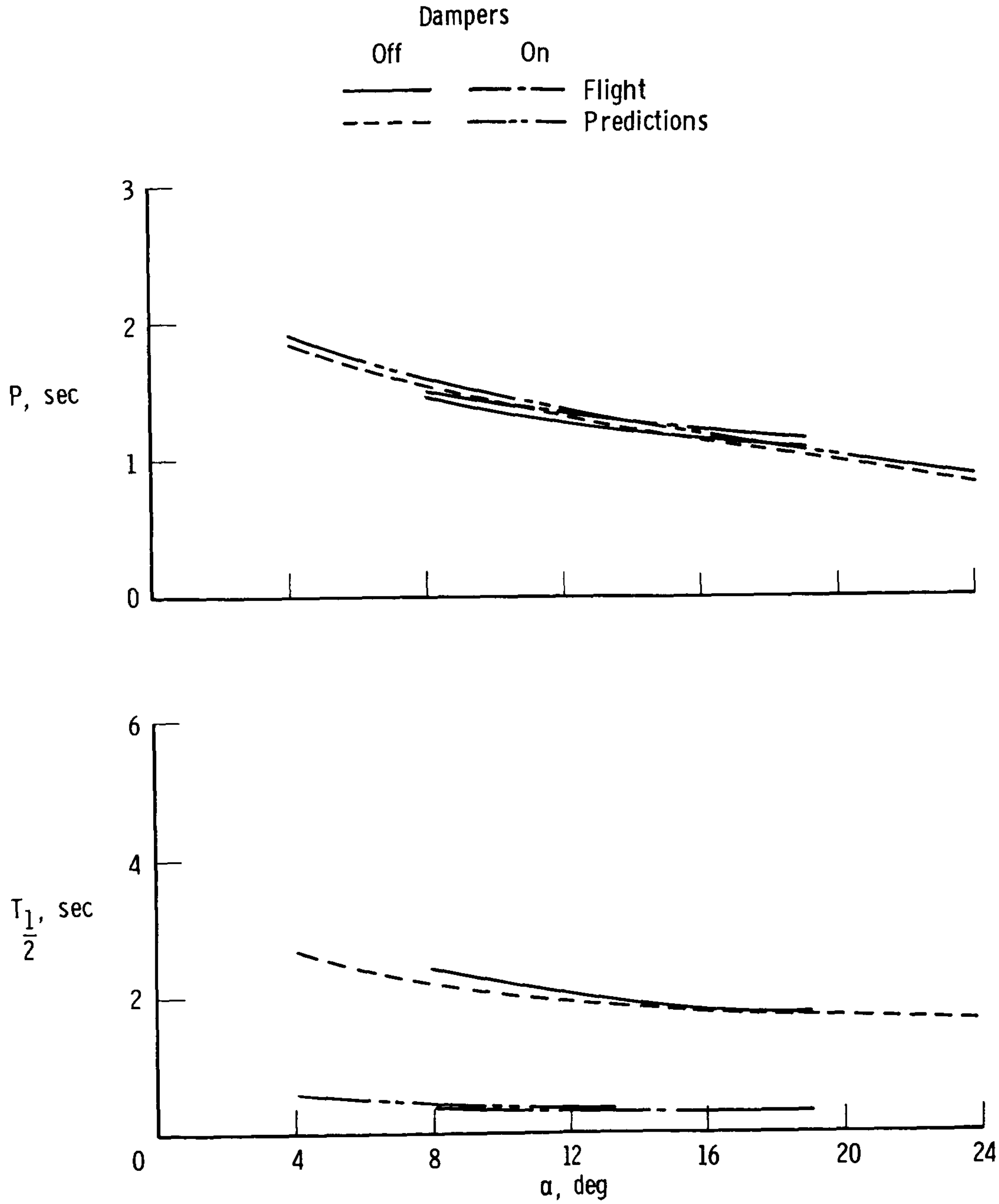

(a) M = 0.7, subsonic configuration.

Figure 20. Comparison of flight and predicted lateral-directional period and time to damp to one-half amplitude as a function of angle of attack.

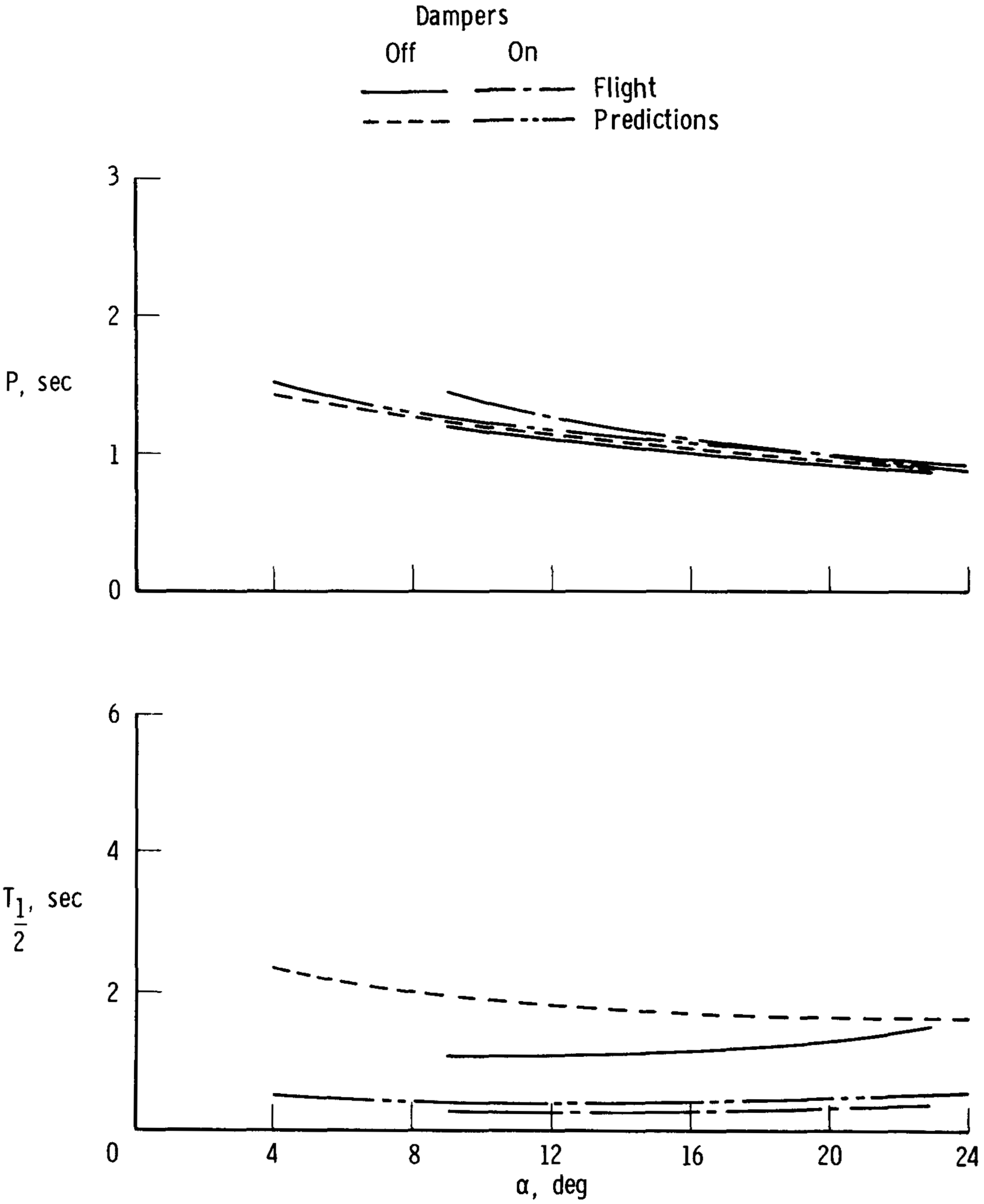

(b) M = 0.7, transonic configuration.

Figure 20. Continued.

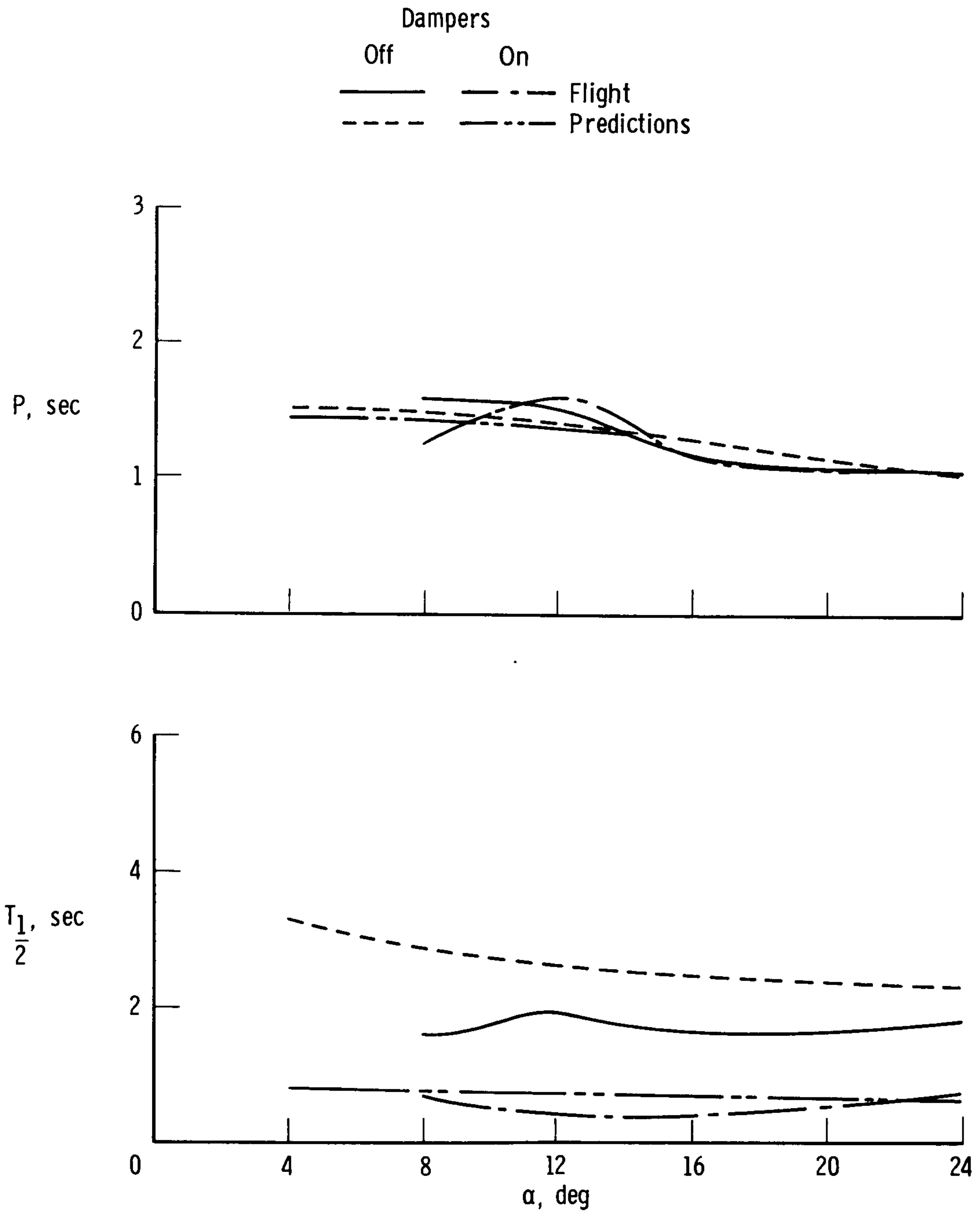

(c) M = 0.9, transonic configuration.

Figure 20. Continued.

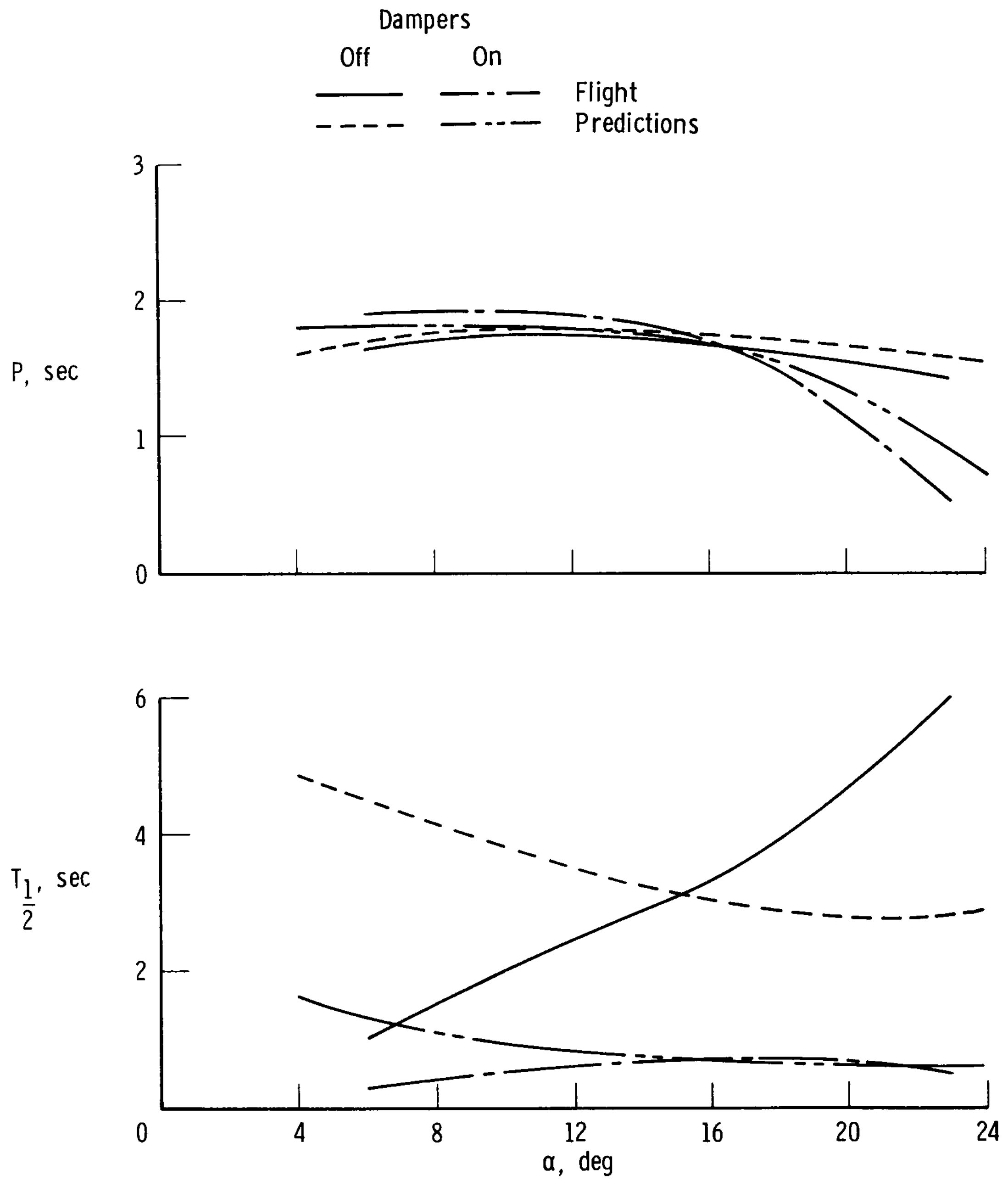

(d) M = 1.2, transonic configuration.

Figure 20. Concluded.

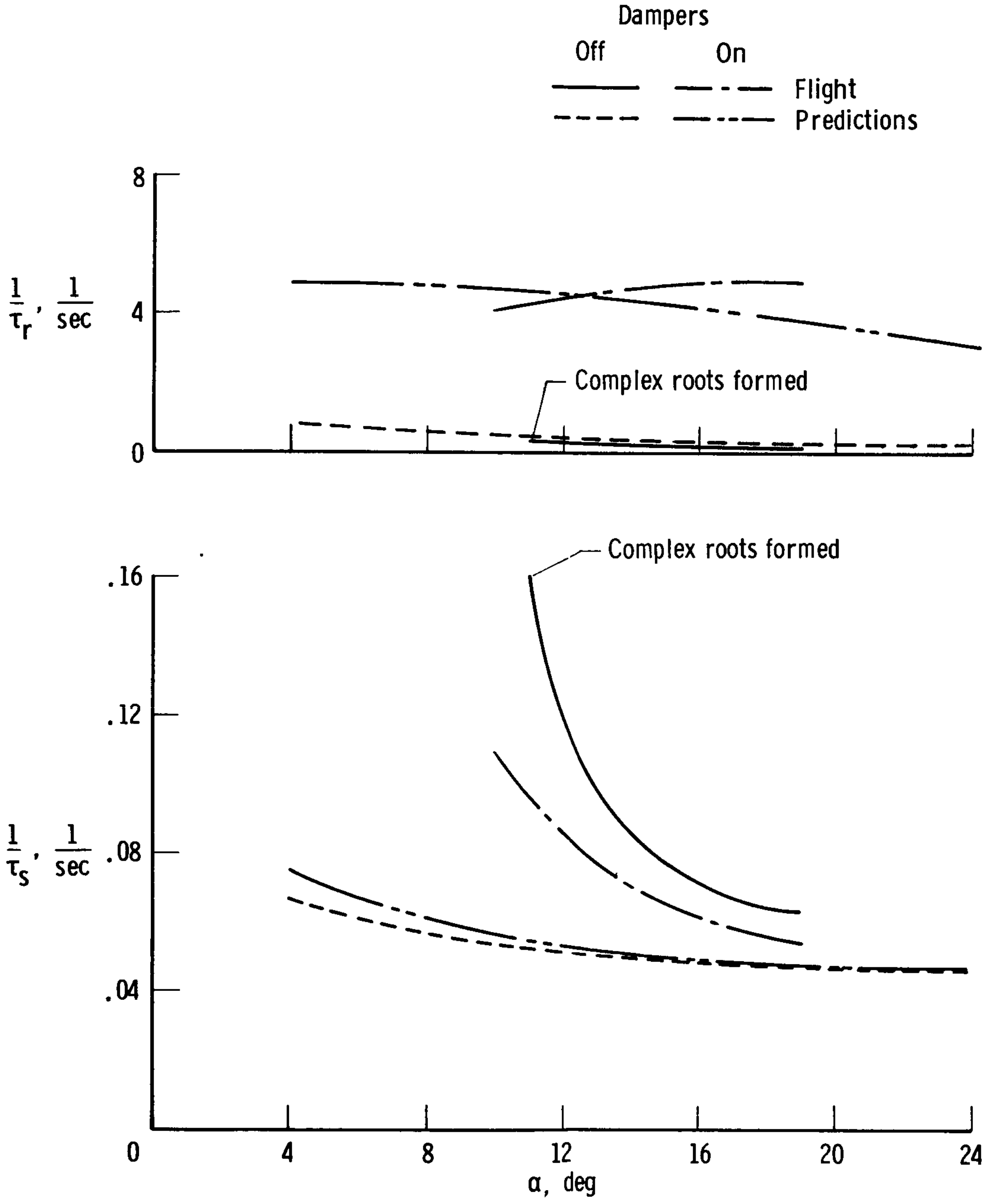

(a) M = 0.7, subsonic configuration.

Figure 21. Comparison of flight and predicted roll-spiral modes as a function of angle of attack.

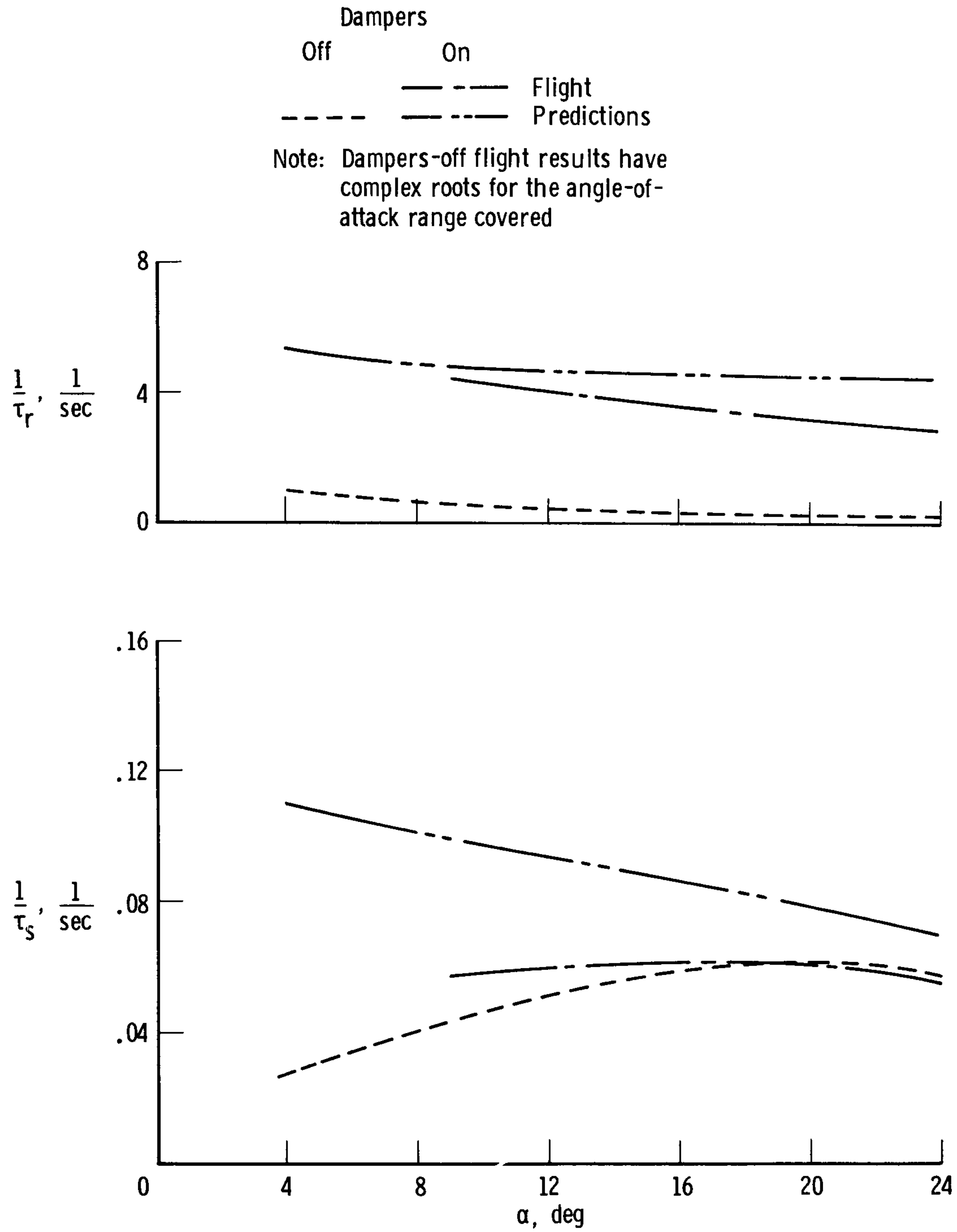

(b) M = 0.7, transonic configuration.

Figure 21. Continued.

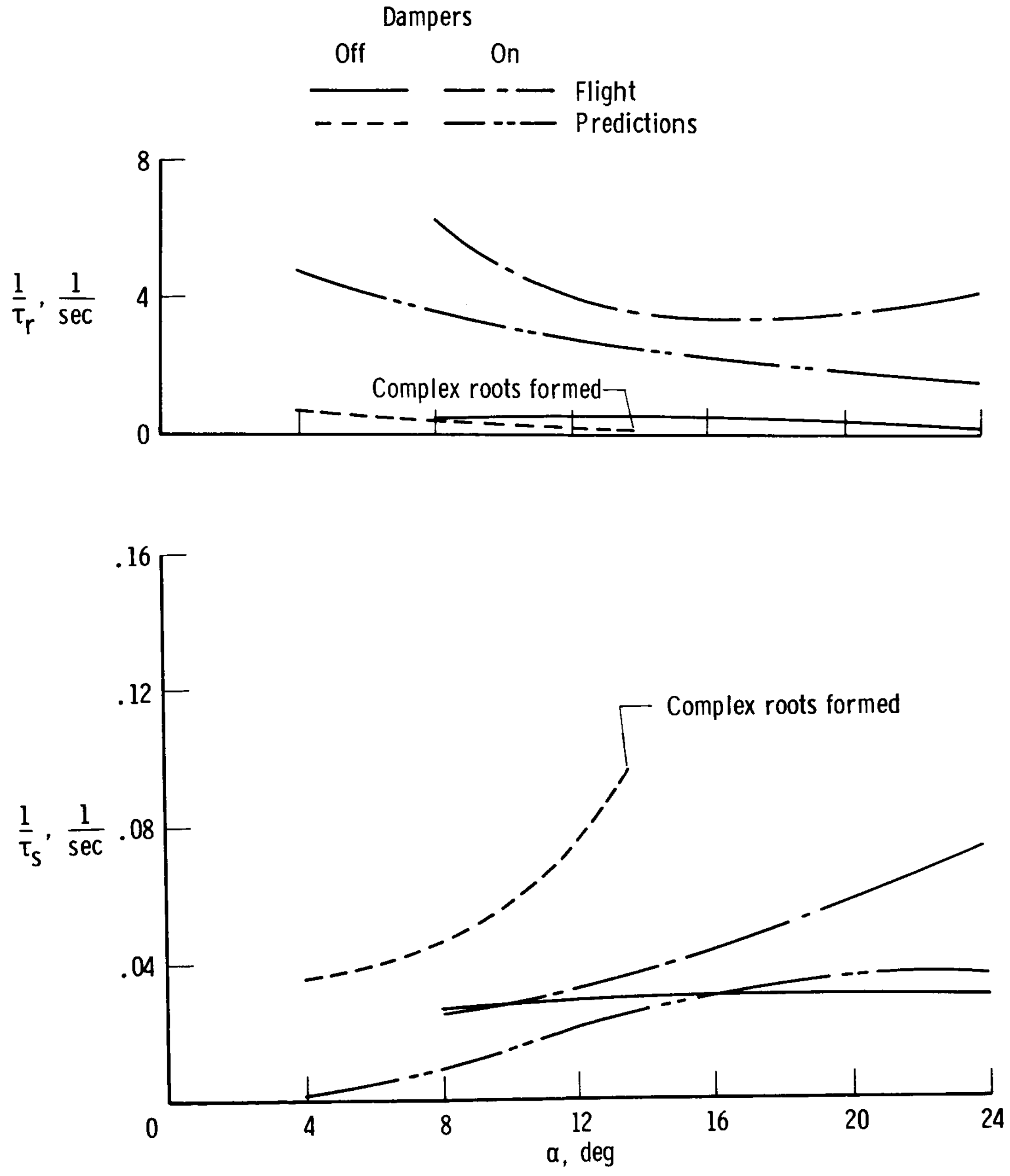

(c) M = 0.9, transonic configuration.

Figure 21. Continued.

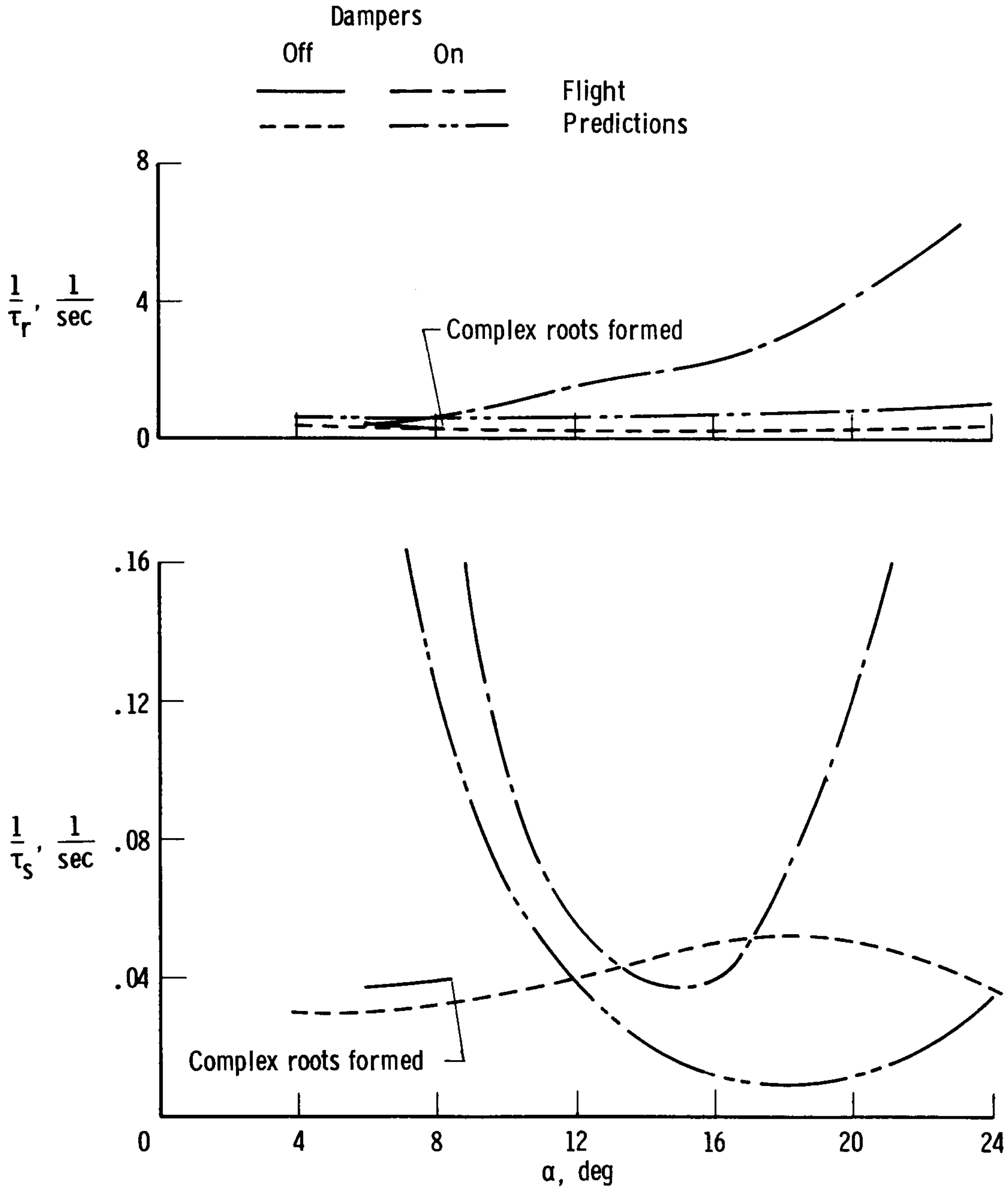

(d) M = 1.2, transonic configuration.

Figure 21. Concluded.

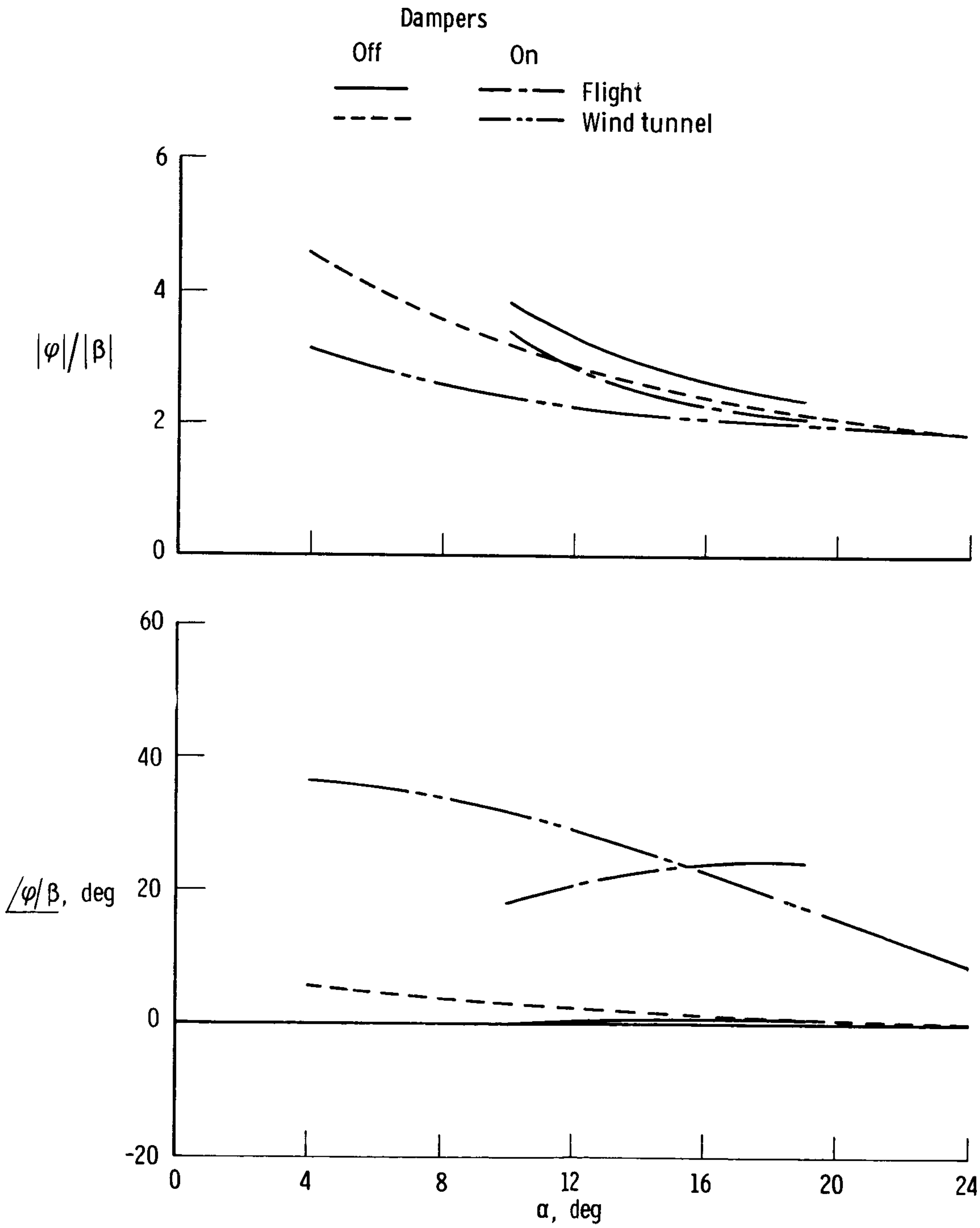

(a) M = 0.7, subsonic configuration.

Figure 22. Comparison of flight and predicted magnitude and phase angle of the ratio of roll angle to sideslip angle as a function of angle of attack.

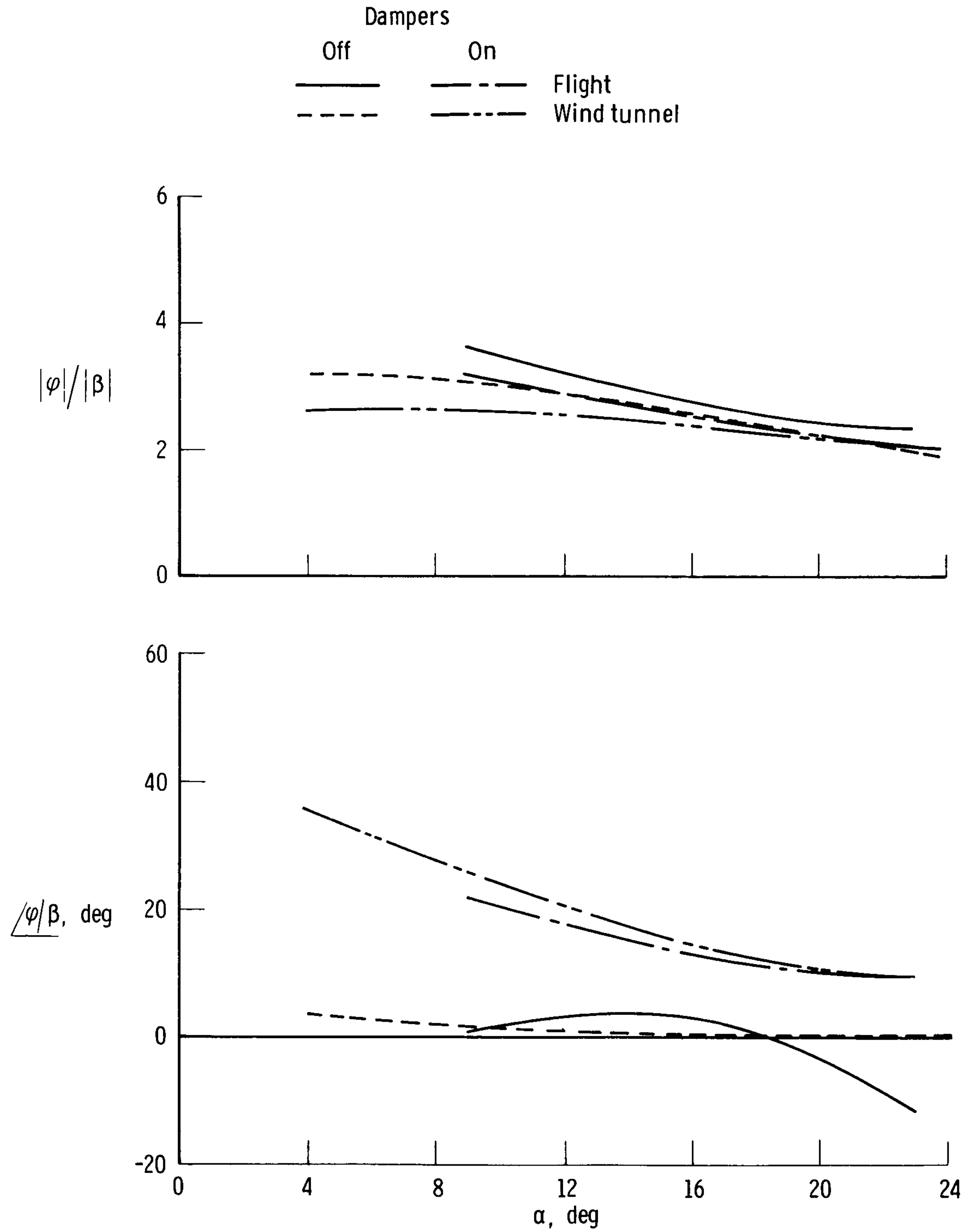

(b) M = 0.7, transonic configuration.

Figure 22. Continued.

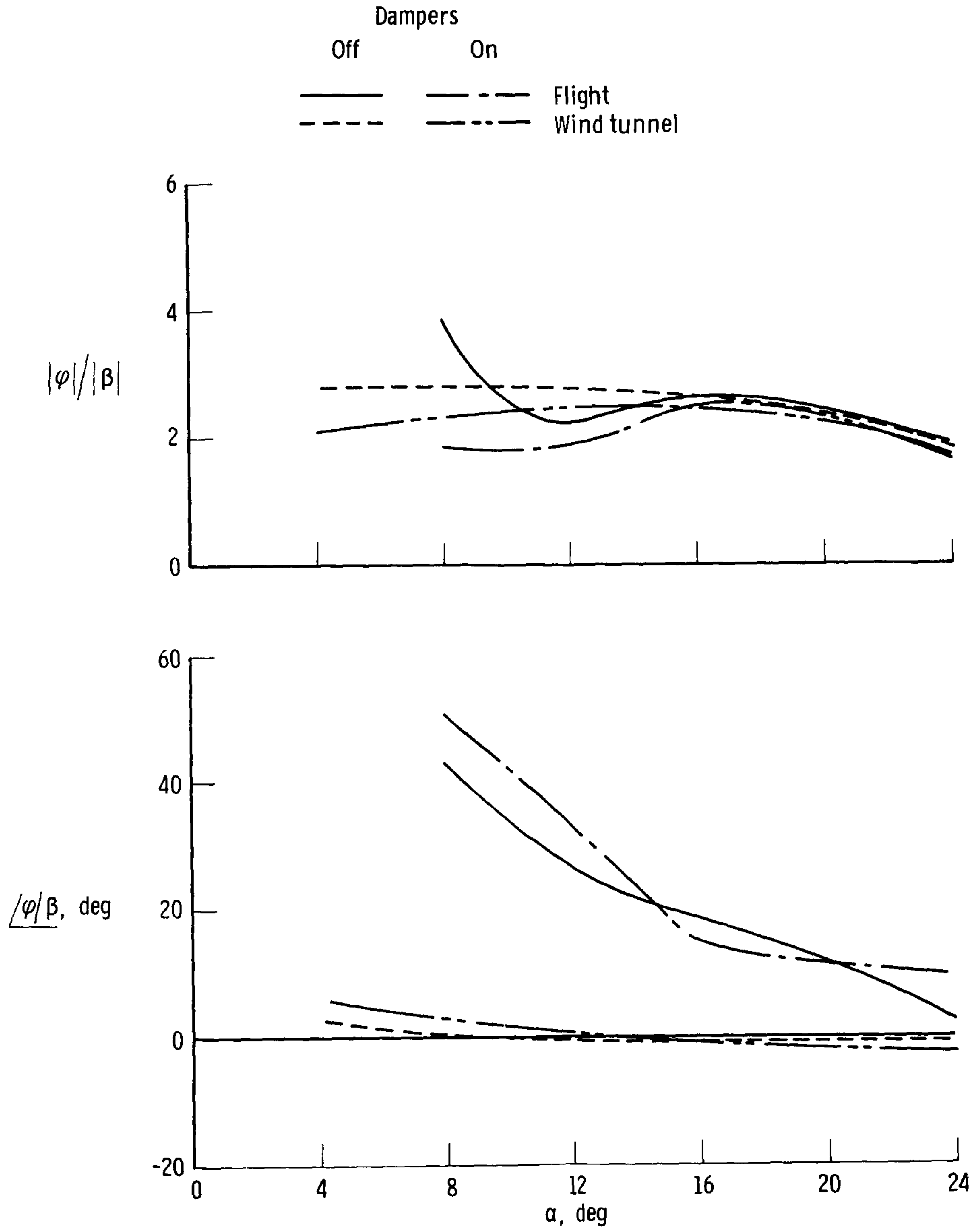

(c) M = 0.9, transonic configuration.

Figure 22. Continued.

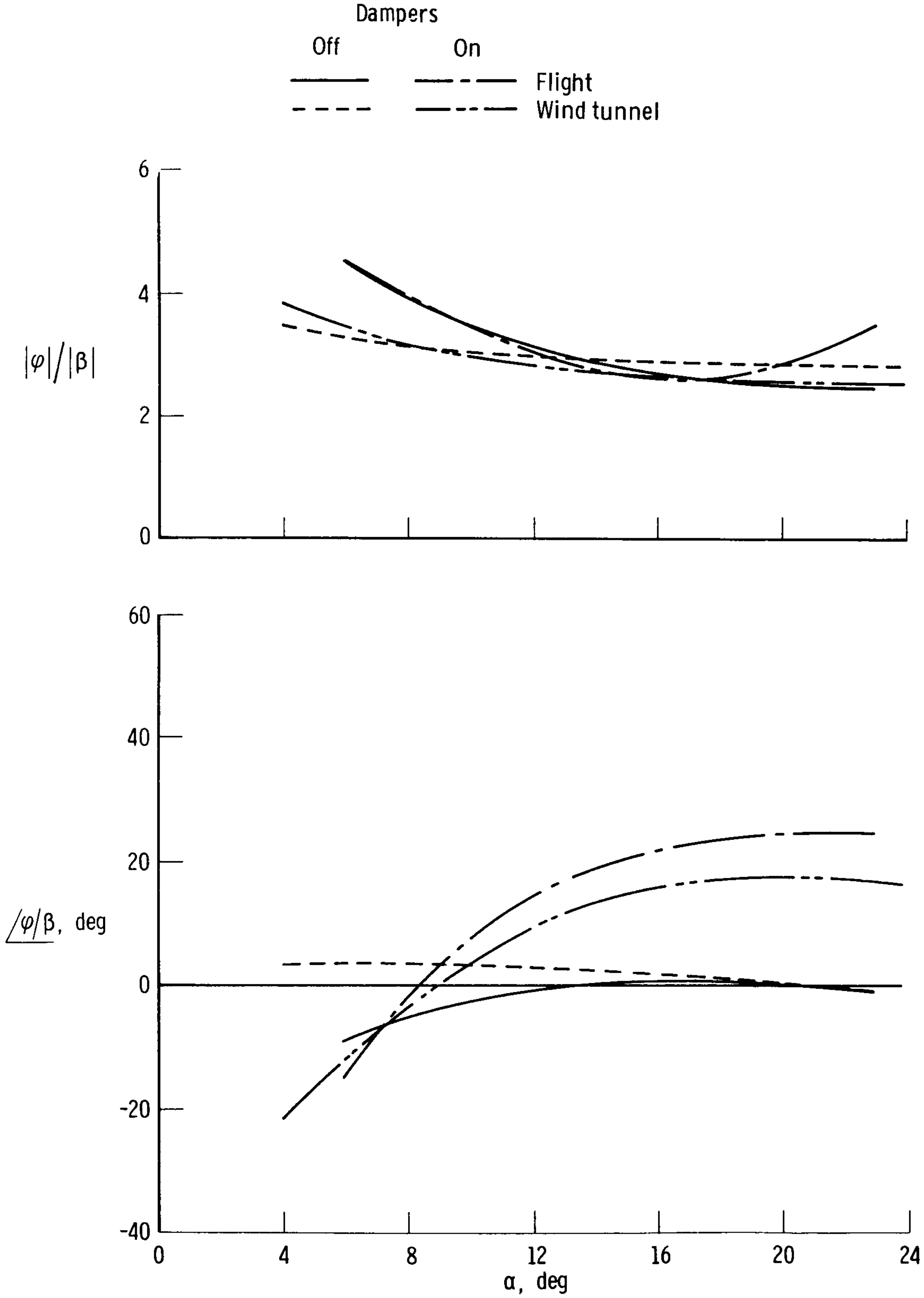

(d) M = 1.2, transonic configuration.

Figure 22. Concluded.

NASA-Langley, 1972 —— 31 H-708